Carbon dioxide and methane balances of pristine and degraded temperate peatlands

Empirical modeling of eddy covariance trace gas fluxes measured over heterogeneous terrain

Dissertation with the aim of achieving a doctoral degree at the
Faculty of Mathematics, Informatics and Natural Sciences
Department of Earth Sciences of
Universität Hamburg.

submitted by David Holl

Hamburg
2017

Als Dissertation angenommen vom
Fachbereich Geowissenschaften der Universität Hamburg
auf Grund der Gutachten von
Prof. Dr. Lars Kutzbach und
Prof. Dr. Eva-Maria Pfeiffer

Tag der Disputation: 16.Mai 2017

Abstract

Regarding their climate impact, natural peatlands are characterized by their ability to sequester atmospheric carbon. This trait is strongly connected to the water regime of these ecosystems. Large parts of the soil profile in peatlands are water-saturated, leading to anaerobic conditions and to a diminished decomposition of plant litter. The rate of carbon fixation by plant photosynthesis is larger than the decomposition rate of dead organic material. Over time, the amount of carbon that remains in the soil, and is not converted back to carbon dioxide, grows. Land use of peatlands often goes along with water level manipulations and thereby with alterations of carbon flux dynamics.

In the present thesis, eddy covariance carbon dioxide and methane flux measurements from two contrasting peatlands are compared. One site is in a pristine state (1), whereas the other one has been degraded by peat mining. On the latter site, two management types are implemented: (2) drainage and (3) rewetting. The pristine investigation site (Rio Pipo) is located on Tierra del Fuego in southern Argentina; seven months of flux data are available from there. A two year dataset is evaluated from the degraded site (Himmelmoor) that is situated in northern Germany. The three investigated land use states are conceptually regarded as sequential, as they can illustrate the possible path a pristine peatland would take over degradation and rewetting back to a natural state.

At the degraded site, the development of rewetting over time is given by greenhouse gas flux balances that cover two consecutive years. Rewetting does have a considerable effect on the annual carbon gas fluxes. Carbon dioxide release decreases up to 40 % (from 22.16 $\pm$ 0.28 mol m^{-2} a^{-1} to 12.91 $\pm$ 0.29 mol m^{-2} a^{-1}), while methane release is up to 84 % (0.45 $\pm$ 0.01 mol m^{-2} a^{-1} vs. 0.83 $\pm$ 0.01 mol m^{-2} a^{-1}) lower from the drained surfaces. Molar carbon dioxide fluxes are factors between 20 and 30 larger than methane fluxes from both surface classes. One mol methane does, however, have a different climate warming effect than one mol carbon dixoide, and its lifetime in the atmosphere is shorter. Factoring in these properties leads to a twofold interpretation of the results. On short timescales (20 years), the ramifications of increased methane release offsets the climate cooling impact of decreasing carbon dioxide emissions. On long timescales (100 years), rewetting shifts the investigated peatland's greenhouse gas balance towards a climate cooling effect. While the rewetted areas are still a carbon source today, they are

less of a source than the drained areas and release progressively less carbon gases in the course of rewetting.

In contrast to the degraded site, the pristine peatland is a net carbon sink in summer and a smaller source of carbon in winter. Winter source strength is two times smaller compared to the rewetted areas and 2.5 times smaller relative to the drained surfaces.

In order to report fluxes integrated over time, two methodological topics are addressed: (1) gap-filling of gas flux time series and (2) the assessment of eddy covariance signals that contain information from multiple microforms. Due to the importance of methane flux dynamics for the evaluation of rewetting measures, this trace gas flux has to be included in a comprehensive and informative wetland greenhouse gas balance. There is, however, some ambiguity in literature about eddy covariance methane flux gap-filling. I propose a data-driven decision-making framework for empirical modeling of eddy covariance gas fluxes that includes the selection of input variables and compares different model types. The algorithm also evaluates surface classification data if fluxes were recorded over heterogeneous terrain.

Mechanistic modeling was feasible with carbon dioxide fluxes measured over homogeneous terrain at the pristine investigation site. In comparison to these generally more robust flux estimates, the proposed gap-filling algorithm gives equally good results, while this notion is based on the Akaike Information Criterion and hence does take into account the higher complexity of the applied empirical models.

Individual time series related to distinct surface classes were inferred from the eddy covariance gas flux time series measured over heterogeneous terrain at the degraded site. When the derived carbon dioxide models on surface class level are interpreted in a mechanistic way, the resulting plant parameters match literature values for the actual plant species occurring on this microform. Therefore, the applied extraction of surface class time series from landscape-scale eddy covariance data appears to be feasible.

Zusammenfassung

Bezüglich ihrer Klimawirksamkeit sind natürliche Moore durch ihre hohe Fähigkeit atmosphärischen Kohlenstoff zu binden, charakterisiert. Diese Eigenschaft ist eng mit dem Wasserhaushalt dieser Ökosysteme verbunden. Moorböden sind großteils wassergesättigt, was zu anaeroben Bedingungen und einem veringerten Abbau organischer Substanz führt. Die Festlegung von Kohlenstoff durch Photosynthese ist größer als die Rate mit der totes organisches Material im Boden abgebaut wird. Mit der Zeit wächst so die Kohlenstoffmenge, die im Boden verbleibt und nicht wieder zu Kohlendioxid umgewandelt wird. Ein Absenken des Wasserstands im Zuge der Moornutzung führt zur Belüftung des Moorbodens und daher zum vermehrten Abbau des seit Jahrtausenden gespeicherten Kohlenstoffs.

In der vorliegenden Arbeit werden Eddy Kovarianz Kohlendioxid- und Methanflüsse dreier verschiedener Moornutzungstypen verglichen: (1) eines unberührten Hochmoores, (2) eines durch laufenden Torfabbau degradierten Moores und (3) eines nach Torfabbau wiedervernässten Moorstandorts. Das naturnahe Untersuchungsgebiet (Rio Pipo) befindet sich auf Feuerland in Süd-Argentinien; von dort liegen sieben Monate Flussdaten vor. Von dem in Norddeutschland liegenden, degradierten Standort (Himmelmoor) wird ein zweijähriger Datensatz ausgewertet. Die Stadien der Landnutzug der drei Standorte können konzeptionell als zeitlich aufeinanderfolgend betrachtet werden. Sie veranschaulichen den möglichen Weg eines unberührten Moores über Degradierung und Wiedervernässung zurück zu einem natürlichen Zustand.

Die zeitliche Entwicklung der Wiedervernässung des degradierten Untersuchungsstandorts ist durch die Treibhausgasbilanzen zweier aufeinanderfolgender Jahre dokumentiert. Wiedervernässung hat erhebliche Auswirkungen auf die jährlichen Kohlenstoffflüsse. Die Kohlendioxidfreisetzung wird um bis zu 40 % verringert (von 22.16 $\pm$ 0.28 mol m^{-2} a^{-1} zu 12.91 $\pm$ 0.29 mol m^{-2} a^{-1}), während die Methanemissionen der dränierten Flächen um bis zu 84 % niedriger (0.45 $\pm$ 0.01 mol m^{-2} a^{-1} vs. 0.83 $\pm$ 0.01 mol m^{-2} a^{-1}) sind. Die molaren Kohlendioxidflüsse sind zwischen zwanzig- und dreißigmal größer als die Methanflüsse beider Oberflächentypen. Ein Mol Methan wirkt jedoch anders auf die Klimaerwärmung als ein Mol Kohlendioxid und hat eine kürzere Aufenthaltsdauer in der Atmosphäre. Unter Berücksichtigung dieser Eigenschaften ergibt sich eine

zweifache Interpretation der Ergebnisse. Kurzfristig (20 Jahre) relativiert die Wirkung ansteigender Methanfreisetzung die klimakühlenden Effekte verringerter Kohlendioxidemissionen. Langfristig (100 Jahre) wird die Treibhausgasbilanz des untersuchten Moores durch Wiedervernässung in Richtung einer klimakühlenden Wirkung verschoben. Während die wiedervernässten Flächen zur Zeit noch Kohlenstoffquellen sind, sind sie eine geringere Quelle als die dränierten Flächen und setzen im Zuge der Wiedervernässung immmer weniger Kohlenstoffgase frei.

Im Gegensatz zum degradierten Standort ist das naturnahe Moor eine Kohlenstoffsenke im Sommer und eine geringe Quelle im Winter. Im Winter sind die wiedervernässten Flächen eine zweifach stärkere und die dränierten Gebiete eine zweieinhalbmal größere Kohlendioxidquelle.

Um über die Zeit integrierte Flüsse angeben zu können, mussten zunächst zwei methodische Themen behandelt werden: (1) Das Füllen von Lücken in Gasflusszeitreihen und (2) die Auswertung von Eddy-Kovarianz-Datensätzen, die Informationen von mehreren Oberflächen beinhalten. Auf Grund der Bedeutsamkeit der Methanflussdynamik für die Bewertung von Wiedervernässungsmaßnahmen, müssen die Flüsse dieses Spurengases Teil einer umfassenden und aussagekräftigen Treibhausgasbilanz eines Feuchtgebiets sein. Die vorhandene Literatur über das Füllen von Lücken in Eddy Kovarianz Methanflusszeitreihen ist jedoch nicht eindeutig. Ich schlage ein Rahmenkonzept zur datengesteuerten Entscheidungsfindung für die empirische Modellierung von Eddy Kovarianz Gasflüssen vor, das die Auswahl von Eingansvariablen und den Vergleich verschiedener Modelltypen beinhaltet. Der Algorithmus wertet auch Oberflächenklassifikationsdaten aus, falls Flüsse über heterogenem Gelände aufgezeichnet wurden.

Mechanistische Modelle konnten an die Kohlendioxidflüsse, die im naturnahen Standort über homogener Oberfläche gemessen wurden, angepasst werden. Im Vergleich mit diesen im Allgemeinen belastbareren Flussabschätzungen, erzeugt der vorgeschlagene Algorithmus ähnlich gute Ergebnisse. Diese Bewertung der Ergebnisse basiert auf der Auswertung des Akaike Information Criterion. Die höhere Komplexität der empirischen Modelle wurde somit in diesem Vergleich berücksichtigt.

Separate Zeitreihen einzelner Oberflächenklassen wurden aus den Eddy Kovarianz Gasflüssen, die über heterogenem Gelände gemessen wurden, abgeleitet. Die Interpretation der so abgeleiteten Kohlendioxidflussmodelle einzelner Oberflächenklassen ergibt Pflanzenparameter, die in der Literatur angegebenen Werten der tatsächlich auf diesen Oberflächen vorkommenden Pflanzen entsprechen. Die Extrahierung von oberflächenspezifischen Zeitreihen aus Eddy Kovarianz Daten auf Landschaftsskala erscheint demzufolge machbar.

Contents

List of Figures

List of Tables

Abbreviations

#HLN	number of hidden layer nodes.
r	Pearson's correlation coefficient.
ABL	atmospheric boundary layer.
AIC	Akaike's information criterion.
ANN	artificial neural network.
ATLO	automatic time lag optimization.
BE	bias error.
CC_{dra}	class contribution of *drained* surfaces.
CC_{rew}	class contribution of *rewetted* surfaces.
CC_{veg}	class contribution of *vegetated* surfaces.
$CC_{veg,E}$	class contribution of surface class *vegetated* within CC_{dra}.
$CC_{veg,W}$	class contribution of surface class *vegetated* within CC_{rew}.
CH_4	methane.
CO_2	carbon dioxide.
CO_2eq	carbon dioxide equivalents.
EC	eddy covariance.
EPReM	ecosystem photosynthesis respiration model.
F_{CH4}	methane flux.
F_{CO2}	carbon dioxide flux.
FFH	Fauna Flora Habitat Guideline.
$fuzzy_{af}$	fuzzy variable *afternoon*.
$fuzzy_{ev}$	fuzzy variable *evening*.
$fuzzy_{ni}$	fuzzy variable *night*.
$fuzzy_{su}$	fuzzy variable *summer*.
$fuzzy_{wi}$	fuzzy variable *winter*.
GHG	greenhouse gas.
GRNN	generalized regression neural network.
GTP	global temperature change potential.
GWP	global warming potential.
GWP100	global warming potential on a 100 years time horizon.
GWP20	global warming potential on a 20 years time horizon.
HLN	hidden layer node.
I-SIM	input-sensitive input and model selection.
Lim_{gf}	final limit.
Lim_{init}	initial limit.
Lim_{rand}	random limits.
LUT	look-up table.
Lw_{out}	outgoing longwave radiation.
MAE	mean absolute error.
MDS	marginal distribution sampling.
MDS_{QC}	marginal distribution sampling quality check.
MDV	mean diurnal variation.
MF0	high quality fluxes.
MF1	intermediate quality fluxes.
MF2	low quality fluxes.
MLP	multilayer perceptron.
MLR	multilinear regression.
MSE	mean squared error.
NEE	net ecosystem exchange.
P_{max}	maximum photosynthesis.
PAR	photosynthetically active radiation.
R_{eco}	ecosystem respiration.
R_g	global radiation.
RBF	radial basis function.
RMSE	root mean squared error.
RSSI	relative signal strength indication.
SC_{dra}	surface class *drained*.
SC_{rew}	surface class *rewetted*.
SC_{veg}	surface class *vegetated*.
SCTS	surface class time series.
Sw_{out}	outgoing shortwave radiation.
T_{air}	air temperature.
TVTS	tower view time series.
VPD	water vapour pressure deficit.
WT	water table depth.

Chapter 1

Introduction

1.1 Objectives

The present study covers carbon gas fluxes from two wetlands and discusses implications for climate change mitigation related to the management of ecosystems like these. Moreover, methodological challenges concerning the processing of trace gas fluxes measured with the eddy covariance (EC) technique (see section 2.2 for details) are addressed. In particular, strategies for gap-filling of greenhouse gas (GHG) time series and the impact of different scales of surface inhomogeneity on EC gas fluxes are explored.

The Rio Pipo investigation site is located in southernmost Patagonia on Tierra del Fuego, Argentina (54.8° S). The second site, Himmelmoor, is situated in NW-Germany (53.7° N) close to the city of Hamburg. Both sites developed as rainfed peatlands, can be classified as raised bogs (Hammond, 1981) and lie within temperate climate zones. Yet, some of the two sites' features are very much contrasting. Rio Pipo is a living (i. e. peat accumulating) peatmoss dominated mire, whereas Himmelmoor has been shifted distinctly from its pristine state due to peat mining.

From an ecological perspective, the two investigated peatland sites differ in their land use state. Rio Pipo bog is pristine, whereas Himmelmoor is degraded. Rio Pipo can be regarded as a reference for comparison to evaluate how far degradation has shifted Himmelmoor from its former pristine state. Moreover, Rio Pipo carbon gas exchange balances outline a possible long-term future scenario of the climate change mitigation potential a transformation of Himmelmoor back into a peat-accumulating raised bog would implicate.

From a metrological point of view, the two sites differ with respect to the spatial scales on which surface variabilities are distributed throughout the EC footprint. On landscape-scale, Rio Pipo is very homogeneous regarding relief, water regime, vegetation cover and occurring plant species. Nevertheless, on decimeter to meter scale, patterning into hummocks, lawns and pools exists (Lehmann et al., 2016; Mark et al., 1995). In contrast, surface inhomogeneities in Himmelmoor display on landscape level. The site is divided in strips with contrasting properties that are several tens of meters wide and a few hundred meters long. The disparity in scales on which surface

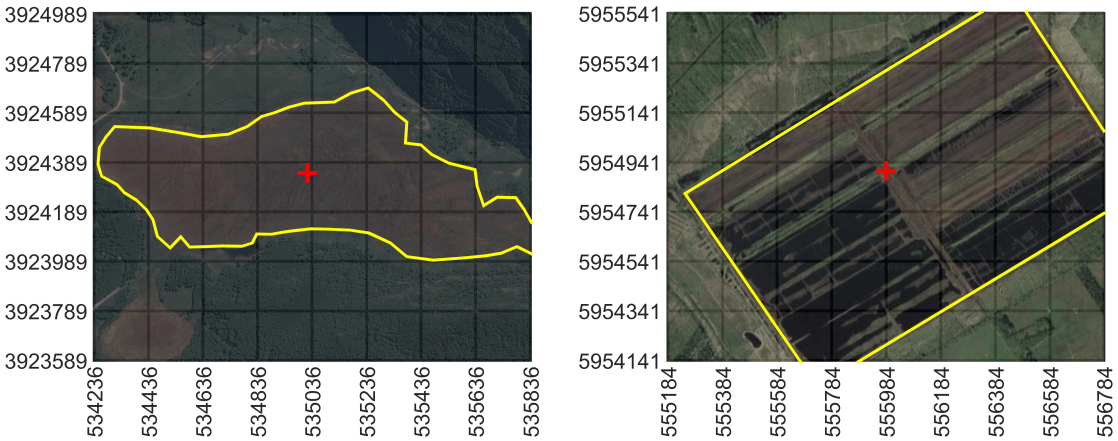

Figure 1.1: Satellite images of the investigation sites, Rio Pipo bog on the left panel and Himmelmor on the right-hand side. Rio Pipo serves as an example for a near pristine ecosystem, whereas Himmelmoor is under two types of management, peat mining and restoration. Coordinates refer to UTM zones 19 F on the left and to 32 U on the right. Grid spacing is 200 meters. (Images: Google, DigitalGlobe, 2015)

features vary becomes apparent in figure 1.1, where equally scaled satellite images of the two sites are compared. The questions addressed in this thesis can be related to two overriding topics: (1) The climate impact of peatland land use change and (2) time series modeling of EC gas fluxes measured over heterogeneous terrain. In particular, I followed up on the inquiries listed below.

- What is the best procedure for a reproducible selection of driving variables for accurate and robust empirical models (such as artificial neural networks, multilinear regressions or marginal distribution sampling methods) of gas flux time series?
- Is it possible to extract trace gas flux balances of individual surface classes from a complex EC flux times series measured over a heterogeneous peatland?
- Are the contrasting peatland management types also reflected in disparate carbon gas flux balances?
- How does the climate change mitigation potential of a former peat-mining site develop during the early phase of rewetting.

1.2 Contents overview

In the methods section, I present a data-driven decision-making framework for the selection of model inputs. I compare five different half-hourly flux models based on their explanatory power, their number of parameters and their generalization capability. I also give a structured approach to the choice of architectural properties for artificial neural networks (ANNs). Input and model selection are combined in the presented input-sensitive input and model selection (I-SIM) algorithm. The obtained model results are used to fill gaps in the methane flux (F_{CH4}) and carbon dioxide flux (F_{CO2}) time series. On the basis of a two year dataset from Himmelmoor, chapter 4 covers the method-

ological concepts with an emphasis on modeling of methane flux time series. By evaluating half-hourly footprint statistics (see section 2.2), the datasets are partitioned and gap-filled in order to calculate the annual sums of carbon gas fluxes on surface class level. These results are furthermore interpreted in a mechanistic way on microform level to evaluate if the produced surface class time series (SCTS) do contain reasonable information when related to plant physiological parameters. This mechanistic model is based on light saturation functions for photosynthesis and an exponential temperature-respiration relation. The continuous carbon gas flux time series are used to calculate annual sums of gas emissions comparing the two contrasting types of land use that are employed in Himmelmoor.

Seven month of carbon dioxide fluxes are available from Rio Pipo. These fluxes are also gap-filled using I-SIM and with an additional half-hourly mechanistic model. The methodological goal of this proceeding is to inquire into the comparison between simplifying mechanistic and more complex empirical models with respect to their explanatory power for EC fluxes over homogeneous terrain.

Finally, Carbon gas emissions from the the three examined peatland surface classes, that are distinguished by land use type, are collated. Implications for the management of peatlands regarding their climate regulation function are discussed. Results of I-SIM modeling are evaluated and interpreted for gas flux time series recorded over homogeneous and heterogeneous terrain. Additionally, I propose a new quality filter for raw methane concentration time series measured with LI-7700 (Licor, USA) open path methane (CH_4) sensors.

A synthesis of the results is presented in chapter 7. Synoptic answers to the initially posed research questions are given.

Chapter 2

Background

2.1 Links between land use and carbon flux dynamics of peatlands

Peatlands are wetland ecosystems that accumulate peat under water-saturated conditions. Peat formation is the result of an imbalance between production and decomposition of organic matter. For a peatland to qualify as a mire, the accumulation of peat has to be ongoing. The term peatland is defined broader and refers to soils that include an at least 30 cm thick peat horizon. Concerning long-term carbon sequestration, no other terrestrial ecosystems are as efficient as mires. Although peatlands cover only 3 % (400 million ha) of the Earth's land surface, they store 550 Gt carbon (Yu et al., 2010), which equals the amount of carbon stored in the entire terrestrial biomass and represents twice as much carbon as sequestered in the Earth's forests respectively.

Peatlands are characterized by complex interactions between vegetation, hydrology and peat and therefore are vulnerable to alterations of these factors by men or climate change. Traditional land use practices in peatlands are commonly paralleled by interference with the ecosystems' water regimes. Hydrological manipulations can fundamentally modify the carbon flux dynamics of peatlands, regardless if they are undertaken to prepare the area for commercial use (drainage) or to restore a "natural" state of the ecosystem (rewetting). Anthropogenic use of peatlands usually involves their drainage. The stored carbon is than oxidized and a C-sink is turned into a C-source. Per year at least 3 billion tons carbon dioxide (CO_2) (Parish et al., 2008) are emitted by degraded peatlands. This is equivalent to 10 % of the global annual emissions by the combustion of fossil fuels. The rewetting of formerly drained peatlands commonly reduces CO_2 emissions drastically and makes the re-establishment of a CO_2-sink possible on the long run (Alm et al., 2007; Beyer and Höper, 2015; Couwenberg, 2009a; Tuittila et al., 1999; Vanselow-Algan et al., 2015; Wilson et al., 2009, 2016). Under water-saturated conditions, however, the anaerobic decomposition of organic matter and thereby the production of the GHG CH_4 increases. Land use change of peatlands thus inheres the potentials to accelerate global warming as well as to mitigate climate change.

For a peatland to act as a CO_2 sink, the water level may fluctuate around the surface only to a minor degree. If it is too low, more plant litter is decomposed aerobically than is being produced. If it is too high, plant production is often inhibited, so that e.g. lakes commonly are carbon sources. At high water tables, CO_2 emissions are low (respectively negative when C is sequestered); with a decreasing water table they rise. Couwenberg et al. (2010) found a linear correlation between F_{CO2} and water table depth in a meta-analysis of flux data from temperate European peatlands. For sites with mean annual water levels above 40 cm below the surface, CO_2 emissions decrease with rising water tables. CH_4 emissions are also linked to the water table. At levels deeper than 20 cm below the surface, CH_4 emissions are negligible and increase with a rising water table. In case of inundation, diffusive CH_4 release is hampered due to the large difference in gas diffusivity of water and air. Moreover, CH_4 can be decomposed on its comparably slow way through the water column if enough dissolved oxygen is present. Two alternative mechanisms for the transport of pedogenic CH_4 to the atmosphere are known. CH_4 release via bubbles can account for a significant portion of the overall CH_4 emissions (Glaser, 2004; Goodrich et al., 2011; Strack et al., 2005). This process is referred to as ebullition and describes the sudden release of gas bubbles that accumulate in the soil pore space until their buoyancy is high enough for them to ascend to the surface. The importance of diffusion and ebullition declines with the presence of vascular plants. The soil and water volume can be bypassed employing plant mediated transport through the aerenchymae of vascular plants (Bubier, 1995; Whalen, 2005). Moreover, higher plants also provide labile dissolved organic carbon to the rhizosphere. These easily decomposable carbon compounds can act as a substrate for methanogenic microorganisms. F_{CH4} dynamics are therefore gravely impacted by vegetation cover and type.

Wilson et al. (2009) investigated the development of CH_4 emissions and modeled the course of CH_4 emissions for different land use types following peat extraction. The authors conclude, that by long-term inundation of peatlands formerly used for peat harvesting, the creation of a landscape scale methane hotspot is very possible. Nevertheless, the balance of avoided CO_2 emissions by restoration and newly created CH_4 emissions results in a net-reduction of the global warming potential (GWP) at the site Wilson et al. (2009) describe. When anaerobic conditions prevail after inundation, CH_4 production is mainly controlled by the availability of fresh organic matter (Couwenberg, 2009a; Lai, 2009; Saarnio et al., 2009) as well as soil and water temperature (Schrier-Uijl et al., 2010). Hahn-Schöfl et al. (2010) performed a chamber measurement campaign and incubation experiments on a rewetted former grassland fen in the Peene river valley in NE-Germany. The authors describe the formation of an organic sediment from the rotting former vegetation cover. The CH_4 production potential, which lies in the anaerobic

decomposition of this substrate, is very high. Tiemeyer et al. (2016) investigated GHG release from 48 grassland sites on drained fens and bogs in Germany. They report high CH_4 emissions from relatively nutrient-poor and acidic sites. Incubation experiments from Hahn-Schöfl et al. (2010) show that bare peat is comparatively inactive. This finding is confirmed by Wilson et al. (2016) for drained as well as rewetted bare peat surfaces in temperate peatlands. In case of a vegetation-free restored peatland site, the risk of CH_4 production depends on which plants are established or colonize the site respectively. Thereby, it is critical how easily decomposable the delivered organic matter is and if plant mediated methane transport via their aerenchyma (Whalen, 2005) occurs. Furthermore, CH_4 production is negatively correlated with the availability of other electron acceptors like iron or sulfate.

2.2 State of the art: Trace gas flux measurement techniques

Two main methods for measuring trace gas fluxes are frequently described in literature: the EC method and the chamber method. With a manual chamber method, the air volume in a closed chamber is sampled over time. Gas can be extracted with syringes and analyzed in the lab employing gas chromatography. Alternatively, the chamber air can be circulated through an on-site infrared gas analyzer. A common sampling frequency of these kinds of devices is 1 Hz. With an area coverage of typically less than 0.5 m^2, the spatial resolution of this technique is very high. However, the temporal resolution of a manual chamber method is sparse. Direct measurement of trace gas, energy and momentum fluxes can be provided by the EC method. Wind blowing over a rough surface produces turbulently moving air parcels called eddies. Relating to small time scales, an eddy can be regarded as being confined in space. The atmospheric layer that is influenced by the surface relief within a time horizon of several hours is called atmospheric boundary layer (ABL) (Garratt, 1994; Stull, 1988). Sinks and sources of energy or matter at the surface create vertical gradients of those features in the ABL. Turbulent mixing leads to a net vertical transport of these entities. The turbulent transport of energy, momentum and matter in the ABL is orders of magnitude more effective than diffusive transport (Lee et al., 2004). The movement of gas molecules along the vertical velocity component of eddies mainly causes their exchange between surface and atmosphere. Fluctuations of gas concentrations and three-dimensional wind speed can be determined with an eddy covariance setup at a sampling rate of 20 Hz and can therefore be seen as quasi-continuous. Depending on anemometer height, the EC method provides flux data integrated over a landscape scale area. Moreover, in a setting where the EC data contains signals from various surface classes, the contribution of each class to the total signal can be modeled. Different methods

for computing this so called footprint are described in literature (Hsieh et al., 2000; Kljun et al., 2004; Kormann and Meixner, 2001). In combination with a surface classification, fluxes can be associated to and evaluated separately for different microforms within the EC footprint (Forbrich et al., 2011). The spatial resolution of the computed surface class contributions relies on the pixel size of the available classification and can for example be as low as 1 m^2 if satellite footage is used. If reliable small-scale flux time series can be estimated depends, however, on the size of and the contrast between the diverse surface features. Their size determines, in relation to the EC measurement height, the number of half-hours with almost exclusively one class in the EC footprint.

The earliest direct landscape scale CH_4 flux measurements date back to the 1990s. While Fan et al. (1992) used a sensor with a flame ionization detector, laser absorption spectroscopy (LAS) soon became the dominant technique (Suyker et al., 1996; Verma et al., 1992; Zahniser et al., 1995)). Various innovations in LAS, resulting in different instrument designs, have been made since then. Intercomparisons of the available sensors are given by Tuzson et al. (2010), Detto et al. (2011), Peltola et al. (2013) and Peltola et al. (2014). Besides high power consumption, the major drawback of early tunable diode laser spectrometers (TDLS) was the necessity to cool the lasers (e. g. with liquid nitrogen) and to frequently calibrate them leading to a high maintenance effort. Off-axis integrated cavity output spectroscopy (OA-ICOS) and wavelength scanned cavity ring-down spectroscopy (WS-CRDS) eliminated the need for cooling but rely on ultra-high reflective mirrors, limiting these techniques to closed path applications. Due to the required high flow rates and low cell pressures, these instruments still consume too much power ($\gtrsim$ 500 W) to make them suitable for sites without access to the power grid. McDermitt et al. (2011) presented an open-path sensor using wavelength modulation spectroscopy (WMS) that can operate at room temperature while consuming only little power ($\lesssim$ 20 W). However, as the measuring cell is exposed to the atmosphere, rain and dust on the mirrors can deteriorate the acquired data. Since methane is an important GHG and a crucial part of the carbon balance of many, especially wetland ecosystems, the development of fast sensors fostered plenty of research as it provided the possibility to measure long-term landscape scale methane fluxes with the eddy covariance technique at high temporal resolution.

2.3 State of the art: Trace gas flux time series modeling

Since the development of fast methane sensors, wetland carbon balances can be reported more comprehensively. However, to be able to calculate for example annual sums, gaps in the flux time series have to be filled first. Compared to modeling CO_2 fluxes, gap-filling of methane

fluxes is more challenging because the relations between environmental drivers and CH_4 flux often appear to be more intricate than for CO_2. Basic gap-filling methods include for example interpolation between measured values (Dengel et al., 2011; Hanis et al., 2013) or the use of an average to replace all gaps (Hatala et al., 2012; Mikhaylov et al., 2015). Simple linear models have also proven to be applicable in certain settings (Alberto et al., 2014; Hanis et al., 2013). A common approach is to fit Arrhenius-type non-linear functions to the flux as a function of various environmental drivers, what has been done for half-hourly data (Forbrich et al., 2011; Hommeltenberg et al., 2014; Kroon et al., 2010; Sachs et al., 2008, Goodrich et al. 2015a) as well as for downsampled time series (Brown et al., 2014; Friborg and Christensen, 2000; Jackowicz-Korczyski et al., 2010; Long et al., 2010; Mikhaylov et al., 2015; Parmentier et al., 2011; Rinne et al., 2007; Shoemaker et al., 2015; Suyker et al., 1996; Wille et al., 2008). In this respect, downsamplig refers to the procedure of fitting models to (e. g. daily) averages of higher frequency time series (e. g. 30 minute fluxes). Look-up tables (LUTs) have been applied by Pypker et al. (2013), Hommeltenberg et al. (2014) and Bhattacharyya et al. (2014). The mean diurnal variation (MDV) method described by Falge et al. (2001) for CO_2 has been employed to fill CH_4 time series by Dengel et al. (2011) and Jha et al. (2014).

A combination of the LUT and MDV methods presented by Reichstein et al. (2005), termed marginal distribution sampling (MDS), has found wide application in modeling of CO_2 fluxes. The practicability of the original MDS method for methane gap-filling has been explored by Alberto et al. (2014) and Shoemaker et al. (2015). In this study, I present a more general reformulation of the MDS algorithm, including the possibility to use other input variables than originally implemented by Reichstein et al. (2005) for CO_2 gap-filling.

Artificial neural networks (ANNs) form a category of non-parametric models that have frequently been used to fill gaps in EC CO_2 time series. Mostly, multilayer perceptrons (MLPs) were chosen (Järvi et al., 2012; Menzer et al., 2015; Moffat, 2012; Moffat et al., 2007; Papale and Valentini, 2003; Pypker et al., 2013) while other authors utilized radial basis function (RBF) networks (Kordowski and Kuttler, 2010; Menzer et al., 2015; Schmidt et al., 2008). For CH_4 fluxes, MLP models are described by several authors (Dengel et al., 2013; Deshmukh et al., 2014; Knox et al., 2015, Goodrich et al. 2015a) as well as a special kind of RBF network, a generalized regression neural network (GRNN), by Zhu et al. (2013).

In light of the diverse modeling approaches that have been successfully applied in literature, the question remains, how to decide which model is an adequate choice for a particular dataset. Furthermore, not only the model type but also the input variables, which ideally contain information about the driving processes of the flux, have to be decided for. Both decisions have an impact on model complexity and should not be made arbitrarily. The

more complex a model is, the more variability in the data it can potentially explain. For noisy target data, this can lead to a model mainly reproducing the noise and missing physically meaningful relationships between input and output that are valid in a general sense. A lack of generalization capability is problematic when using an overfitted model for time series gap-filling. Values of low accuracy and high precision would be introduced into the dataset and potentially create a bias when for example cumulative flux sums are reported.

2.4 A brief history of peatland research on Tierra del Fuego - Can fuegian mires be regarded as pristine?

Tierra del Fuego has been subject to ecological research for centuries. Among many famous visitors, Charles Darwin, who reached the fuegian archipelago aboard the Beagle navigated by Captain Fitz Roy in 1832, probably stands out the most. Before him, Philibert Commerson (1767), Joseph Banks and Daniel Solander during James Cook's first voyage to the region as well as Johann Reinhold Forster and his son Johann Georg Adam Forster who accompanied Cook during his second expedition between 1772 and 1774, have contributed a significant amount of information primarily on the prevalent flora of Tierra del Fuego. During the 19th and into the early 20st century various international expeditions from Europe, Asia, North and South America reached southern Patagonia, what led to a further completion of the botanical inventories of the contrasting ecosystems that can be found in this region. Scientist from this era include for example Joseph D. Hooker, Per Dusén, Otto Nodenskjöld, Carls Skottsberg, Carl Caldenius and Giacomo Bove (Tuhkanen, 1990). More recent and yet more complete descriptions of fuegian flora are given by Moore and de Goodall (1983) and Roig (1998). A major advance in the biogeochemical exploration of Tierra del Fuego is marked by the expeditions the Geographical Society of Finnland sent under Väinö Auer's leadership. Between 1928 and 1952 he conducted a total of 15 extensive sampling and mapping campaigns in the region. The results obtained with these data cover multiple scientific fields like botany, mesozoic tectonics, quaternary geology, paleoecology, paleoclimatology and volcanology. Auer himself was the researcher who established the view on fuegian peatlands how it is predominant in scientific literature until today. He analyzed 70 bog profiles throughout the archipelago focusing on the archive function of peatlands. From the pollen records of the profiles he drew conclusions about past shifts in ecological boundaries that he attributed to fluctuating climatic conditions, sea level changes and volcanic eruptions. For this purpose he also used volcanic ash layers preserved in peat and by that pioneered the application of tephrachronology for quaternary geology. Since Auer's times, peatlands have often been studied by ge-

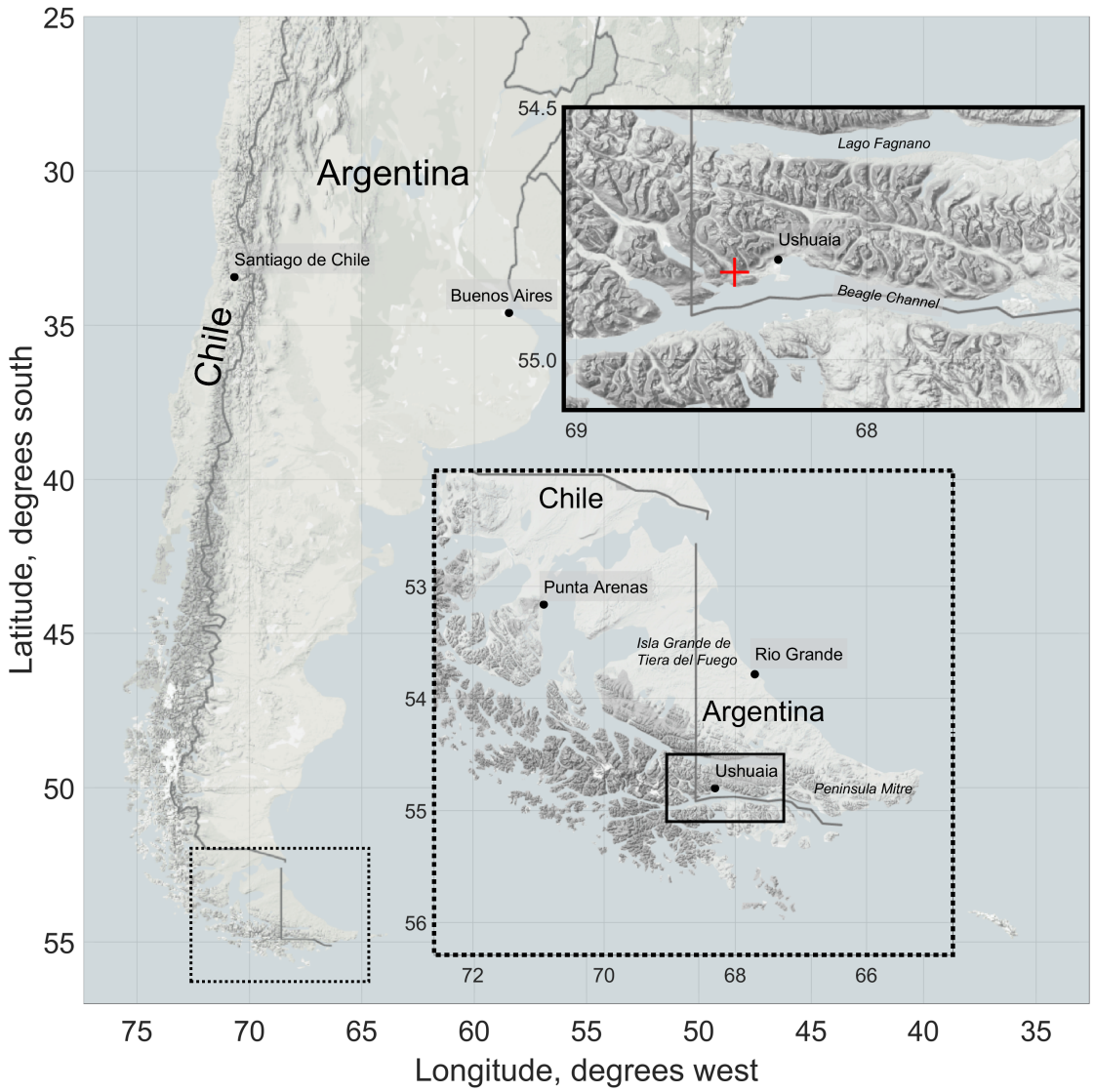

Figure 2.1: Location of the Rio Pipo investigation site at the Beagle Channel on Tierra del Fuego in Argentina. (Map data: Google, Digital Globe, 2016)

ologists to yield information on the Pleistocene and Holocene that they contain (e. g. Heusser, 1993; Rabassa et al., 2000, 1989, 2006). More recently, the focus of publications in this discipline has shifted towards the east (Penisula Mitre and Isla de los Estados), beyond the extend of the last glaciation (Björck et al., 2012; Heusser, 1995; Ponce et al., 2016; Ponce and Fernández, 2014). Also the interest of ecologist in the peatlands of Peninsula Mitre has grown (Fritz et al., 2011; Grootjans et al., 2014; Iturraspe, 2012). Data on the occuring peatland types and their distribution across Tierra del Fuego has been gathered and/or compiled for example by Roivainen (1954), Auer (1965), Pisano (1983), Tuhkanen (1990), Rabassa et al. (1996), Roig et al. (2001), Blanco and de la Balze (2004), Moen et al. (2005), Mauquoy and Bennett (2006), Iturraspe (2010) and Grootjans et al. (2010). In general, shifts in peatland types follow the steep climatic east-west gradient that is caused by the mountain range of the Andes and the Cordillera Darwin foremost affecting the distribution of precipitation. While prevailing winds come from the west-northwest year-round, the relief divides southern Patagonia in a very moist western part (up to 5000 mm yr^{-1}) and a steppe (below 300 mm yr^{-1}) (Tuhkanen, 1992). However, local precipitation and wind conditions can be heavily influenced by smaller scale relief features of the landscape. At the pacific coast on Islas de los Evangelistas (52°24' S, 75°06 W) for example, the average annual wind speed is 12 m/s coming from the northwest, whereas Ushuaia experiences mainly southwesterly winds with an annual average of around 4 m/s (Tuhkanen, 1992). In general winds are stronger in spring and summer than in winter. Plant-ecology is, however, not mainly impacted by the speed of the winds but by the merciless constancy with which they sweep across the region (Weischet, 1985).

The fuegian landscape as a whole has been termed magellanic moorland or magellanic tundra complex (Pisano, 1977, 1983) and in particular consists of extended wetland areas interlinked with forests. In the dry northern and central Isla Grande de Tierra del Fuego seasonally flooded vegas (termed "Steppenmoore" by Auer) that lack the presence of peat mosses can be found. Raised *Sphagnum magellanicum* bogs are distributed throughout the central and marginal cordilleran valleys and roughly follow the distribution of *Nothofagus pumilio* forests (Tuhkanen, 1990). Cushion bogs (termed "Polstermoore" by Auer) dominate the wet pacific coast but also extensive parts of Peninsula Mitre in the east of Isla Grande and the archipelagic region south of the Beagle Channel on Chilean territory. These cushion bogs form a unique type of peatlands, exclusively found on the southern hemisphere. They grow in similar relief settings like blanket bogs. Their main peat forming species, however, are not mosses but vascular plants like *Astelia pumila* and *Donatia fascicularis*. More similar to northern hemisphere bogs are the raised *Sphagnum* bogs. Biodiversity in these systems is, however, very low in comparison to their northern counter-

parts. They can be inhabited by as little as 10 vascular plant species (Moen et al., 2005). Their vegetation community consist nearly completely of one moss species: *Sphagnum magellanicum*. Apart from that, only two other peat mosses commonly occur in transitions to fens (*S. fibriatum*) or in pools (*S. cuspidatum*) as stated by Kleinebecker et al. (2007). The magellanic moorland covers an area of 44 000 km^2 (Arroyo et al., 2005) of which 2700 km^2 are located on Argentinen territory (Iturraspe, 2012).

Gas flux measurements in fuegian peatlands have only been done twice and with manual chambers. Fritz et al. (2011) measured methane fluxes six times on three days representative for spring, summer and autumn in a cushion bog on Peninsula Mitre close to the Beagle Channel. Lehmann et al. (2016) investigated methane fluxes during four summer days from the Rio Pipo raised *S. magellanicum* bog near Ushuaia, the exact same site the data presented here was collected. Carbon dioxide flux measurements of any fuegian ecosystem have not been reported so far. Carbon balances of southern hemisphere peatlands are scarce in general. Only recently, comprehensive CO_2 (Goodrich et al. 2015b; Campbell et al., 2014) and CH_4 (Goodrich et al. 2015a) flux records have been reported from New Zealand. The ombothrophic raised bogs described there are dominated by the rush *Empodisma robustum*, distinguishing them from most global bogs that are commonly dominated by peat mosses.

Some authors have already stressed the importance of fuegian ecosystems as a basal reference to their anthropocenically altered global counterparts. Studying these landscapes allows for a ”glimpse of pre-industrial environments” as Kleinebecker et al. (2008) put it in their biogeochemical analysis of peat samples from an west-east Andean transect (53°S). Fritz et al. (2011) estimated nitrogen deposition to be very low at 0.1 g m^{-2} a^{-1} inferring this number from data published by Godoy et al. (2003) about the Pacific coast of Chilean Patagonia. There is, however, evidence that the pristine state of the magellanic region is in jeopardy. Using lichens as a biomonitor, Conti et al. (2012) analyzed the atmospheric deposition of trace metals at the Atlantic coast of Isla Grande close to the industrial capital of the island, the city of Rio Grande. Although the levels of pollution were comparably low in general, the authors measured beginning trace metal contamination which they attributed mainly to the atmospheric deposition of soil particles. Overall, the authors conclude that Tierra del Fuego is suitable as a reference whose ecosystems can be regarded as being only little affected by industrial progress. In context with the data analyzed in the present study, it is important to note that the reference material for the comparison of Conti et al. (2012) was taken from Parque National Tierra del Fuego where the Rio Pipo bog is located, too. In this respect, atmospheric contamination of trace metals appears to be limited to the industrial northeast of Isla Grande. Biester et al. (2002) investigated the accumulation of heavy metals in a cushion bog profile at the Chilean Pacific coast (53°S). With 2.5 fold elevated

mercury accumulation rates compared to pre-industrial times, they found a clear anthropogenic signal at this site. This signal was not present in Pb concentrations though, what in turn proves the high mobility of gaseous Hg from anthropogenic sources and the extreme distances Hg can cover as opposed to other metals.

pontaneous ebullition (hot moments) can in particular be determined robustly using these techniques concurrently.

Chapter 3

Study Areas

3.1 Rio Pipo

Rio Pipo mire is located at 54.83°S, 68.45°W in Parque Nacional Tierra del Fuego. The mire is a raised *Sphagnum magellanicum* bog as they are typical for the wind protected western valleys of Tierra del Fuego (Iturraspe, 2012). It covers an area of around 60 ha at the southern end of a glaciogenic valley bottom. The valley stretches to the SE and is drained by the Rio Pipo river, which marks the northern margin of the bog. Along its southern border, a rather narrow lagg zone forms the transition to the adjacent upwards sloping *Notofagus pumilo* forest. *S. magellanicum* is with a surface cover of around 40 % (Lehmann et al., 2016; Mark et al., 1995) the most abundant plant species. It occurs in wet lawns and forms roughly N-S oriented chains of hummocks perpendicular to the drainage direction. Alternating strips of lawns with pools and hummocks compose most of the peatland's surface. The drier hummocks are commonly covered by the dwarf-shrub *Empetrum rubrum* and the rush *Marsipospermum grandiflorum* (Lehmann et al., 2016).

The mean annual temperature at the closest longterm meteorological station in Ushuaia is 5.5 °C (Iturraspe, 2012), where annual precipitation ranges from 530 mm (Iturraspe, 2012) over 545 mm (Pisano, 1977) to 574 mm (Tuhkanen, 1992). To date, the data collected for this thesis covers 7 months and includes precipitation as well as temperature measurements. Between February and September the mean air temperature was 5.1 °C with a maximum of 21.7 °C on March 3rd and a minimum of -5.6 °C on August 8th. Mean June temperature was 5.0 °C, which is considerably higher than the long-term average of 1.2 °C given by Iturraspe (2012) for Ushuaia. Precipitation records sum up to 287.8 mm within seven months. Wind came almost exclusively from west-northwestern directions, hence from the valley.

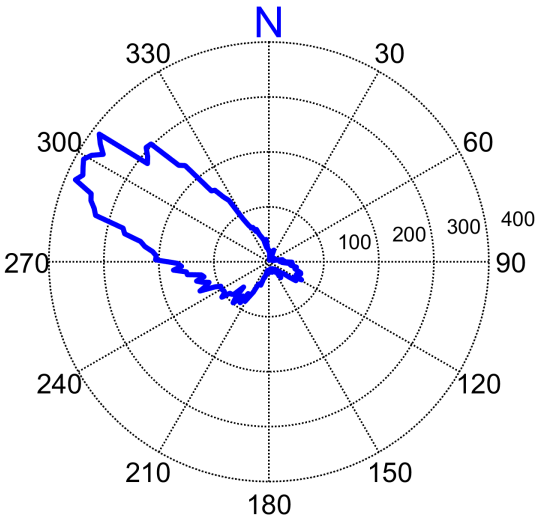

Figure 3.1: Polar thirty minute wind directions histogram illustrating EC source area homogeneity at the Rio Pipo site.

3.2 Himmelmoor

Himmelmoor is a temperate bog that has been heavily degraded by peat mining. The site is located in NW Germany, 3 km west of Quickborn in Schleswig-Holstein (53°44'23.3" N, 9°50'55.8" E). Along with the adjacent grassland-fen of the Bilsbek lowland and the beech-dominated forest stand Kummerfelder Gehege, Himmelmoor forms a nature reserve according to the EU Fauna Flora Habitat Guideline (FFH) and is also protected by federal law of Schleswig-Holstein as a core area of the local biotope network (Zeltner, 2003).

The bog developed in a river valley, which was pre-formed as a glacial meltwater valley during the Weichselian glaciation in the depressed fringe of a salt dome. Peatland formation from a standing water body began 10.020 $\pm$ 100 years BP (Pfeiffer, 1997). Following the deposition of lake sediments, a Phragmites-Carex fen and a subsequent birch forest formed. Around 8000 BP a rising groundwater level led to the extinction of the forest vegetation and to the spread of *Sphagnum spp.* peat mosses. Industrial peat extraction began in the 132 ha large (Grube et al., 2010) central bog area in the mid 19th century. The extraction site is divided into two halves by a NNW-SSE running railroad dam. Areas on the western half have been stepwise taken out of operation by the local peat-mining company since 2008. The eastern part was still being harvested during the measurement period , whereas most of the western section was rewetted, apart from a 90 m wide strip in the northwest (see figure 3.2). These areas of opposing water regimes and land use will be referred to as surface class *drained* (SC_{dra}) and surface class *rewetted* (SC_{rew}) throughout this text. In 2016, more than half of the eastern section has also been rewetted by ditch blocking. Peat extraction will be completely ceased in 2017. 400 ha of the 600 ha bog area are suitable for restoration according to the FFH site description.

The soil properties of the research site were altered by peat decomposition and subsidence during decades of drainage and peat extraction. The former acrotelm layer is missing. Thereby the peatland's ability to self-regulate the water table for optimal peat forming and carbon sequestering conditions is lost. The performed ditch blocking leads in the early years of rewetting ($<$ 5 years, own observation) to an oscillating water table over the course of the season. The alternating conditions from oxic (water table low, summer) to anoxic (water table high/inundation, win-

ter) might facilitate bacterial decomposition and prevent self intoxication (Beer and Blodau, 2007). The leaching of reaction products at high water levels could hamper the slowing down of decomposition. Overall, the peat's varying physical properties lead to changing chemical conditions that could amplify GHG production and dissolved organic matter export at the same time.

Himmelmoor drains into the two local creeks Bilsbek and Pinnau. The water added to the peatland originates from precipitation and from a series of ditches, that were dug between 1950 and 1968 (Czerwonka and Czerwonka, 1985) and that are distributed regularly across the central bog area. Some of these diggings reached below the peatland base and penetrate the mineral ground. The ditches were later refilled with peat but still provide a connection to the aquifier beneath, from which minerotrophic groundwater is supplied. Today, fen-type vegetation is covering these strips which will be referred to as surface class *vegetated* (SC_{veg}). They are between 600 and 700 m long in ENE-WSW direction and 20 to 50 m wide in NNW-SSE direction. The plant community of SC_{veg} includes *Betula pubescens*, *Salix spp.* (presumably *Salix aurita* and *Salix caprea*), *Eriophorum vaginatum*, *Eriophorum angustifolium*, *Molinia caerulea*, *Calla palustris*, *Typha latifolia*, *Carex spp.*, *Juncus effusus* and *Calamagrostis pseudophragmites*. The long-term (2000 – 2014, Deutscher Wetterdienst, DWD) average annual precipitation is 888.0 mm, the mean air temperature is 10.1 °C. Both investigated years were considerably wetter compared to the long-term average, while precipitation in Year 2 was lower than in Year 1. In Year 1 the relatively high cumulative precipitation can mainly be attributed to heavy rain in early summer. The differences in mean annual air temperatures are mainly accounted for by deviating winter temperatures. In Year 2 they were well above and in Year 1 below average.

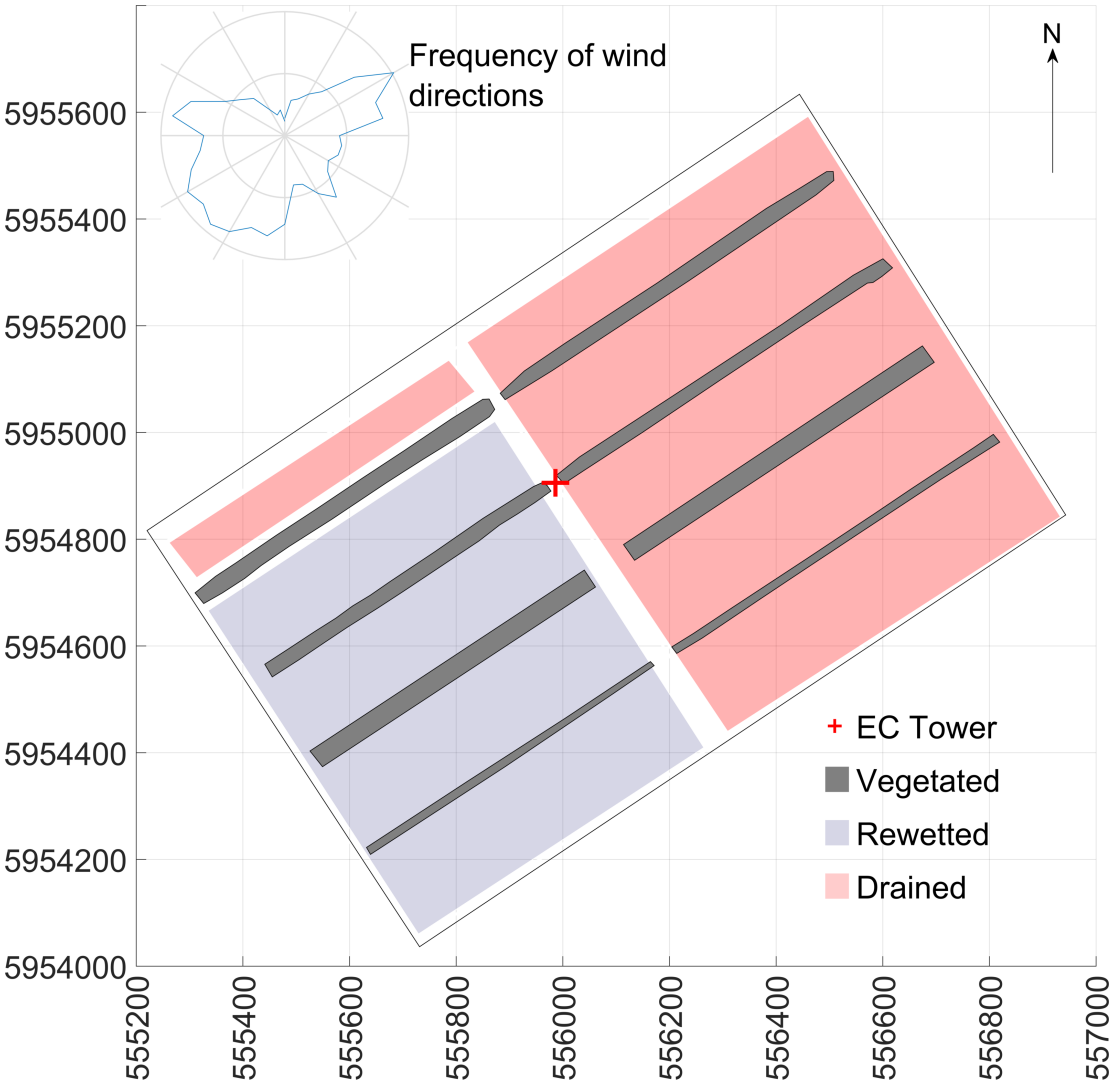

Figure 3.2: Distribution of surface classes *rewetted*, *drained* and *vegetated* in Himmelmoor. The map section shows the central extraction area. Grid spacing is 200 m, coordinates refer to UTM zone 32U. The polar histogram in the top left corner displays two years of half-hourly wind direction measurements binned in 2° classes.

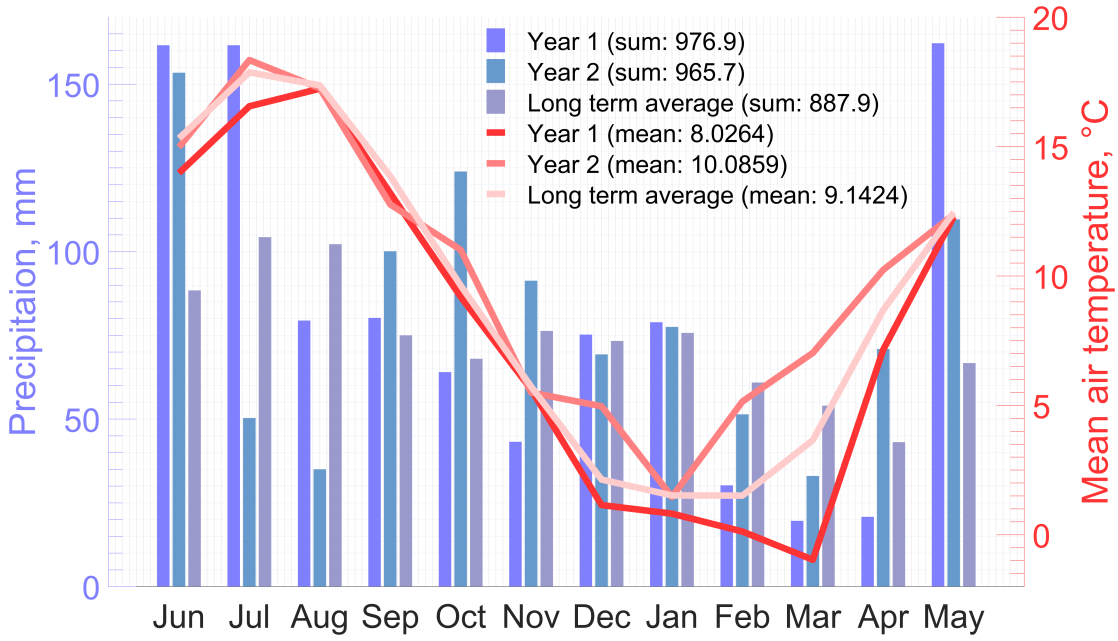

Figure 3.3: Climate diagram of the two investigated years from 06/2012 to 05/2013 and form 06/2013 to 05/2014 as measured in Himmelmoor and a 14 year average of a nearby DWD station (WMO-Station ID 10146 in Quickborn).

Chapter 4

Material and methods

4.1 Instrumentation

4.1.1 Himmelmoor

EC methane fluxes were measured using an open path CH_4 analyzer (LI-7700, Licor, USA) and a 3-D sonic anemometer (R3, Gill, UK) mounted on a tower at 6 m height. 20 Hz water vapour and carbon dioxide concentrations were determined with an enclosed path CO_2 and water vapor sensor (LI-7200, Licor, USA). The data was recorded on a LI-7550 (Licor, USA) logger. Additionally, a HMP45 (Vaisala, Finland) temperature and relative humidity probe was mounted on the eddy covariance tower and logged with the same device. A second HMP45 was installed together with a NR01 4-component net radiometer (Hukseflux, Netherlands) 70 m southwest of the EC tower on a tripod at 2 m height. These data were logged on a CR-3000 (Campbell Scientific, UK). Another logger of this type was used at the weather station approximately 500 m northeast of the EC-Tower. The sensors there included a third HMP45 and a tipping bucket rain gauge (R.M. Young, USA). Per depth, redox potentials were determined with three parallel probes and recorded on a Hypnos II (MVH Consult, Netherlands). The redox probes were installed in a vegetated strip approximately 100 meters west of the EC tower. Water level was measured and logged with a Mini-Diver (Schlumberger Water Services, USA) around 150 m west-southwest of the EC tower. Rain and long-term temperature data as presented in figure 3.3 was taken from a nearby station operated by DWD (WMO-Station ID 10146), which is located east-southeast from the EC tower at approximately 2.4 km distance.

Two years of turbulent flux data were available for analysis from Himmelmoor. The EC setup did not change during that time. The first year from June 1st 2012 to May 31st 2013 is from hereon called Year 1, the second year from June 1st 2013 to May 31st 2014 is termed Year 2.

4.1.2 Rio Pipo

The eddy covariance system to measure turbulent CO_2 fluxes consisted of a Windmaster Pro sonic anemometer (Gill, UK), a LI-7200 infra-red gas analyzer and a LI-7550 data logger (Licor, USA). Additional atmospheric and soil variables were recorded on a CR-3000 data logger (Campbell Scientific, UK). Air relative humidity and temperature were determined

with a HC2-S3 probe (Rotronic, CH), photosynthetically active radiation with a SKP-215 sensor (Skye Instruments, UK), precipitation with a ARG 100 raingauge (EML, UK), incoming and outgoing short- and longwave radiation with a NR-01 radiometer (Hukseflux, NL), ground heat flux with HFP01 heat flux plates (Hukseflux, NL), soil volumetric water content with CS616 water content reflectometers (Campbell Scientific, UK) and soil temperature with PT100 probes (Campbell Scientific, UK). Soil variables were recorded at three different microsites: One hummock and two lawns. Of the latter, one is dominated by *Empetrum rubrum* the other one by *Sphagnum magellanicum*.

Data from Rio Pipo presented in this study were collected between February 8th 2016 and September 12th 2016.

4.2 Raw data processing

Turbulent fluxes were computed using the software EddyPro 5.2.1 (Licor, USA). Raw data processing included (1) an angel of attack correction, i. e. compensation for flow distortion induced by the anemometer frame (Nakai et al., 2006), (2) coordinate rotation to align the anemometer x-axis to the current mean streamlines (Kaimal and Finnigan, 1994, double rotation), (3) linear detrending (Gash and Culf, 1996), (4) time lags compensation (see below for details), (5) spectral corrections (see below for details) and 6) WPL-correction to compensate for air density fluctuations due to thermal expansion or water dilution (Burba et al., 2012).

Time lags were compensated for by using the automatic time lag optimization (ATLO) option in EddyPro. For this procedure, prior to processing the complete dataset, time lags are determined for a subperiod of raw data by covariance maximazation. The median of the found time lags is called nominal time lag (T_{nom}), a searching window around T_{nom} is given by $T_{nom} \pm 3.5 \cdot MAD$, where MAD is the median absolute deviation of the found time lags. When processing the complete dataset, EddyPro performs a covariance maximization of vertical wind speed and the scalar of interest for each half hour and then checks whether the found time lag falls within the previously defined searching window. If not, T_{nom} is used as timelag. Water vapor concentration is binned in ten RH-classes, and the procedure is applied to each class, so there are ten different nominal time lags for water vapor. CH_4 and CO_2 concentrations are not binned in humidity-classes.

Spectral attenuations of the high and the low frequency range were both compensated for. Low frequency loss due to finite averaging time and linear detrending was corrected for following Moncrieff et al. (2004). In order to obtain a correction factor for each flux value, true cospectra were estimated as proposed by Kaimal et al. (1972) and reformulated by Moncrieff et al. (1997) for each half hour. Frequency-wise multiplication with a transfer function yielded an estimate of the filtered signal in the frequency domain. The transfer function was selected according to the used detrending method as given by Moncrieff et al. (2004). After integrating over the averaging period, a

low-cut spectral correction factor for each raw flux could be calculated. High frequency loss due to path averaging, signal attenuation and finite time response of the instruments was accounted for following Fratini et al. (2012). First, the cut-off frequency (f_c) and natural frequency (f_n) were determined by fitting the amplitude response of a first-order low-pass filter ($H_{IIR}(f_n/f_c)$) to the power spectrum of the respective scalar time series (Ibrom et al., 2007). For water vapour, f_c was estimated for nine relative humidity classes. Correction factors F1 were calculated with two methods depending on sensible heat and latent energy flux being above (high fluxes) or below (low fluxes) the thresholds of 10 and 5 W m^{-2} (Fratini et al., 2012). For high fluxes the correction factors were calculated after Hollinger et al. (1999) as implemented in EddyPro since version 5.2.0. Their calculation includes the degradation of the unattenuated sensible heat flux cospectrum by multiplying it with $H_{IIR}(f_n/f_c)$ for the previously determined f_c. For low fluxes, the obtained F1, f_c dataset was fitted to the model given in Ibrom (2007) for stable and unstable conditions. After obtaining the model parameters, F1 can be calculated for individual half hours as a function of f_c and mean wind speed. Spectral losses due to crosswind and vertical instrument separation were corrected for following Horst and Lenschow (2009).

4.3 Flux quality screening

Thirty minute fluxes were screened for quality according to the following scheme. Atmospheric stability and developed turbulence were analyzed as described by Mauder and Foken (2004). By this step, fluxes were classified into three groups: high quality fluxes (MF0), intermediate quality fluxes (MF1) and low quality fluxes (MF2). carbon gas fluxes flagged with MF1 and MF2 were discarded. Due to potentially faulty WPL correction, methane and carbon dioxide fluxes of half-hours where sensible or latent heat flux were flagged with MF2 were discarded as well.

Certain quality flags that were derived from raw data statistics as described by Vickers and Mahrt (1997) were evaluated. If skewness or kurtosis of vertical wind or sonic temperature were assigned a hard flag (skewness outside [-2,2], kurtosis outside [1,8]) or if CH_4 or CO_2 concentration statistics were rated with a soft flag (skewness outside [-1,1], kurtosis outside [2,5]), trace gas fluxes where discarded. Furthermore, half-hourly fluxes were rejected if the respective 20 Hz concentration time series failed the amplitude resolution test.

Additionally, diagnostic values from the LI-7700 and LI-7200 gas analyzers were used for quality screening. LI-7200 data was omitted when the signal strength indication (AGC) lay above 63. Due to a change in the signal quality definition along with a software upgrade, this rule was modified to discarding data below a value of 75 for data acquired when the sensor was running on firmware version 6.6 and above. With respect to the LI-7700, the relative signal strength indication (RSSI) and the heater diagnostics were evaluated. As a first step, methane fluxes were discarded if the mean RSSI of the respective averaging interval was

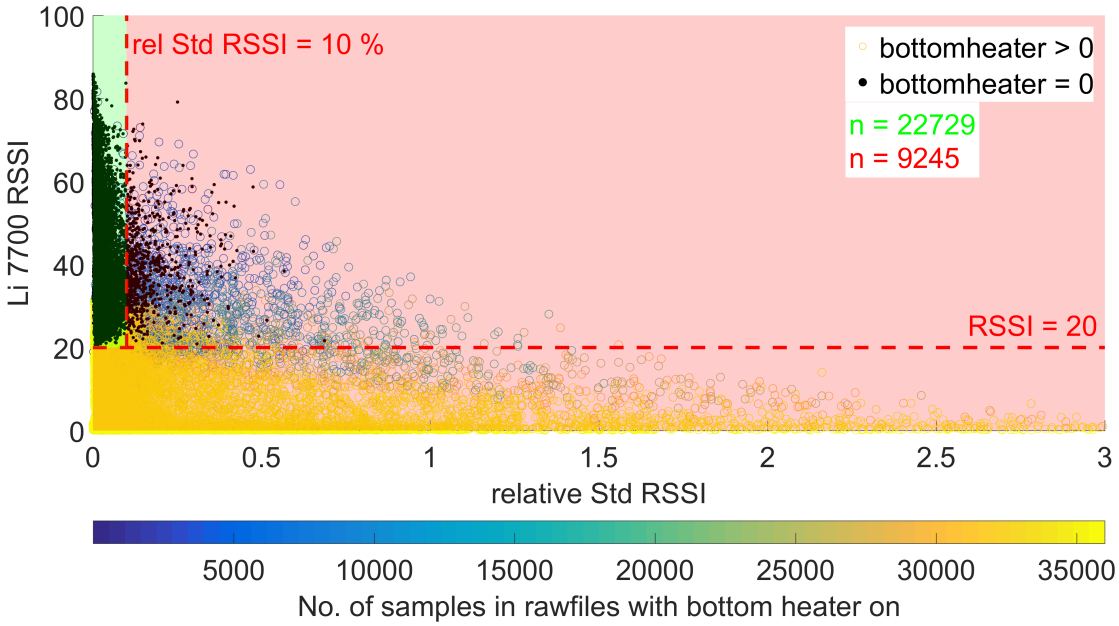

Figure 4.1: Illustration of the empirically derived threshold for the new LI-7700 open path methane analyzer quality filter. This check evaluates raw 20 Hz RSSI statistics to remove erroneous half-hourly methane fluxes. The filter is designed to capture concentration time series that were deteriorated by switching events in a LI-7700 mirror heater. Black data points denote half hours, during which the heater of the bottom mirror was switched off entirely. Colored points represents half hours, during which switching events (maximum: 36000) in the 20 Hz time series occured.

below 20. The bottom and top mirror of the gas anlalyzers measurement cell can be heated to counter condensation and frost on the mirrors. The Li-7700 instrument software allows for user defined thresholds that control the power-on of the heaters. For the bottom heater a RSSI threshold $RSSI_{th}$, below which the heater is turned on, can be adjusted. For the top heater an ambient temperature offset threshold $T_{a,\,offset}$ can be defined. This mirror is heated to keep its temperature about $T_{a,\,offset}$ above ambient temperature. In the present case, $RSSI_{th}$ was set to 20 and $T_{a,\,offset}$ to 1 °C. The number of samples within one half hour, for which a heater is switched on, is recorded. Accordingly, these diagnostics (bottom heater on: BH_{on}; top heater on: TH_{on}) take maximum values of 36000 if a heater is switched on for an entire half hour. Heater diagnostics were investigated closely due to the observation that within an averaging interval, high variation in RSSI was often accompanied by switching events in the 20 Hz heater time series, i.e. if BH_{on} or TH_{on} were neither 0 nor 36000. Moreover, methane concentrations had the tendency to covary with RSSI values if the latter showed large changes, what renders calculated fluxes hardly trustworthy. In general, the top heater was switched on most of the time whereas switching events in the BH_{on} time series where more common, which is why I mainly focused on the bottom heater diagnostics for the analysis of this phenomenon. Figure 4.1 shows the relationship between half-hourly averaged RSSI values, the corresponding rel-

ative standard deviation of 20 Hz RSSI ($RSSI_{relStd}$) values and BH_{on}. From this graph, I empirically derived a $RSSI_{relStd}$ threshold of 10 % , above which the respective flux records where neglected.

The next quality screening step was only applied to the Himmelmoor dataset. I first classified the surface using georeferenced orthoimages of the area. As the surface types I aimed to discriminate were quite large and easily distinguishable on the images, I could draw polygons around the different classes and get the coordinates of their corners. This step was implemented through the Matlab 8.4 Mapping and Image Processing Toolboxes. I defined the classes SC_{dra}, SC_{rew} and SC_{veg}, the latter of which is contained in the other two surface types. Calculating a 2-D footprint function after Kormann and Meixner (2001) with 1 m^2 resolution and summing up the contribution values of all pixels within each of the three surface types, yielded half-hourly contribution fractions of the different classes to the EC signal (class contribution of *rewetted* surfaces (CC_{rew}); class contribution of *drained* surfaces (CC_{dra}); class contribution of *vegetated* surfaces (CC_{veg})). CH_4 fluxes of half hours when $CC_{rew} + CC_{dra} < 30$ % were discarded. Thereby, flux data mainly related to the railroad dam and to areas outside the minig site were excluded.

Fluxes were then filtered for absolute limits. CH_4 data outside [-100 1000] nmol m^{-2} s^{-1} and CO_2 data outside [-10 10] µmol m^{-2} s^{-1} were neglected. The interval was left wider at [-20 20] µmol m^{-2} s^{-1} for Rio Pipo CO_2 fluxes. In case of the CH_4 flux time series, outlier removal was addresed furthermore by assessing the frequency distribution of the remaining data. Values smaller than the bin center of the 1st (BC_1) or larger than the 99th percentile's bin center (BC_{99}) were omitted. As a last step, CH_4 fluxes with random uncertainties calculated with EddyPro after Finkelstein and Sims (2001) larger than 400 nmol m^{-2} s^{-1} were filtered out.

4.4 Empirical gap-filling

4.4.1 Introduction

In order to fill gaps in the carbon gas flux time series from Himmelmoor, five different models were applied and compared. The tested model types include parametric and non-parametric varieties and range from predictions of multilinear systems to ANNs. Moreover, a data-driven evaluation of possible model inputs was developed and aggregated within an automatable decision-making framework. As input vectors, the routine accepts measured environmental variables, EC footprint information and artificial transformations of cyclicality expressed in fuzzy logic. Input selection and model evaluation are combined in the I-SIM algorithm.

4.4.2 Multilinear regression

I applied a stepwise multilinear regression (MLR), utilizing a combination of forward selection and backward elimination (bidirectional elimination) for the selection of model inputs (see Draper and Smith, 1998). The calculations were made using the Matlab 8.4 Statistics and Machine

Learning Toolbox in the following way. At each step the p-values of an F-statistic of models with or without each input were evaluated by comparing them with an enter condition p_{enter} = 0.05 and an exit condition p_{remove} = 0.1. If inputs currently not in the model had p-values below p_{enter}, the one with the lowest value was included into the model until the next step (forward selection). If inputs currently in the model had p-values above p_{remove}, the one with the highest value was removed from the model (backward elimination). These steps were repeated until the model could not be further improved by a single step. The initial model contained no inputs.

4.4.3 Marginal distribution sampling

Reichstein et al. (2005) presented the MDS method for gap-filling of net ecosystem exchange. I propose a redesign of the algorithm for the use with methane fluxes. The original algorithm takes into account the covariation of gas fluxes and environmental drivers (look-up table steps) as well as the temporal autocorrelation of gas fluxes (diurnal cycle steps). A look-up table step involves searching for similar meteorological conditions within different time windows. Gas fluxes from the found timestamps are averaged to fill the respective gap. Look-up table steps are performed with two sets of variables, either only with global radiation (R_g) or with R_g, water vapour pressure deficit (VPD) and air temperature (T_{air}). Similar conditions are defined by limits within which the inputs are allowed to vary. I replaced the original input variables used for CO_2 gap-filling with meteorological variables of the general categories level 1 and level 2. A level 1 variable is required in all look-up table steps (steps 1, 2, 3, 6 & 7; see figure 4.2) of the original algorithm; it replaces R_g. The number of level 2 variables is unlimited in my approach. They appear in steps 1, 2 and 6 and replace VPD and T_{air}. Thereby the model is set up to take various inputs that can be rated by importance. The selection of model inputs is described later in this text. Furthermore, I added a criterion for the minimal number of averaging samples n_{min}.

To get an estimate of the goodness of fit, I ran a slightly modified version (MDS_{QC}) of the algorithm described above. Instead of cycling through the gaps of the time series, this routine scrolls through the data points and calculates an estimate without using the respective data point itself but all other available data. This way, an individual MSE for all three quality classes and an overall MSE can be calculated.

To run the look-up table steps within the MDS model, it is necessary to determine limits that define similar conditions for each input. To yield these limits I proceeded as follows. First, the dispersion of each input was described by calculating its range (maximum minus minimum value) which was then divided by two. Then, 1000 random numbers, laying between zero and the variables' half-range, were generated. The MDS_{QC} routine was run 1000 times with these random limits (Lim_{rand}); n_{min} was set to 5. Subsequently, the Lim_{rand} of the 100 runs

with the lowest MSE were binned in five classes. The bin center of the class with the most counts was termed initial limit (Lim_{init}). A second set of 1000 random limits was generated the same way, and MDS_{QC} was run 1000 times for each input with the limits of all remaining inputs kept constant at Lim_{init} and one being drawn without replacement from the second list of random limits. For each input the 100 Lim_{rand} with the lowest MSE were again binned in five classes, and the bin center with the most counts was used as final limit (Lim_{gf}) for gap-filling.

In case of CO_2 gap-filling, the three input variables and limits proposed by Reichstein et al. (2005) were used. The n_{min} condition was, however, left part of the MDS routine, what constitutes the difference between it and the original approach of Reichstein et al. (2005).

4.4.4 Multilayer perceptron

The MLP was set up with one hidden layer with tan-sigmoid activation functions, a single output layer node with a linear transfer function and Levenberg-Marquardt backpropagation as supervised learning method. See Papale and Valentini (2003), Dengel et al. (2013), Sarle (1994) for details on MLP architecture. The input data was divided randomly in 70 % training and 30 % validation data. Inputs were re-scaled before training to range between -1 and 1. Training data was used to optimize the network weights and biases for low MSE. Validation data served as inputs independent from training data to check the generalization capability of the model. The model performance on these data was used to avoid overfitting by terminating the learning process if for six consecutive iterations the MSE of the validation data did not decrease (early stopping).

Instead of using the response of a single MLP, I calculated the ensemble average of multiple networks starting with varying initial weights and different sets of training and validation data each. This method is well described in neural network literature (Hashem, 1997; Haykin, 1999; Naftaly et al., 1997; Perrone and Cooper, 1993; Wolpert, 1992) as one type of so called committee machines. It has been shown that dividing the input space into many subspaces and consecutively combining all individual so called expert responses to an overall prediction is often superior to the response of a single network.

To find an approriate number of hidden layer nodes (#HLN), I used Akaike's information criterion (AIC). I simulated committee machines with 100 networks each for hidden layer sizes from 1 to 20. The resulting relationship between #HLN and AIC was inspected further in an effort to find the optimal #HLN. In general, the relevance of a model rises with decreasing AIC. The #HLN optimum thus should be found at the AIC minimum. However, for different gases and datasets, I encountered two shapes a relation like this would commonly assume. The more desirable for analysis is a parabola-like curve with a clear minimum at the function vertex. The second type is an asymptotic function of the form $AIC = \#HLN^{-1} + a$. In order to programmatically decide within the I-SIM algorithm on which #HLN to use for

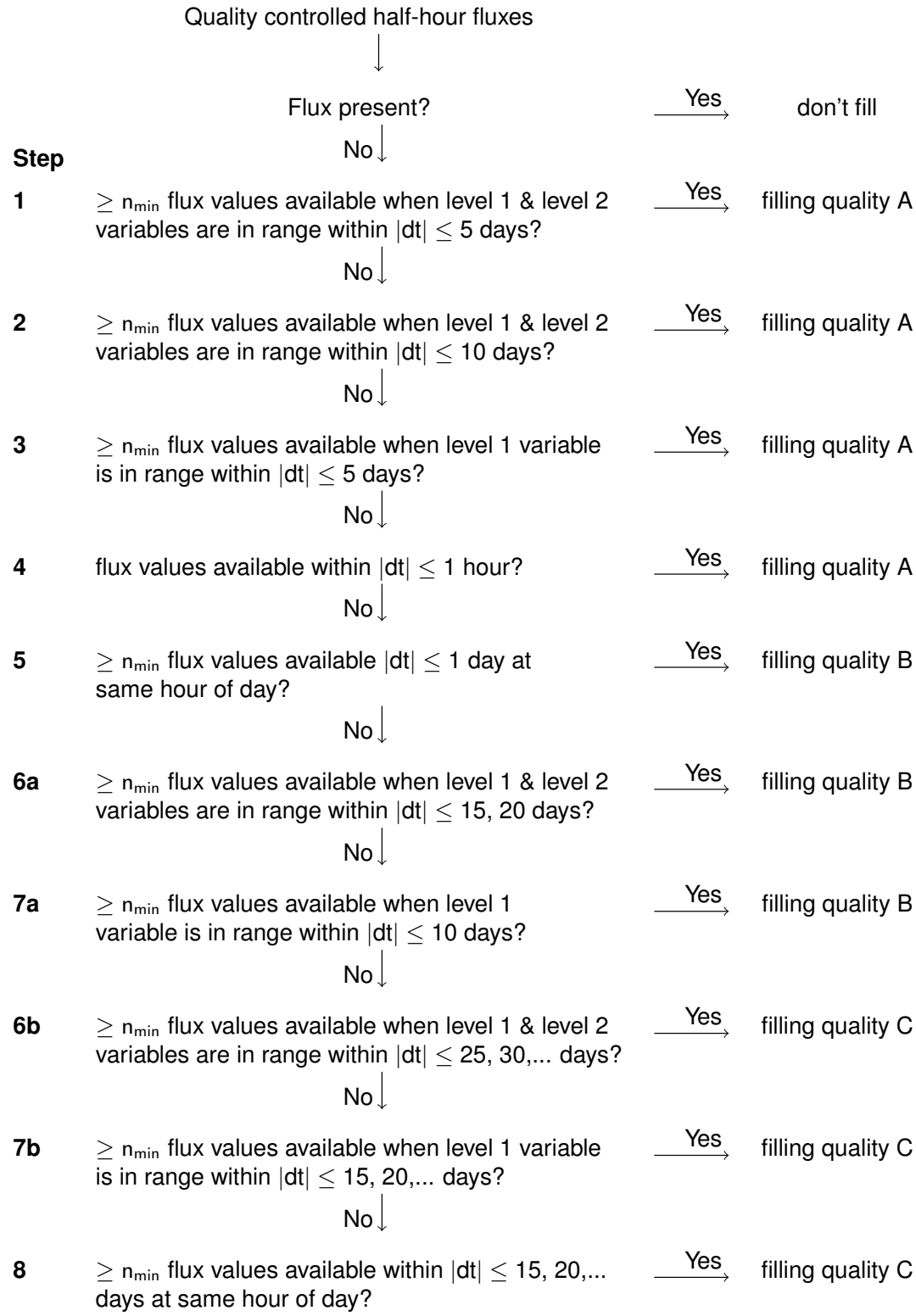

Figure 4.2: Flow diagram of the marginal distribution sampling algorithm as implemented in I-SIM, changed after Reichstein et al. (2005). n_{min}: minimum number of averaging samples.

the final MLP architecture, the program flow illustrated in figure 4.5 was implemented. First, #HLN1 is found at the AIC minimum. Next, an asymptotic function is fitted to the data and differentiated. The derivative is rounded to the nearest multiple of 10 if F_{CH4} is the model target or of 100 in case of F_{CO2} modeling. #HLN2 is defined to be at the position where the rounded derivative turns zero for the first time. The decision tree is finished at this point, and #HLN1 is used as best hidden layer size if it is smaller than #HLN2. Due to observed cases of parabolic curve shapes where #HLN2 was found left from the vertex, a further check is included before #HLN2 is to be selected as optimum. This revisal includes the fit of a 2nd degree polynomial whose 1st derivative is set to zero to find #HLN3 at the function vertex. If #HLN1 lies within [#HLN3 -1, #HLN3 +1] and is smaller than the maximum number of nodes of 20 it is used as hidden layer size optimum. Otherwise, the result of the asymptotic fit #HLN2 gets selected. The resultant number of nodes is used to construct 1000 networks whose mean response yield the I-SIM MLP model.

4.4.5 Radial basis function neural network

Another kind of feedforward neural network, namely a RBF network, was applied and tested with our data. In contrast to MLPs, RBF networks use Gaussian exponential functions (see figure 4.3) as activation functions and are non-iterative, i.e. learning is finished after data was passed through the network once. Also,

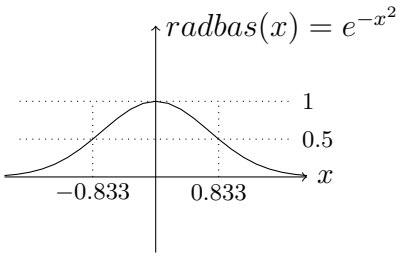

(a)

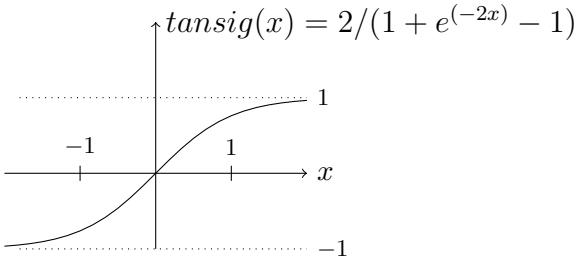

(b)

Figure 4.3: Neuron activation functions of a radial basis function neural network (a) and a multilayer perceptron (b).

rather than passing a linear combination of input and weight to the activation function, the euclidean distance of the input and weight vector is calculated, multiplied with a bias and then passed to the radial basis function. The outputs of the radial neuron are then assigned as inputs to the second layer consisting of linear neurons with associated upstream weights and biases. The values optimized during learning are the linear output layer weights and biases that are adjusted for minimal MSE. In our case, model inputs were normalized by subtracting the average of the respective input series from each of its values and dividing the results by the corresponding standard deviations (as in Schmidt et al. (2008)). See for example Haykin (1999), Schmidt et al. (2008), Sarle (1994) or Beale et al. (2015) for more details on RBF architecture.

The hidden layer weights can also be

thought of as the centers (i.e. maxima) of the RBF. These centers are constructed from the training samples; several different approaches on how to determine these hidden layer weights are described in literature. They can for example be found statistically by the so called k-means clustering algorithm using all available input vectors (Bishop, 1995; Haykin, 1999; Likas et al., 2003; Schmidt et al., 2008). Being an unsupervised learning process (i.e. independent from targets) this method cannot use an optimization of the performance function to find the best centers. I instead applied a parameterized version of a forward selection algorithm proposed by Chen et al. (1991) that uses a subset of input-target pairs to determine the radial node centers. In this stepwise approach, the RBF network starts with zero hidden layer nodes. At each step the input vector with the worst performance is used to add one radial node by setting its weights to be equal to this input vector. To avoid overparameterization and decrease computing time, I stopped training when a fixed number of nodes was reached (as in Menzer et al., 2015).

The first layer biases b are indirectly adjusted by setting the spread parameter $s = 0.833/b$ to a fixed value prior to learning. By this parameter, the receptive field (Sarle, 1994), i.e. the responsiveness of each RBF neuron to input vectors other than the one the neuron weight was constructed from, is determined. Large values of s result in many inputs triggering the activation function, small values make the respective neuron "fire" only for inputs close to the one the neuron weight was constructed from. It is essential to select a value for s that is large enough for the neurons to respond to overlapping regions of the input space as well as small enough, so the network does not respond alike to all inputs.

I included an optimization procedure for the two RBF parameters s and #HLN into the I-SIM algorithm. I first randomly divided the dataset into 60 % training and 40 % validation data. From the training inputs and targets, I constructed 19 RBF networks with spread values between 0.2 and 2 in 0.1 steps and simulated the resulting networks with the validation inputs. The network with the spread value that resulted in the lowest MSE with respect to the validation targets was assumed to be the most accurate and was simulated over the entire input space. I repeated this process 100 times with different data divisions each time and used the ensemble average of these iterations as the overall model response. To find the appropriate #HLN, I calculated committee machine outputs for 1 to 70 hidden layer units and selected the #HLN with the lowest AIC.

4.4.6 Generalized regression neural network

As a third ANN type, I applied GRNNs which have architectural similarities with RBF networks. The hidden layer in a GRNN is set up as a radial basis layer like in a RBF network. The second layer is somewhat different as it contains only weights and no biases. Before passing layer one outputs to the layer two linear activation function, the dot prod-

uct between layer two weights and layer one outputs is calculated and normalized by the number of input vector elements (Beale et al., 2015; Specht, 1991). The network is set up with as many neurons as there are input-target pairs. The first layer weights are set to be equal to the transposed input matrix. The second layer weights are set to be equal to the target vector. That way, for each input vector there is one hidden neuron with a net output of unity that has zero error on the respective target if it were the only neuron in the network. The responsiveness of the neuron to input vectors other than the one it was constructed from is tuned with the spread parameter s, just like in a RBF network. I used the same data division, spread optimization and ensemble average process as with the RBF networks.

4.4.7 Model input selection

According to the principle of parsimony, the dimensionality of the model input space and thereby the model complexity should be reduced as much as possible in order to obtain a relevant model. In an effort to approximate such a model, I developed a general selection procedure that aims for the identification of redundant as well as irrelevant input variables. In literature, the terms *sensitivity* or *importance* are used alike for mathematically different approaches that can give contradicting results. Regarding the analysis of ANNs there is no single indisputable measure of importance, which is on the one hand due to limitations of the existing methods and more importantly due to the fact that different methods address different types of importance. Sarle (1997) gives a critical review on this topic and divides the available methods into such that yield measures for what he terms predictive and causal importance. In short, predictive importance measures are those that check the change of model performance when an input is omitted, whereas causal importance measures evaluate the change of a performance function when inputs are manipulated. The latter can be realized by degrading the variability of an input for example by replacing it partly with its mean (as in Hunter et al., 2000; Schmidt et al., 2008).

In case of the Himmelmoor dataset, three categories of potential model inputs were presented to the selection scheme. Meteorological and soil (biomet) variables, fuzzy variables representing diurnal and seasonal cycles (following Papale and Valentini, 2003) and footprint variables in the form of surface class contribution estimates. Table 4.1 gives an overview of the available variables. Note that in Year 1 no soil properties were recorded. The matrix of potential inputs for Rio Pipo gas flux models did not contain footprint variables. As a first step, possible functional relationships between the inputs were roughly checked by inspecting scatter plots of all variable combinations. To check for time lags between biomet inputs and methane fluxes, their cross-correlation was calculated and normalized to range between -1 and 1 (Kettunen et al., 1996). The lag time for which the absolute cross-correlation was maximized was used to shift the respective

Table 4.1: Available (x: yes, -: no) model inputs sorted by type and time lags between Himmelmoor CH_4 flux and biomet variables derived from cross-correlation.

Type	*Name*	*Unit*	*Abbreviation*	*available in...*		*Time lag, hours*	
				Year 1?	*Year 2?*	*Year 1*	*Year 2*
Biomet	Global radiation	W m^{-2}	R_g	x	x	0	2
	Air temperature	°C	T_{air}	x	x	1.5	2.5
	Outgoing longwave radiation	W m^{-2}	Lw_{out}	x	x	2	2
	Air pressure	kPa	P_{air}	x	x	-6	4.5
	Rate of change in air pressure	kPa/1800 s	$slope_{Pair}$	x	x	5.5	6
	Water vapour pressure deficit	Pa	VPD	x	x	1	1.5
	Soil redox potential in 2 cm depth	mV	$Redox_2$	-	x	n.a.	-5
	Soil redox potential in 5 cm depth	mV	$Redox_5$	-	x	n.a.	1
	Soil redox potential in 10 cm depth	mV	$Redox_{10}$	-	x	n.a.	1
	Soil redox potential in 20 cm depth	mV	$Redox_{20}$	-	x	n.a.	2
	Soil temperature in 2 cm depth	°C	T_{Soil2}	-	x	n.a.	4.5
	Soil temperature in 5 cm depth	°C	T_{Soil5}	-	x	n.a.	-4.5
	Soil temperature in 10 cm depth	°C	T_{Soil10}	-	x	n.a.	-1.5
	Soil temperature in 20 cm depth	°C	T_{Soil20}	-	x	n.a.	2.5
	Soil temperature in 40 cm depth	°C	T_{Soil40}	-	x	n.a.	-6.5
	Water table below surface	cm	WT	-	x	n.a.	7.5
Fuzzy	Morning	n.a.	$fuzzy_{mo}$	x	x		
	Afternoon	n.a.	$fuzzy_{af}$	x	x		
	Evening	n.a.	$fuzzy_{ev}$	x	x		
	Night	n.a.	$fuzzy_{ni}$	x	x		
	Summer	n.a.	$fuzzy_{su}$	x	x		
	Winter	n.a.	$fuzzy_{wi}$	x	x		
Footprint	Class contribution of rewetted area	n.a.	CC_{rew}	x	x		
	Class contribution of drained area	n.a.	CC_{dra}	x	x		
	Class contribution of vegetated area in rewetted part	n.a.	$CC_{veg,\ W}$	x	x		
	Class contribution of vegetated area in drained part	n.a.	$CC_{veg,\ E}$	x	x		

variable. Thus a second biomet data set with lagged variables was derived. The obtained time lags are also presented in Table 4.1. Three datasets were used for sensitivity analysis: Only the original biomet data, only the lagged data and both. All data sets were extended by fuzzy and footprint data.

Four methods to estimate the importance of the individual inputs were applied. They were combined via a scoring table (see figure 4.4). If an input was selected by one method, one point was assigned to it. Inputs with more points were regarded as more important. For the scoring table I used predictive as well as causal importance measures and yet another indicator for input sensitivity termed relative importance.

As applied previously by Dengel et al. (2013), I used the outcome of a MLR with bidirectional elimination which can be regarded as a measure of predictive importance. Inputs that remained in the model received one point. To calculate causal importance measures, I used the output of a MLP whose hidden layer size had been optimized first for all three input data sets. I chose the output of MLPs because they, as opposed to RBF networks, have the ability to ignore irrelevant inputs without developing the need for increased complexity in order to do so. This property can be attributed to the fact that inputs are linearly combined in the first MLP layer, what includes the option for the network to select a linear subspace of inputs. Redundant inputs, however, can be processed by both MLPs and RBF networks effectively. Following Schmidt et al. (2008), I calculated two similar measures of causal importance from the MLP output. The variability of each input variable was manipulated by replacing first 50 % and then 100 % with its median, while all remaining variables were left unchanged. A network was first trained with the original data and then simulated with the artificial input matrix. The relation of the resultant mean squared errors (MSEs) was calculated and called relative error (RE). This process was repeated 1000 times for all input variables to obtain diverse results for different data divisions. The resulting values for RE were binned into six classes with centers at 0.8, 0.9, 1.0, 1.1, 1.2 and 1.3. If the latter was the bin with the most counts, one point was assigned to this input variable in the scoring table, meaning that the manipulation of this input vector resulted in a deterioration of the respective MSE of more than 25 % in most cases. This method yielded two measures of causal importance for each input variable, RE_{50} and RE_{100}, referring to the two percentages of data being manipulated.

Next,the weights of a MLP were interpreted based on the algorithm of Garson (1991) as presented in Olden and Jackson (2002). This method interprets the weights of a neural network similar to the coefficients of a linear model. Before calculating the relative importance (RI) of an input, the products of the weights that connect this input with each hidden neuron and the output layer is determined and normalized by the sum of weight products feeding also into the same hidden unit. These so called neuron contributions are summed up and normalized by the sum of all neuron contributions re-

sulting in the RIs of all inputs. I analyzed the RIs of 1000 MLP runs by computing their mean, median and maximum values for all input variables. I then compiled three lists, where I sorted the inputs in descending order with respect to the determined statistics. The lengths of those lists were afterwards shortened to equal the number of variables that were included in the MLR model that was derived before – only variables with the highest RI statistics stayed in the lists. All inputs that occurred at least in two of three lists received one point in the scoring table, which was completed with this step.

I then summed up the scores for all input variables and calculated two score thresholds above which an input was to be selected. One threshold was derived for the original and the lagged biomet variables, one for fuzzy and footprint data. I proceeded like this owing to the structure of the three input datasets. Each biomet variable occurred in two of three datasets, each fuzzy and footprint variable was part of all datasets, making it more likely for them to reach a high score. I calculated the mean score of the respective variable category and used the next larger integer as a score threshold.

The inputs that were selected via the scoring table were used to fit another MLR model. By that, the inputs were rated with a final causal importance measure. The last step of the input selection algorithm was to check if both a variable and its lagged derivative remained in the input matrix. If so, the scores of those two variables were compared, and only the higher scoring input stayed in the matrix. In case there was no score difference, the lagged derivative was removed from the input space, whose reduction was hereby finished. The obtained variables were regarded as most relevant and least redundant and used as inputs for all models. As the MDS approach is designed to accept inputs of different importance, the input matrix for this model had to be divided into level 1 and level 2 variables. The matrix division was done based on the result of the final MLR in the selection process described above. The variable which was selected in the first iteration of this stepwise approach was used as level 1 input, all others as level 2 inputs.

In case of the Rio Pipo dataset, gaps in the input variable time series were closed with a mean diurnal variation (MDV) approach prior to gas flux modeling. If this algorithm encounters a gap, it looks for available values of the same variable in adjacent days at the same hour of day and uses the mean of the found records to fill the gap. At first, a window of $\pm$ 1 day around the gap is screened. If not at least one data point is found, the search range is increased in steps of one day to up to five days until the gap can be filled.

4.4.8 Measures for model comparison

To compare the performance of the different model types, I used Akaike's information criterion

$$AIC = n \cdot ln(MSE) + 2 \cdot P_{free}$$

or if $n/P_{free} < 40$

$$AIC_c = AIC + \frac{2P_{free}(P_{free}+1)}{n - P_{free} - 1} \quad ,$$

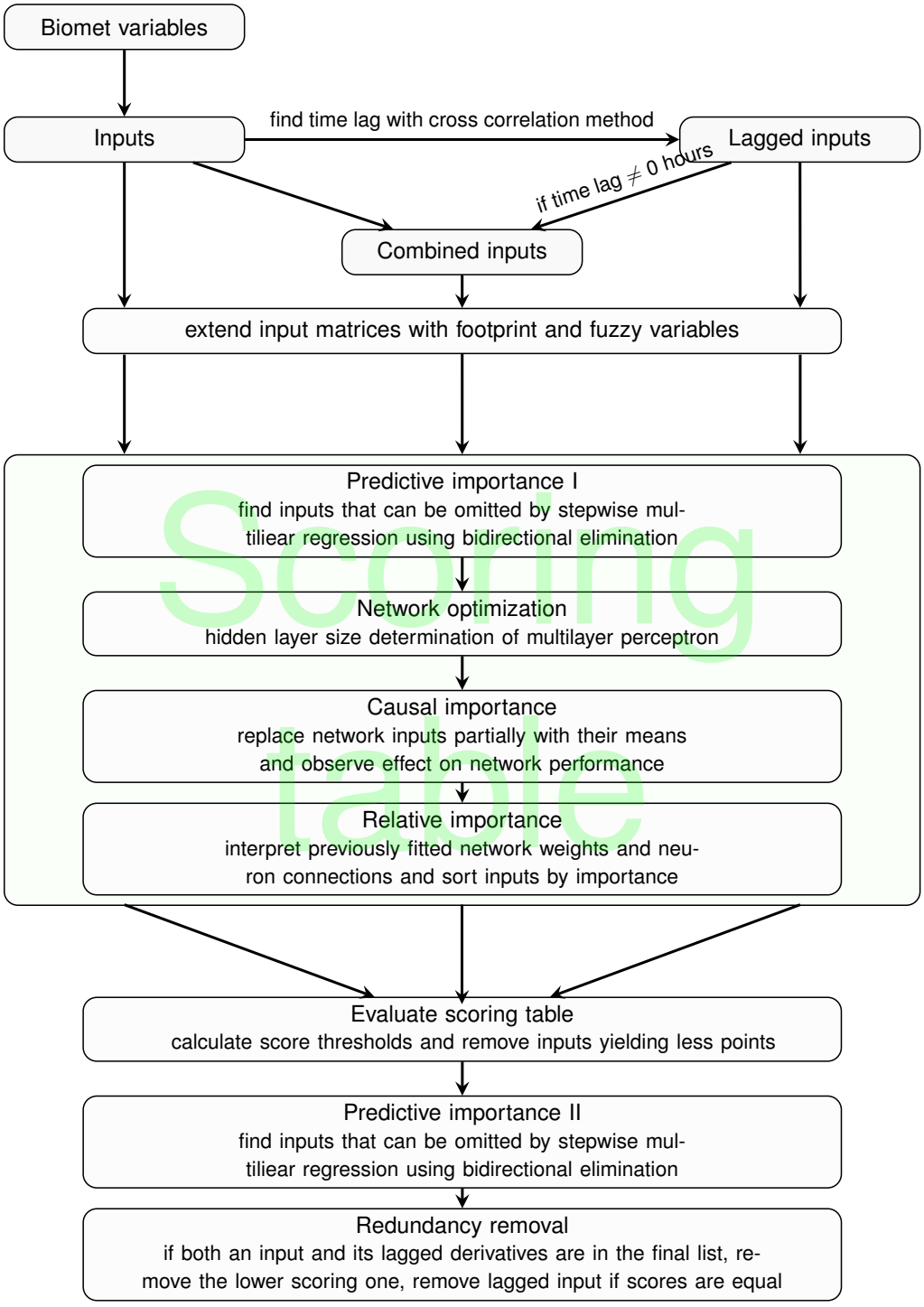

Figure 4.4: Flow chart of input selection module within the input-sensitive input and model selection (I-SIM) algorithm.

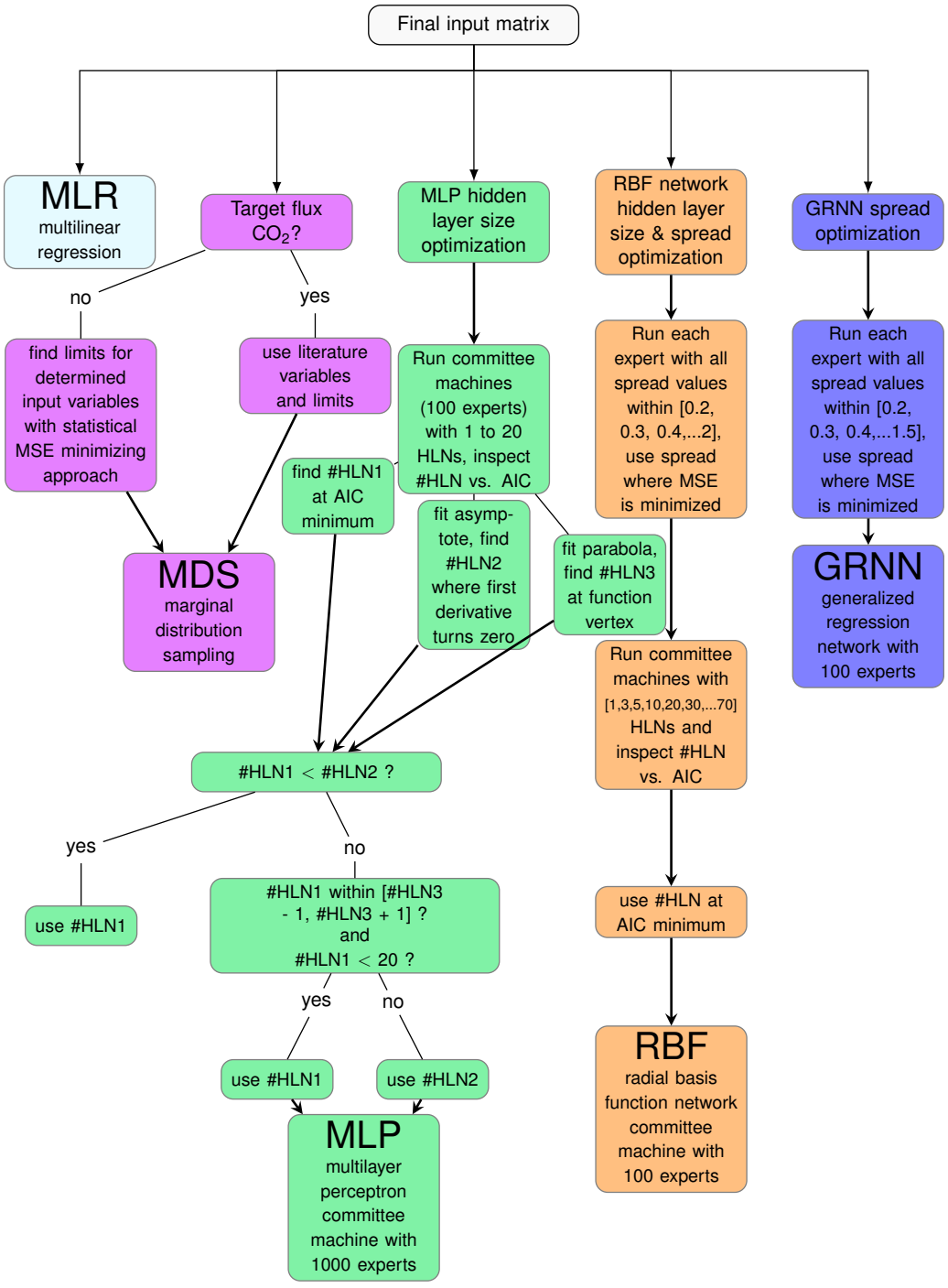

Figure 4.5: Flow chart of the model calibration module within the input-sensitive input and model selection (I-SIM) algorithm. MLR: multilinear regression, MDS: marginal distribution sampling, MLP: multilayer perceptron, RBF: radial basis function, GRNN: generalized regression neural network.

Pearson's correlation coefficient

$$r = \frac{\sum_{i=1}^{n}(m_i - \overline{m})(t_i - \overline{t})}{\sqrt{\sum_{i=1}^{n}(m_i - \overline{m})^2 \sum_{i=1}^{n}(t_i - \overline{t})^2}} \quad ,$$

root mean squared error

$$RMSE = \sqrt{\frac{\sum_{i=1}^{n}(m_i - t_i)^2}{n}} \quad ,$$

bias error

$$BE = \frac{1}{n}\sum_{i=1}^{n}(m_i - t_i)$$

and mean absolute error

$$MAE = \frac{1}{n}\sum_{i=1}^{n}|m_i - t_i|$$

where n is the number of measured target values, P_{free} is the number of model parameters, m_i are modeled values, t_i are target fluxes and $\overline{t}$ and $\overline{m}$ are their means. To characterize the spectral properties of the models, I transformed the respective time series into the frequency domain using the method of Lomb (1976) and Scargle (1982) creating a so called Lomb-Scargle periodogram. This method allows for the estimation of a power spectrum (P) similar to the Fourier spectrum, but it can in contrast be applied to unequally spaced time series, hence flux datasets with gaps. With the power spectrum of the time series, I could calculate the scaling exponent α, which is a measure of the noise or the autocorrelation respectively contained in time series data. The scaling exponent is given by $P(f) = f^{\alpha}$ (where f is frequency) and was calculated as the slope of the log-log transformed relationship between f and P (Richardson et al., 2008). Values of α around -2 point to high autocorrelation (red noise), values close to 0 characterize equal spectral power across all frequencies (white noise), whereas values around -1 denote an intermediate correlation structure in the data (pink noise).

4.5 Mechanistic gap-filling

The I-SIM methodology described in section 4.4 was also applied to fill gaps in the CO_2 time series of the Rio Pipo site. In addition to the five models included in I-SIM, a sixth deterministic model was tested in case of the Rio Pipo data set. The Ecosystem photosynthesis respiration model (EPReM) is a flux partitioning and gap-filling tool developed by Christian Wille (v 2.2, 03/2016, unpublished) based on work by Runkle et al. (2013). The measured eddy covariance CO_2 flux (NEE), is described as the following function of temperature and radiation.

$$NEE = R_{base} \cdot Q_{10}^{(T-15)/10} - \frac{P_{max} \cdot \alpha \cdot PAR}{P_{max} + \alpha \cdot PAR}$$

The model includes the four parameters temperature sensitivity coefficient Q_{10}, maximum photosynthetic rate P_{max}, base respiration R_{base} and initial quantum yield efficiency α. Model complexity is, however, reduced during this three step algorithm. In step 1 the four parameter model is fitted to data available in a five day time window. The window is moved in steps of one day. For every step, one set of parameters is derived. A model is only fitted

if in a single step (1) the number of available data points is larger or equal to the chosen window size in days times nine, (2) the mean temperature exceeds -10 ° C and (3) the temperature range (T_{max} - T_{min}) is larger than 12 K. From the resultant daily parameter sets the ones where none of the parameters' 95 % confidence intervals exceeds their respective values are selected. Of these fits the median Q_{10} value is determined. If this median falls within [1.1, 1.7], Q_{10} is set to this value for steps two and three; if not, a fixed value of 1.4 (following Mahecha et al., 2010) is used for the subsequent steps. With Q_{10} being fixed at this stage, three parameter models are fitted in step 2 in a similar fashion like before. Only now, the temperature range condition is not a prerequisite for carrying out a regression any more. All significant α values from the resultant fits are used to find a relation between α and day of year (DoY). Step 2 is concluded by finding the parameters of the Gaussian function

$$\alpha(DoY) = k \cdot exp(-1 \cdot \mid \frac{(DoY - l)^m}{2n^2} \mid) + o$$

which is set up to reflect the seasonality embedded in α. In step 3, Q_{10} is still held constant and a model with 3 parameters is fitted. However, in this iteration, the window size is varied until significant parameters are found. The algorithm tries to fit models starting from a range of one up to 30 days in steps of one day. In case the window is at maximum length and no parameters could be found or α is larger than $2 \cdot \alpha(DoY)$, α is set to $\alpha(DoY)$ utilizing the function from step 2. The EPReM is then a two-parameter model.

4.6 Dataset division by microform type

The I-SIM methodology was first applied to the carbon gas fluxes that were directly measured with the EC system. The resulting gap-filled time series thus represent approximations of the landscape scale fluxes integrated over the whole ecosystem. These time series are from hereon called tower view time series (TVTS). In case of the Himmelmoor dataset, SCTS were constructed by selecting all flux values for the class contributions CC_{dra} and CC_{rew} above a threshold which was set to 70 %. The obtained four time series ($Y1_{rew}$, $Y1_{dra}$, $Y2_{rew}$ and $Y2_{dra}$) were again gap-filled using I-SIM. Apart from the class contribution variables, the inputs presented to the selection scheme were the same as for TVTS modeling. To gap fill the SCTS, the contributions of the respectively opposite surface classes were omitted from the input space. To fill $Y1_{rew}$ for instance, CC_{dra} and class contribution of surface class *vegetated* within CC_{dra} ($CC_{veg,E}$) were removed from the input matrix. Also, the surface class of interest was set to the threshold value of 70 % at all flux gaps that resulted from data division. The measured contributions of SC_{veg} were binned in ten classes and the bin-center of the most frequent class was used to fill gaps in the CC_{veg} time series. Referring to the example above, CC_{rew} would be set to 70 % in $Y1_{rew}$ gaps; class contribution of surface class *vegetated* within CC_{rew} ($CC_{veg,W}$) statistics would be evaluated for all timestamps where $Y1_{rew}$ has a record and the bin-center of the most fre-

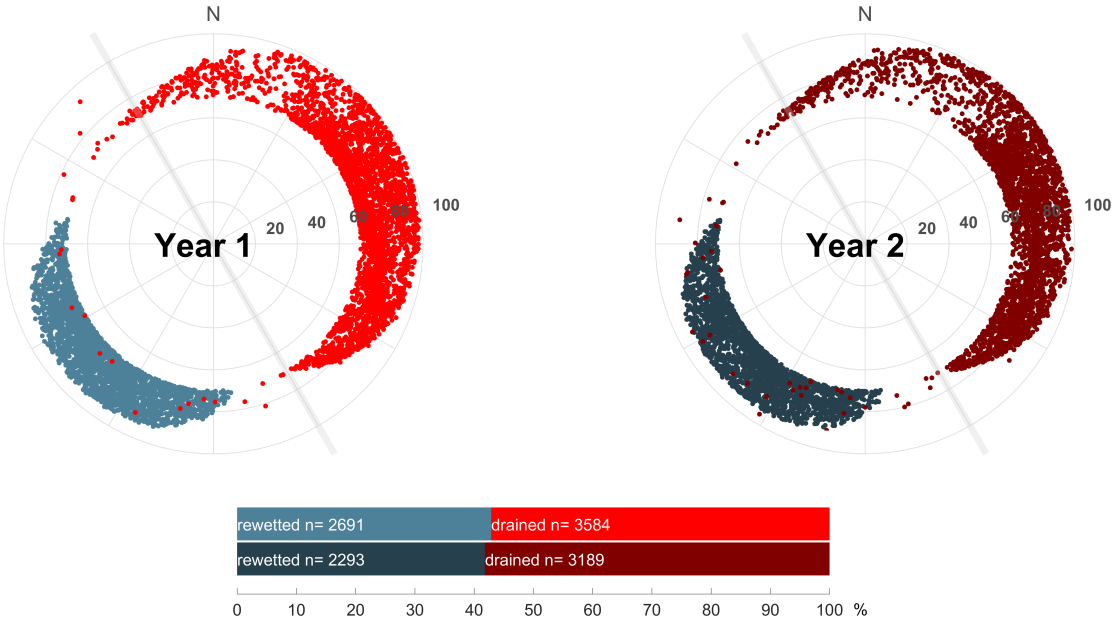

Figure 4.6: Half-hourly contributions above 70 % of the *rewetted* and *drained* surface class in Himmelmoor to the EC footprint, plotted against mean wind direction. In both analyzed years, half hours mostly associated to only one surface class, are a bit more frequent from the *drained* site. The gray line indicates the direction of the central railroad dam. From this perspective, the EC tower is located at the origin of the plot.

quent class would be put into $CC_{veg,W}$ where $Y1_{rew}$ has a flux gap.

4.7 Mechanistic interpretation of model results on surface class level

In case of the Himmelmoor F_{CO2} SCTS, the following deterministic model was fitted to monthly ensembles of the half-hourly time series,

$$\begin{aligned} NEE(CC_{veg}, PAR) = \\ (1 - CC_{veg}) \cdot R_{eco,bare} \\ + CC_{veg} \cdot R_{eco,veg} \\ - CC_{veg} \cdot \frac{P_{max} \cdot \alpha \cdot PAR}{P_{max} + \alpha \cdot PAR} \end{aligned}$$

where CC_{veg} is the class contribution of the vegetated strips, PAR is photosynthetically active radiation, $R_{eco,\,veg}$ and $R_{eco,\,bare}$ are ecosystem respirations of the vegetated strips and the areas covered by bare peat respectively, P_{max} is the maximum photosynthetic rate and α is the initial quantum yield. Prior to fitting, CC_{veg} was rescaled to sum up to 1 with CC_{bare} so that

$$1 - CC_{veg} = CC_{bare}.$$

The last term of the fitted model consists of a rectangular hyperbolic Michaelis-Menten type function to simulate plant photosynthesis as first proposed by Thornley (1998) and revisited by e.g. Zheng et al. (2012). This type of light saturation curve has found widespred application throughout literature and has proven to be feasible for modeling plant carbon dioxide fixation driven by radiation. As only some parts of Himmelmoor are occupied by vegetation, I scaled

this term with the half-hourly contribution of those surfaces (CC_{veg}) to the EC footprint. In order for the model to express net CO_2 flux, two ecosystem respiration terms were added to the formula; the combined plant and soil respiration $R_{eco,\,veg}$ scaled by CC_{veg} and the microbial respiration $R_{eco,\,bare}$ taking place in the vegetation-free areas scaled with CC_{bare}. This function was fitted to every month of all four available ($Y1_{dra}$, $Y1_{rew}$, $Y2_{dra}$ and $Y2_{rew}$) CO_2 SCTS, yielding timeseries of the four model parameters each. The included scaling of the model terms with the surface class contributions facilitates comparability of the parameter timeseries among each other and with literature values describing the light response of similar plant communities as found in the vegetated strips of Himmelmoor.

4.8 Calculation of cumulative fluxes

In order to obtain annual sums of carbon gas fluxes for the different surface classes and years, measured fluxes of quality class MF1 were included back into the SCTS. All MF1 values that corresponded to CC_{dra} or CC_{rew} ranging above 70 % were used to replace the modeled SCTS data for the respective timestamps. The gaps remaining after this step were closed using the MLP model results. Time steps when the MLP model had gaps due to missing input variables (mostly an issue in Year 2) were filled with MDS results since this is the only gap-filling method used that still produces an output when input biomet records are missing. It does so in the diurnal cycle steps of the algorithm (see steps 4, 5 and 8 in figure 4.2 and section 4.4.3).

Which error got assigned to the half-hourly fluxes of the SCTS depended on whether it was a measured, a MLP or a MDS value. For measured fluxes, 20 % of it were included into the uncertainty term to account for systematic errors of the EC method. Random uncertainty was added to the term following Finkelstein and Sims (2001). In case of MLP data, the uncertainty estimate was based on the performances of the 1000 individual networks prior to ensemble averaging (see 4.5). The optimization of each expert machine comprised validation runs with 30 % of the available data that were independent from network training (see 4.4.4). The residuals of these validation runs hence give a conservative estimate for the individual model's generalization capability. The highest root mean squared error (RMSE) of all validation runs was used as an uncertainty estimate for each MLP data point. Values in the SCTS taken from the MDS model received uncertainties according to their quality class. RMSEs were computed for data of quality A, B and C with the MDS_{QC} routine (see 4.4.3). Uncertainties of cumulative flux sums were calculated applying the rules of Gaussian error propagation.

Chapter 5

Results

5.1 Linear flux-input dependencies

Himmelmoor. To gain first insight into the relations between input variables and gas fluxes as well as between the input variables among each other, scatter plots were inspected and Pearson's correlation coefficient (r) was determined for each pair (see appendix, figures A.1 to A.6). Three biomet timeseries correlate with r values of 0.4 or higher with F_{CH4} in both years: Lw_{out}, T_{air} and R_g. In Year 1, this list is extended by VPD and PAR while the highest linear relation exists with CC_{rew} (0.5) and $CC_{veg,W}$ (0.6). In Year 2 additional connections with r values of 0.4 or higher include soil temperatures T_{Soil20}, T_{Soil2} and T_{Soil40}. Footprint variables were not as closely related as in Year 1. Nevertheless, $CC_{veg,W}$, yields again the highest correlation among the footprint variables.

Linear relations between model inputs variables and F_{CO2} are more clear as the only strong connections exist with PAR and R_g (both r = 0.5 in Year 1 and r = 0.6 in Year 2).

Regarding linear dependencies between biomet variables, R_g and photosynthetically active radiation (PAR) ($r > 0.9$ both years), T_{air} and VPD (r = 0.7 in both years) as well as T_{air} and outgoing longwave radiation (Lw_{out}) ($r > 0.9$ both years) were highly correlated. In Year 2, soil temperatures were closely connected among each other ($r > 0.9$) and with T_{air} ($r > 0.7$). Water table depth (WT) was correlated negatively with all redox measurements at different positions in the soil profile, with the largest absolute r of -0.7 for the relation with $Redox_{20}$. WT was also correlated with T_{Soil20} (r = 0.3). The seasonality embedded in soil temperature measurements was reflected by high correlation coefficients with the two low frequency fuzzy variables fuzzy variable *summer* ($fuzzy_{su}$) and fuzzy variable *winter* ($fuzzy_{wi}$) (see A.6). The deeper in the soil profile the temperature measurement was taken, the less amplitude response they show to diurnal variations and the less noisy the relation to the fuzzy data appears to be.

Rio Pipo. The biomet and fuzzy variables that were fed into the I-SIM algorithm are shown in table 5.1. Linear correlations between F_{CO2} and the potential model inputs were inspected. Closest dependencies exist between F_{CO2} and the radiation variables R_g (r = -0.8),

PAR (r = -0.8) and outgoing shortwave radiation (Sw_{out}) (r = -0.6). Connections also appear with the fuzzy variables fuzzy variable *afternoon* ($fuzzy_{af}$) (r = -0.6) and fuzzy variable *night* ($fuzzy_{ni}$) (r = 0.5) that contain diurnal information as well. Linear temperature dependencies of F_{CO2} were not particularly strong with the highest absolut r of -0.4 with $T_{SoilH,-2}$. All of the mentioned radiation variables are highly correlated among each other. The seasonal trend in volumetric water content measurements of the wet lawn microforms is depicted by their correlations with $fuzzy_{su}$ and $fuzzy_{wi}$, which are positive ($r > 0.4$) with the latter and negative ($r <$ -0.5) with $fuzzy_{su}$. With ground heat flux measurements the relation is also strong but with reverse signs.

Table 5.1: Available Rio Pipo model inputs sorted by type. Time lags between carbon dioxide flux and biomet variables derived from cross-correlation.

Type	*Name*	*Unit*	*Abbreviation*	*Time lag, hours*
Biomet	Global radiation	W m^{-2}	R_g	0.0
	Outgoing shortwave radiation	W m^{-2}	Sw_{out}	0.0
	Incoming longwave radiation	W m^{-2}	Lw_{in}	2.5
	Outgoing longwave radiation	W m^{-2}	Lw_{out}	2.5
	Air temperature	°C	T_{air}	1.5
	Water vapour pressure deficit	Pa	VPD	1
	Photosynthetically active radiation	mol m^{-2} s^{-1}	PAR	0
	Soil temperature under Empetrum lawn in 1 cm depth	°C	$T_{SoilEL,-1}$	2.5
	Soil temperature under Empetrum lawn in 10 cm depth	°C	$T_{SoilEL,-10}$	-3.0
	Soil temperature under Empetrum lawn in 20 cm depth	°C	$T_{SoilEL,-20}$	3.5
	Soil temperature under Sphagnum lawn in 1 cm depth	°C	$T_{SoilSL,-1}$	3.0
	Soil temperature under Sphagnum lawn in 10 cm depth	°C	$T_{SoilSL,-10}$	-2.5
	Soil temperature under Sphagnum lawn in 20 cm depth	°C	$T_{SoilSL,-20}$	1.5
	Soil temperature under Sphagnum hummock in 2 cm depth	°C	$T_{SoilH,-2}$	3.0
	Soil temperature under Sphagnum hummock in 25 cm depth	°C	$T_{SoilH,-25}$	3.5
	Soil temperature under Sphagnum hummock in 50 cm depth	°C	$T_{SoilH,-50}$	-5.5
	Volumetric water content under Empetrum lawn	m^3/m^3	VWC_{EL}	-6.0
	Volumetric water content under Sphagnum lawn	m^3/m^3	VWC_{SL}	-7.0
	Volumetric water content under Sphagnum hummock	m^3/m^3	VWC_H	-5.0
	Ground heat flux under Empetrum lawn	W m^{-2}	HF_{EL}	1.0
	Ground heat flux under Sphagnum lawn	W m^{-2}	HF_{SL}	0.0
	Ground heat flux under Sphagnum hummock	W m^{-2}	HF_H	4.5
Fuzzy	Morning	n.a.	$fuzzy_{mo}$	n.a
	Afternoon	n.a.	$fuzzy_{af}$	n.a
	Evening	n.a.	$fuzzy_{ev}$	n.a
	Night	n.a.	$fuzzy_{ni}$	n.a
	Summer	n.a.	$fuzzy_{su}$	n.a
	Winter	n.a.	$fuzzy_{wi}$	n.a

5.2 Methane flux gap-filling

Quality filtering. The effects of the quality filters on the distribution of half-hourly Himmelmoor CH_4 fluxes are shown in figure 5.1. Overall, 80 % of the original data were discarded. By far the most records (50 % compared to the preceding step) were filtered out due to failure of the skewness or the kurtosis test. The average as well as the skewness of the data distribution become negative after this step, hence more positive than negative spikes were removed by this filter. The amplitude resolution test captures more negative spikes so that the mean becomes positive again. The footprint filter has no noticeable effect on the distribution. The RSSI filter removes preferably negative fluxes as the mean is more than four times larger and skewness jumps from -20 to about 80 after this step. In contrast, many of the positive spikes are discarded by the Std_{RSSI} filter, leading to a dropping mean and skewness. The distribution becomes

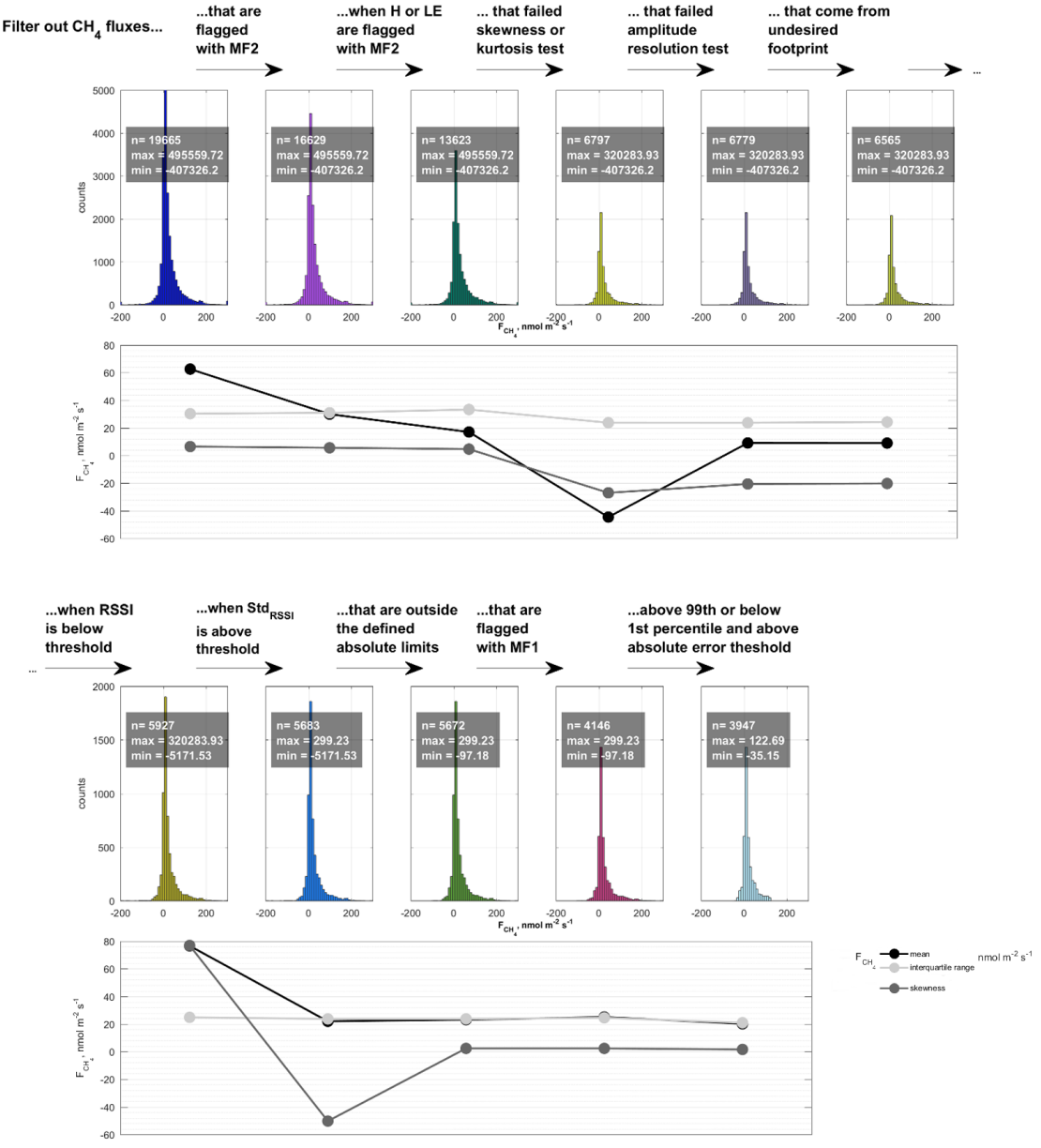

Figure 5.1: The effects of the different quality filtering steps on the distribution of the available two years of half-hourly Himmelmoor methane fluxes. n: number of flux values, min: minimum flux, max: maximum flux, RSSI: signal strength of the LI-7700 gas analyzer, Std_{RSSI}: relative standard deviation of 20 Hz RSSI, MF1/MF2: flux quality classes after Mauder and Foken (2004).

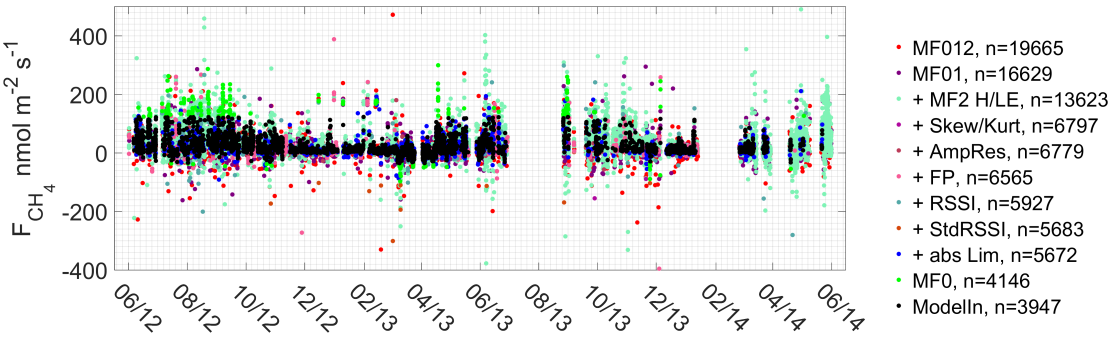

Figure 5.2: Two year Himmelmoor CH_4 target time series for flux modeling compared to lower quality time series from preceding stages of the filtering process.

more symmetrical after the absolute limits filter. Removing data flagged with MF1 eliminates a considerable amount of fluxes (27 % compared to the preceding step), most of them near zero. The range of the distribution is narrowed further by the last step, including the removal of fluxes with high absolute errors and the highest and lowest percent of records being discarded. While all these filters have heavy effects on measures affected by spikes, the data's interquartile range changes muss less vigorously throughout the filtering process. The dispersion of the data is therefore not altered by it.

Input selection. The outcome of the I-SIM method is illustrated in figure 5.3. For Year 1, 14 of the 21 available input variables were selected via the scoring table, of which eight were left after the final selection step. For Year 2, six variables were chosen in the end, while 20 of the 42 inputs originally presented to the scoring table were selected using it. For the MDS approach, $CC_{veg,\,W}$ was used as level 1 input while $fuzzy_{su}$, $CC_{veg,E}$, P_{Air}, $fuzzy_{af}$, $fuzzy_{mo}$, VPD and Lw_{out} #lag were used as level 2 inputs. For Year 2, T_{Soil40} was used as level 1 input, $CC_{veg,\,W}$, $CC_{veg,E}$, VPD, $fuzzy_{mo}$, T_{Soil5}, $Redox_{10}$ and T_{Soil40} as level 2 inputs. The selection of model inputs thus resulted in both years with a focus on the footprint class contributions CC_{veg} and peat temperatures. In Year 1, they were indirectly addressed by Lw_{out} #lag (being a measure of surface temperature) and $fuzzy_{su}$ which is highly correlated with T_{Soil40} (r = 0.86).

Diurnal and seasonal cycles were highly weighted by the inclusion of higher frequency fuzzy variables and VPD in both years. The selection of $Redox_{10}$ in Year 2 gives further confidence that our framework is able to identify physically meaningful driving variables as soil redox conditions are known to be a major limiting factor for methane production in soils. To quantify the ability of the selection scheme to remove redundant inputs, I calculated the condition numbers of the input matrices throughout the selection process (see figure 5.5). I used this measure as an indicator for relations between the inputs. The lower its value, the less related the inputs are among each other. The condition numbers drop by two orders of magnitude between the original dataset and the selection result in both

years, suggesting a successful removal of redundancy in the input matrices.

Model optimization. Results of the performed model parameter optimizations are shown in table 5.4 and figure 5.10. Regarding the look-up table steps within MDS gap-filling, the limits defining similar conditions were found as described in the methods section 4.4.3. This two-step approach mostly resulted in narrowing down the limits after step two. The AIC based #HLN optimization for the applied RBF and MLP models is also described in the methods section. The results are presented in figure 5.10. The #HLN of the GRNN were not optimized due to model architecture. In this kind of regression the number of hidden layer units is always equal to the number of available target values. Nevertheless, the high #HLNs of 3007 in Year 1 and 939 in Year 2 illustrate the fact that the complexity contained in this model type is much larger than in a MLP or RBF network. For both these models the complexity needed to explain the data is lower in Year 2, suggesting that the information embedded in the used soil variables is more meaningful than in the meteorological inputs being the only ones available in Year 1. Comparing the MLPs' and the RBF networks' hidden layer sizes, the MLPs are less complex while describing the data better in both years.

Model comparison. The different measures along which the resultant five model types were compared are shown in tables 5.2 and 5.3. Each model type was evaluated with five datasets. It was compared to the target values used for model calibration and to the same time series, but extended by lower quality (MF1) measurement data. This step elevates the number of samples used in the calculation of statistics, although it most likely also introduces noise due to the lower quality of the new data. These values are nevertheless independent from fitting and thus provide a first level of generalizability estimation. A considerably higher level of independence was achieved by simulating the models whose parameters were optimized with Year 1 data with input and target records from Year 2. Results of this generalization check are given in table 5.3 with dataset C. This kind of model validation was not possible the other way around - evaluating Year 2 models with Year 1 inputs and targets - as no soil variables were measured in Year 1. With datasets B and A, two stages of progressively lower generality are available for evaluation of Year 1 and Year 2 models. Looking at these four sets of statistics, the MLP models outperform all other ones with respect to AIC, although differences to the RBF networks and the MLR models are rather small. Due to their high complexity, all GRNN models are characterized by comparably large AICs although their correlation coefficients are the highest and their RMSEs, as well as their mean absolute errors (MAEs), are the lowest among all models. Regarding r and RMSE of the remaining model types, the MLPs again outperform all other models. The scaling exponents α of the non-gap-filled datasets are -0.49

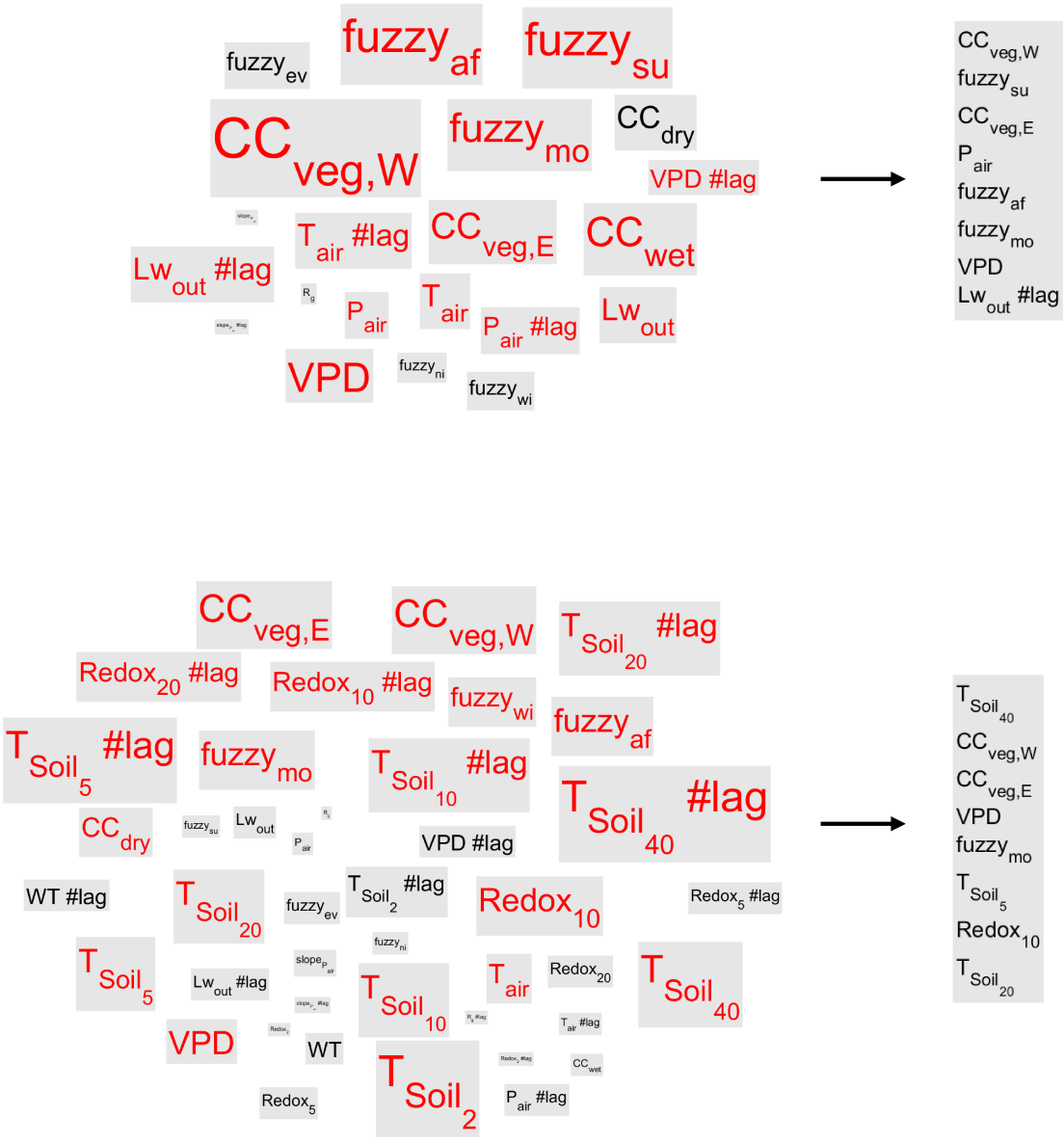

Figure 5.3: Result of the I-SIM input selection scheme for each of the two years of Himmelmoor methane flux data. Fontsizes represent the points a variable received via the scoring table. Variables highlighted in red had a score above the defined threshold and were presented to the final stepwise MLR which selected the inputs to the right of the arrow. If "# lag" is put behind a variable, it means that the the time series has been shifted by the time lag given in table 4.1. Top: Year 1, Bottom: Year 2

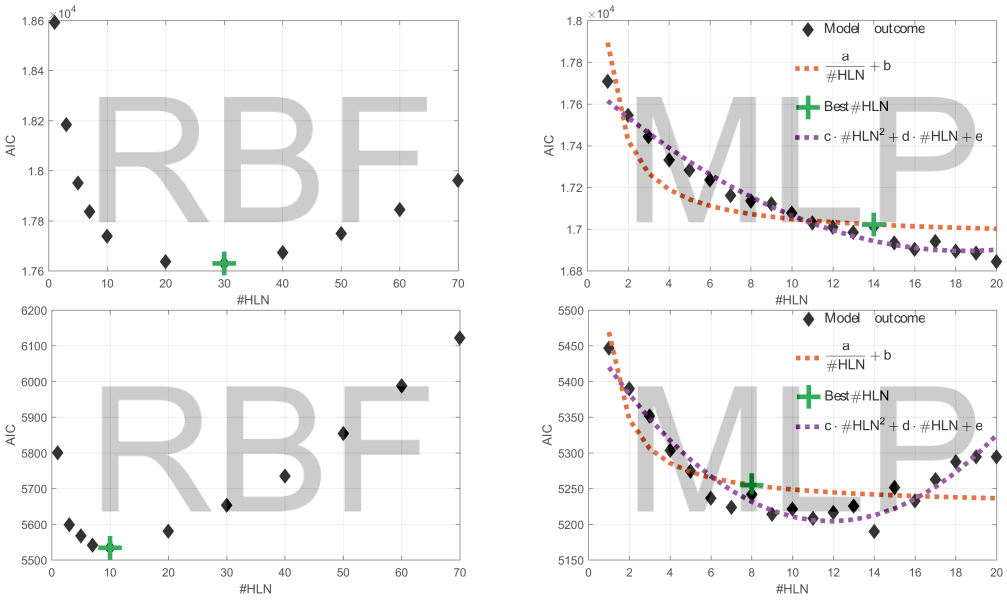

Figure 5.4: Hidden layer size optimization of the employed Himmelmoor methane flux ANN models. Each black diamond marker represents the outcome of a model ensemble. These committee machines were tested with different hidden layer sizes in order to determine an adequate number of hidden layer nodes. Top: Year 1, Bottom: Year 2.

Table 5.2: Himmelmoor Year 1 methane flux models compared with Year 1 fitting targets (A) and lower quality methane fluxes (B). B includes quality class MF1. RMSE, BE and MAE in nmol m^{-2} s^{-1}. MLR: multilinear regression, MDS: marginal distribution sampling, MLP: multilayer perceptron, RBF: radial basis function, GRNN: generalized regression neural network, RMSE: root mean squared error, BE: bias error, MAE: mean absolute error, AIC: Akaike information criterion.

	MLR	MDS	MLP	RBF	GRNN	
r	0.68	0.74	0.80	0.77	0.89	
RMSE	19.65	18.14	16.08	16.97	12.37	
AIC	17945.14	-	17000.93	17696.71	51273.37	A
BE	-0.00	1.01	-0.11	0.07	0.34	
MAE	13.73	11.70	10.78	11.54	8.24	
scaling exponent	-0.90	-0.47	-0.91	-1.02	-0.91	
r	0.57	0.63	0.68	0.66	0.72	
RMSE	31.11	29.74	28.05	28.66	26.65	
AIC	29927.26	-	29243.05	29782.75	64628.19	B
BE	1.98	3.36	1.62	2.06	2.14	
MAE	18.10	16.14	15.23	15.90	13.38	
scaling exponent	-0.90	-0.62	-0.91	-1.02	-0.91	

Table 5.3: Himmelmoor Year 2 methane flux models compared with Year 2 fitting targets (A) and lower quality fluxes (B). B includes quality class MF1. To yield dataset C, Year 1 models were simulated with Year 2 inputs and compared with Year 2 targets. RMSE, BE and MAE in nmol m^{-2} s^{-1}.MLR: multilinear regression, MDS: marginal distribution sampling, MLP: multilayer perceptron, RBF: radial basis function, GRNN: generalized regression neural network, RMSE: root mean squared error, BE: bias error, MAE: mean absolute error, AIC: Akaike information criterion.

	MLR	**MDS**	**MLP**	**RBF**	**GRNN**	
r	0.61	0.58	0.78	0.69	0.84	
RMSE	18.57	19.29	14.87	17.04	13.09	
AIC	5520.49	-	5246.64	5552.23	16114.30	A
BE	-0.00	2.51	-0.10	0.15	0.87	
MAE	12.79	12.05	9.95	11.32	8.65	
scaling exponent	-0.93	-0.35	-0.89	-0.91	-0.81	
r	0.64	0.62	0.75	0.66	0.75	
RMSE	28.55	29.99	25.32	28.26	25.08	
AIC	8908.83	-	8700.83	9050.17	19791.99	B
BE	1.88	4.96	1.50	2.38	2.51	
MAE	17.26	17.07	14.51	16.11	13.54	
scaling exponent	-0.93	-0.53	-0.89	-0.91	-0.81	
r	0.51	0.64	0.54	0.50	0.43	
RMSE	20.33	18.00	19.98	20.97	21.76	
AIC	5690.69	-	5906.26	6316.80	41864.49	C
BE	-0.43	1.39	0.13	5.10	3.69	
MAE	14.13	11.42	13.63	13.28	14.00	
scaling exponent	-0.88	-0.38	-0.88	-0.90	-0.81	

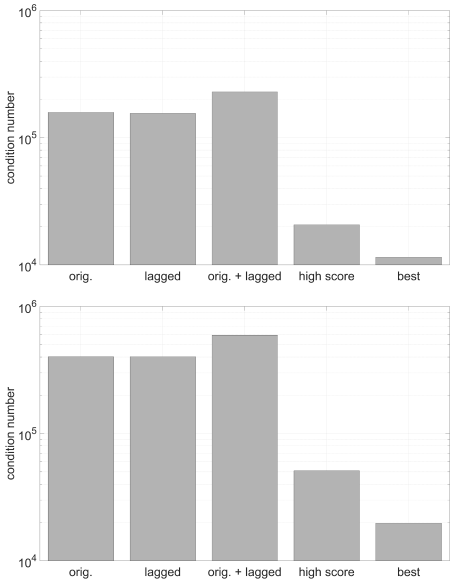

Figure 5.5: Condition numbers of the different input matrices used in Himmelmoor I-SIM methane flux modeling. orig.: unaltered input matrix, lagged: time shifted variables, high score: I-SIM scoring table result, best: final I-SIM input selection result. Top: Year 1, Bottom: Year 2

Table 5.4: Initial limits (Lim_{init}) and final limits obtained with iterative sampling with random values and as used for Himmelmoor F_{CH4} gap-filling (Lim_{gf}) with the MDS approach (section 4.4.3). See table 4.1 for variable descriptions and units.

Variable	Lim_{init}	Lim_{gf}
	Year 1	
$CC_{veg,\ W}$	0.02	0.10
$fuzzy_{su}$	0.25	0.06
$CC_{veg,\ E}$	0.33	0.04
P_{Air}	0.33	1.28
$fuzzy_{af}$	0.45	0.25
$fuzzy_{mo}$	0.45	0.06
VPD	296.96	1296.62
Lw_{out} #lag	24.52	15.92
	Year 2	
T_{Soil40}	0.76	0.74
$CC_{veg,\ W}$	0.11	0.06
$CC_{veg,\ E}$	0.29	0.36
VPD	2983.31	377.66
$fuzzy_{mo}$	0.45	0.05
T_{Soil5}	7.45	7.22
$Redox_{10}$	176.15	106.51
T_{Soil20}	5.14	3.13

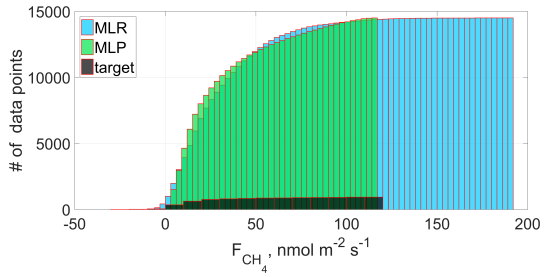

Figure 5.6: Cumulative histogram of Himmelmoor target values, MLR and MLP model results. The MLR model exeeds the value range spanned by the target values, the MLP approximates the range better.

in Year 1 and -0.35 in Year 2. Therefore, some pink noise (i. e. an intermediate correlation structure) is contained in both years, whereas Year 2 data is closer to being governed by white noise. Except for the MDS approach, all model types introduce autocorrelation to the data. These models manipulate the time series' frequency content in a way that α is lowered to values of around -1 denoting pink noise. The diurnal and 1/12 hours peaks present in the original data are enhanced by all models (see figure A.9). The MDS model introduces additional high frequency spikes upwards of 1/6 hours. The 1/6 hours peak is also present in the transformed RBF time series. These spikes could be the result of overfitted variations in diurnal cycles rather than being a depiction of real processes. Neither have the other models developed those spikes nor can they be found in the transformed target time series.

The generalization check reveals overfitting tendencies in some models. GRNN performance deteriorates the most from A over B to C showing that it is overly adapted to noise in the target data and

not of good explanatory power in a general sense. The relative consistency in the performance of the MDS method might be attributed to the fact that the generalization check was not completely independent from Year 2 targets. MDS averaging samples were taken from the Year 2 F_{CH4} time series due to the model principle. The dataset C statistics of all other models are characterized by dropping correlation coefficients and rising AICs with the MLR having the lowest AIC and the MLP having the highest r. The BEs of the RBF and GRNN networks jump to comparably high values. The bias errors (BEs) of the MLPs are consistently low throughout all test datasets. For dataset C, the absolute BE of the MLR is more than 3 times higher than the MLP BE. Although with this dataset, the MLR results in a slightly better AIC than the MLP, I found that it also extrapolates from the range of target values quite drastically (see 5.6). It produces values up to 64 % larger than the maximum target flux and more then ten times more negative values than the MLP model (427 vs. 34 values, 53 in the target time series). Thereby the MLR predicts values outside the scope of the training targets. Since no information could be provided to the MLR about this solution space during optimization, results in these regions are purely driven by noise and not by data. Overall, I assume that the MLP models explain the target fluxes best and in the most general sense.

5.3 Carbon dioxide flux gap-filling

5.3.1 Himmelmoor

Quality filtering. In order to yield a high-quality target time series for modeling, quality filtering was done rather harsh and led to a removal of 49 % of all measured CO_2 fluxes throughout the process illustrated in figure 5.8. The percentages given hereafter always refer to the preceding filtering step. While 6 % of the fluxes were omitted due to the instrument's signal strength (AGC) not fulfilling the defined requirements (see 4.2), the majority of fluxes were removed because the gas flux itself (20 %) or sensible or latent heat flux of the same half hour (21 %) were assigned to quality class MF2. Less data points (11 %) were removed applying the skewness and kurtosis test. However, this step was more effective in removing outliers than the preceding ones and reduced the time series' range rigorously. The footprint filter removed another 3 %, the absolute limits filter below 1 % of data. Up to this point, all MF1 values had been eliminated from the time series, thus the last filter searching for data points of this quality class had no effect on the final modeling target.

Input selection. Of the 23 input variables that were fed into the I-SIM algorithm for Year 1, 11 were selected using the scoring table of which nine variables constituted the final input matrix (see 4.4). With respect to Year 2, 41

variables were presented to the selection routine that resulted in 21 inputs being passed from the scoring table to the last two filters that reduced the input space to its final size of 13. As also the case with the CH_4 flux models, the I-SIM input selection led to a reduction of linear dependencies within the input matrix, what can be proved likewise by dropping condition numbers (figure 5.7). The resultant model inputs are shown in figure 5.9. Both input matrices contain measures for the main driver of photosynthesis which is radiation. In Year 1 PAR and R_g were selected, in Year 2 only the lagged derivative of PAR. More emphasis on the impact of plant-activity on CO_2 fluxes is put by the inclusion of $CC_{veg,W}$ and $CC_{veg,E}$ also in each year. In Year 2, also CC_{dra} was selected, what may point towards a response of carbon dioxide release to respiration from the drained surface class what would furthermore be reflected in the inclusion of surface near time shifted soil temperatures and redox potentials. T_{air} contains both seasonal and diurnal information and is part of the input matrices. This type of frequency content is also divided among the slow and fast changing fuzzy variables that belong to both final input spaces as well.

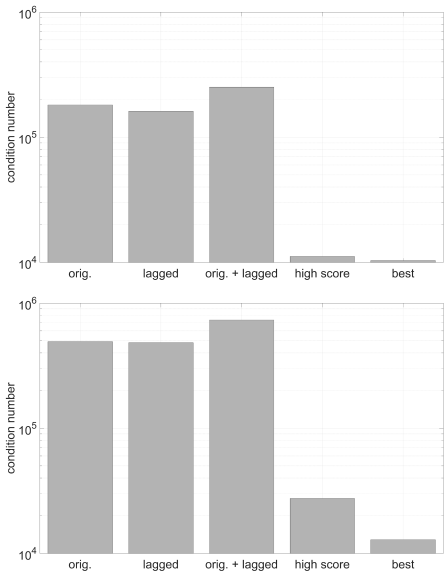

Figure 5.7: Condition numbers of the different input matrices used in Himmelmoor I-SIM carbon dioxide modeling. orig.: unaltered input matrix, lagged: time shifted variables, high score: I-SIM scoring table result, best: final I-SIM input selection result. Top: Year 1, Bottom: Year 2

Model optimization. In both years the best #HLN for the MLPs was found to be 8 and came from the result of the asymptote fit method (#HLN2, figure 4.5). The RBF networks' #HLN optimization yielded 30 hidden layer nodes (HLNs) in Year 1 and 40 HLNs in Year 2. Analogous to F_{CH4} modeling, the GRNNs' hidden layer size was not optimized due to the GRNN architecture. For this model type, the #HLN is set to be equal to the number of available target values (4798 in Year 1 and 4752 in Year 2), resulting in models that are far more complex than the RBFs or MLPs, whereas the latter contain the least parameters of all ANNs.

Model comparison. Similar to the results of F_{CH4} modeling, the MLP approximations of the target time series appear to be the most trustworthy. Their AIC values are the lowest across all evaluated datasets (see tables 5.5 and 5.6). To obtain different levels of generalization tests, model results were evaluated in 5 different ways. Statistics were assessed for Year 1 and Year 2 in comparison with the quality filtered target time

series and with the same dataset but including MF1 quality fluxes. Additionally, the models estimated with Year 1 data were tested with Year 2 inputs and targets. These statistics (dataset C in table 5.6) provide the most robust assessment of generalization capability. The GRNNs perform best regarding their correlation coefficients and RMSE. The large complexity of this model type deteriorates, however, its AICs. Most importantly, only with dataset C the GRNN model does not result in the highest r value meaning that the high correlations in the other comparisons can be attributed to overfitting. With dataset C, the MLP models have the highest r and lowest AIC, what leads to the previously anticipated conclusion of them being the most trustworthy. The MDS model performs r-wise equally good. It furthermore stands out by introducing the least autocorrelation with a scaling exponent of -0.49, compared to -0.55 of the target timeseries. The MDS method even adds some white noise (α = 0), whereas all other models shift the spectrum towards pink noise (α = -1) and thereby introduce intermediate correlation. The RBFs perform very similar to the MLPs, but in all cases not quite as good as them, what is connected to their larger complexity.

5.3.2 Rio Pipo

Input selection. Passing all inputs through the I-SIM input selection yielded the final model input matrix containing 13 of the 46 possible variables, 23 of which were selected using the scoring table outcome. The condition number of the input matrix drops by two orders of magnitude throughout the selection process, indicating a removal of linear dependencies. Being mainly comprised of spectral content on seasonal and diurnal timescales, the radiation variables R_g, PAR and Sw_{out} are part of the final input space. The diurnal component was further emphasized by the inclusion of soil temperatures and the high frequency fuzzy variables, $fuzzy_{af}$ and fuzzy variable *evening* ($fuzzy_{ev}$). Eight out of all selected model inputs are soil temperatures of which three are the lagged derivatives of the original variables. The Cross-covariance series with F_{CO2} show very undistorted daily cyclicality while their amplitudes drop with the depth of the temperature measurement in the soil profile. The timelags between input variables and target flux are calculated within I-SIM based on the transformation of the cross-covariance series into a normalized cross-correlation (see 5.13). Among the three lagged soil temperatures that are part of the final input matrix, $T_{SoilSL,-10}$ is the only one with the highest correlation at a positive timelag (+ 1.5 hours), meaning that changes in CO_2 flux follow changes in soil temperature at this depth. Therefore, it is conceivable that a driving process of CO_2 flux on short timescales ($<$ 1 day) is connected to changes in soil temperatures at this depth. The remaining lagged soil temperatures seem to introduce seasonality and diurnality in a more fundamental way into the models.

Model comparison. Missing sharp contrasts in the surface cover of Rio

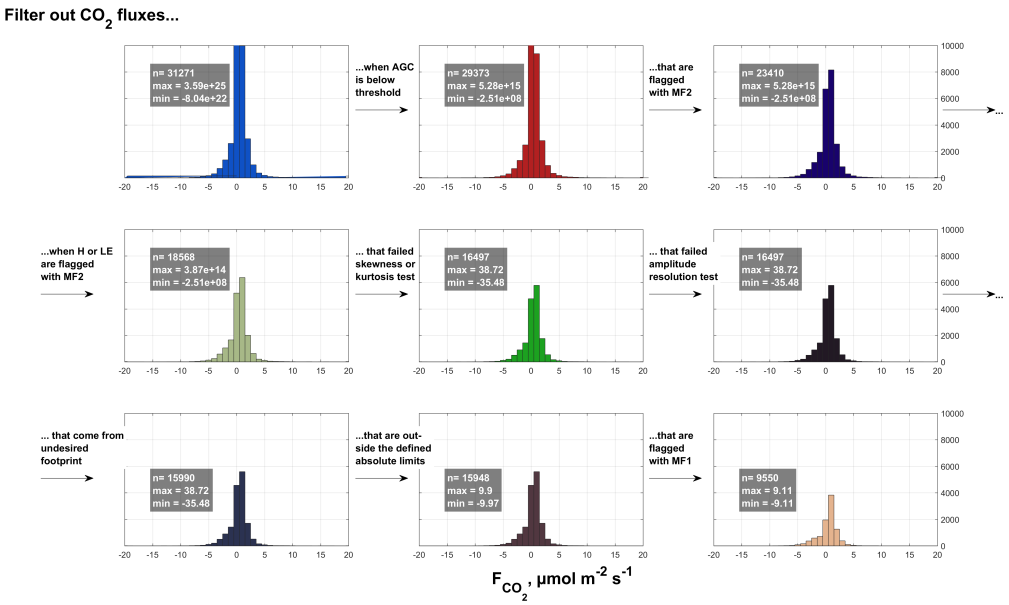

Figure 5.8: The effects of the different quality filtering steps on the distribution of the available two years of half-hourly Himmelmoor carbon dioxide fluxes. n: number of flux values, min: minimum flux, max: maximum flux, AGC: signal strength of the LI-7200 gas analyzer, MF1/MF2: flux quality classes after Mauder and Foken (2004).

Table 5.5: Himmelmoor Year 1 carbon dioxide flux models compared with Year 1 fitting targets (A) and lower quality methane fluxes (B). B includes quality class MF1. RMSE, BE and MAE in µmol m^{-2} s^{-1}. MLR: multilinear regression, MDS: marginal distribution sampling, MLP: multilayer perceptron, RBF: radial basis function, GRNN: generalized regression neural network, RMSE: root mean squared error, BE: bias error, MAE: mean absolute error, AIC: Akaike information criterion.

	MLR	MDS	MLP	RBF	GRNN	
r	0.61	0.72	0.79	0.78	0.85	
RMSE	1.29	1.13	0.99	1.02	0.88	
AIC	2477.63	-	71.13	944.53	62114.98	
BE	-0.00	0.02	-0.00	-0.00	0.01	A
MAE	0.89	0.73	0.66	0.68	0.58	
scaling exponent	-1.02	-0.49	-1.06	-1.04	-0.97	
r	0.51	0.60	0.68	0.67	0.70	
RMSE	1.34	1.27	1.15	1.16	1.11	
AIC	4721.23	-	2356.92	3090.18	64998.28	
BE	-0.02	-0.01	-0.05	-0.05	-0.03	B
MAE	0.90	0.80	0.73	0.75	0.69	
scaling exponent	-1.02	-0.55	-1.06	-1.04	-0.97	

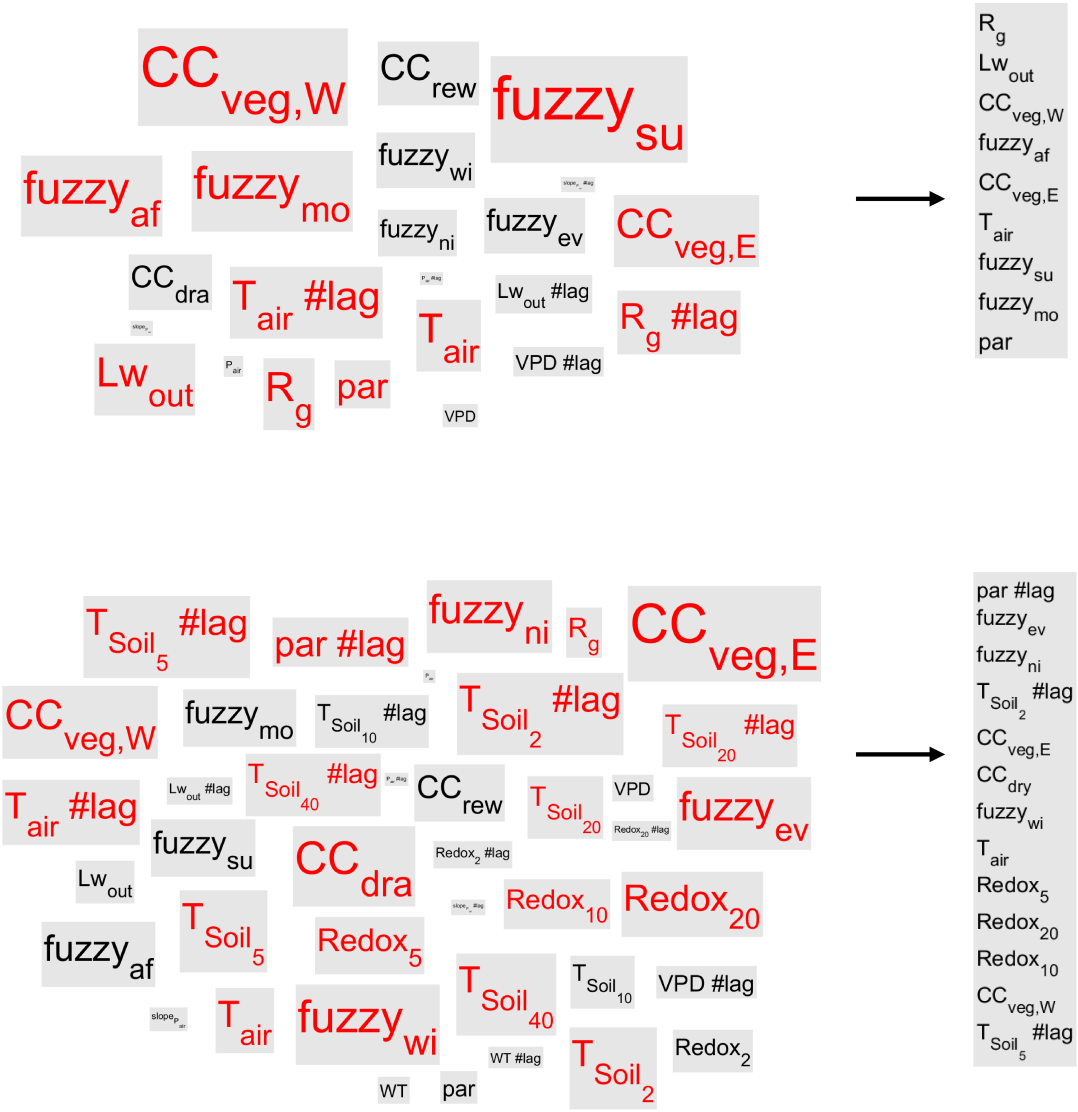

Figure 5.9: Result of the I-SIM input selection scheme for each of the two years of Himmelmoor carbon dioxide flux data. Fontsizes represent the points a variable received via the scoring table. Variables highlighted in red had a score above the defined threshold and were presented to the final stepwise MLR which selected the inputs to the right of the arrow. If "# lag" is put behind a variable it means that the the time series has been shifted by the time lag given in table 4.1. Top: Year 1, Bottom: Year 2

Table 5.6: Himmelmoor Year 2 carbon dioxide flux models compared with Year 2 fitting targets (A) and lower quality fluxes (B). B includes quality class MF1. To yield dataset C, Year 1 models were simulated with Year 2 inputs and compared with Year 2 targets. RMSE, BE and MAE in µmol m^{-2} s^{-1}. MLR: multilinear regression, MDS: marginal distribution sampling, MLP: multilayer perceptron, RBF: radial basis function, GRNN: generalized regression neural network, RMSE: root mean squared error, BE: bias error, MAE: mean absolute error, AIC: Akaike information criterion.

	MLR	MDS	MLP	RBF	GRNN	
r	0.74	0.74	0.88	0.86	0.92	
RMSE	1.36	1.18	0.97	1.02	0.77	
AIC	3003.12	-	-17.13	1580.30	83279.62	A
BE	-0.00	0.05	-0.00	0.00	0.03	
MAE	1.00	0.74	0.67	0.72	0.54	
scaling exponent	-0.98	-0.49	-1.09	-1.13	-1.01	
r	0.62	0.60	0.74	0.74	0.78	
RMSE	1.57	1.42	1.34	1.33	1.24	
AIC	7089.34	-	4822.66	5741.19	88937.49	B
BE	0.03	0.04	-0.03	-0.02	0.02	
MAE	1.09	0.87	0.83	0.86	0.75	
scaling exponent	-0.98	-0.55	-1.09	-1.13	-1.01	
r	0.62	0.74	0.76	0.72	0.71	
RMSE	1.58	1.18	1.35	1.47	1.47	
AIC	4412.04	-	3014.23	4315.89	66971.66	C
BE	-0.06	0.05	-0.30	-0.28	-0.27	
MAE	1.14	0.74	0.95	1.02	1.02	
scaling exponent	-1.01	-0.49	-1.10	-1.06	-0.95	

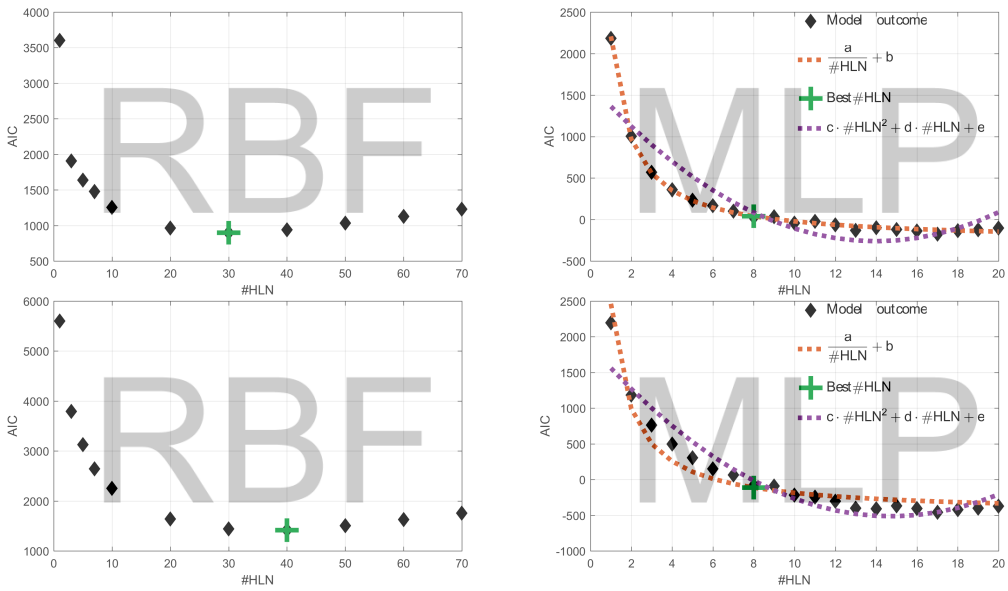

Figure 5.10: Hidden layer size optimization of the employed Himmelmoor carbon dioxide flux ANN models. Each black diamond marker represents the outcome of a model ensemble. These committee machines were tested with different hidden layer sizes in order to determine an adequate number of hidden layer nodes. Top: Year 1, Bottom: Year 2. RBF: radial basis function, MLP: multilayer perceptron.

Table 5.7: Rio Pipo carbon dioxide flux models compared with fitting targets (A) and lower quality fluxes (B). B includes quality class MF1. RMSE, BE and MAE in µmol m^{-2} s^{-1}. MLR: multilinear regression, MDS: marginal distribution sampling, MLP: multilayer perceptron, RBF: radial basis function, GRNN: generalized regression neural network, RMSE: root mean squared error, BE: bias error, MAE: mean absolute error, AIC: Akaike information criterion.

	MLR	MDS	MLP	RBF	GRNN	EPReM	
r	0.86	0.91	0.92	0.91	0.93	0.92	
RMSE	0.64	0.54	0.48	0.51	0.46	0.49	
AIC	-3909.84	-	-6246.16	-5261.64	73078.14	-6296.55	A
BE	< 0.01	0.01	< 0.01	< 0.01	< 0.01	0.03	
MAE	0.37	0.26	0.21	0.24	0.20	0.21	
scaling exponent	-1.49	-0.81	-1.43	-1.34	-1.34	-1.35	
r	0.62	0.65	0.67	0.66	0.67	0.67	
RMSE	1.27	1.23	1.21	1.22	1.20	1.21	
AIC	3260.32	-	2744.87	3301.10	82368.90	2630.31	B
BE	0.07	0.07	0.07	0.07	0.06	0.09	
MAE	0.59	0.50	0.45	0.48	0.45	0.46	
scaling exponent	-1.49	-0.84	-1.43	-1.34	-1.34	-1.35	

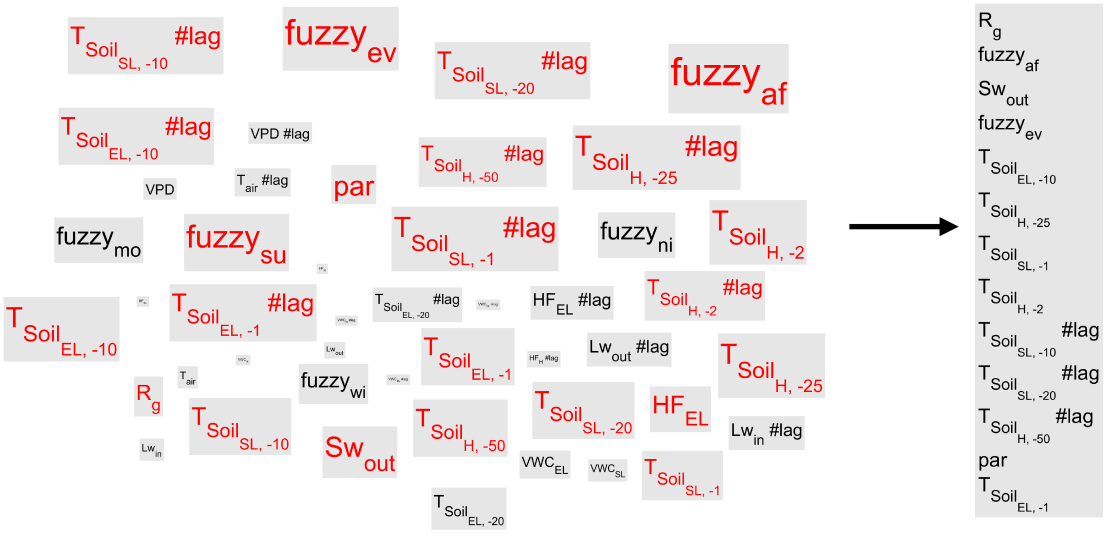

Figure 5.11: Result of the I-SIM input selection scheme for Rio Pipo carbon dioxide flux data. Fontsizes represent the points a variable received via the scoring table. Variables highlighted in red had a score above the defined threshold and were presented to the final stepwise MLR which selected the inputs to the right of the arrow. If "# lag" is put behind a variable it means that the the time series has been shifted by the time lag given in table 4.1.

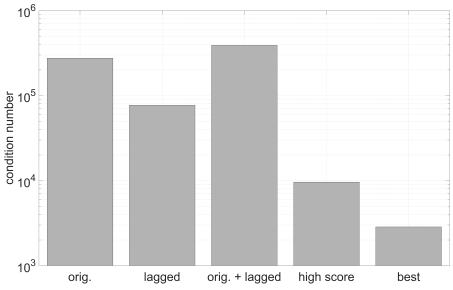

Figure 5.12: Condition numbers of the different input matrices used in Rio Pipo I-SIM carbon dioxide modeling. orig.: unaltered input matrix, lagged: time shifted variables, high score: I-SIM scoring table result, best: final I-SIM input selection result.

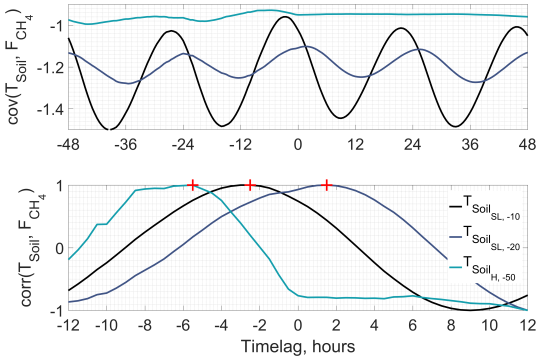

Figure 5.13: Cross-covariance and normalized cross correlation between soil temperatures and carbon dixoide flux at the Rio Pipo site.

Pipo bog justify the assumption of the EC footprint to be homogeneous. The assertion of comparability between TVTS flux values of different points in time is further substantiated by the fact that during the measuring period, wind came almost exclusively from one direction (see figure 3.1). A mechanistic approach to modeling in such a setting seemed feasible and was tested by employing the half-hourly EPReM (see section 4.5). This model consists of a combined estimation of ecosystem respiration (R_{eco}) and photosynthesis and is in fact suitable to explain the variability in the measurement data. During the first, parameter constraining step of EPReM, Q_{10} was determined to be 1.23 and fixed at this value. Most EPReMs could be fitted using window sizes of 2 days as shown in figure 5.17. For each day, a significant value for α could be inferred. Consequently, EPReM complexity was not reduced further and 3-parameter models were fitted to each day. The resultant daily EPReMs were driven with half-hourly radiation data to generate the time series that was compared to I-SIM models. Using AIC as a figure of merit, the mechanistic model type is superior to the empirical models included in I-SIM. The different predictions were evaluated with the dataset used for model calibration (dataset A in table 5.7) and with a time series containing also target fluxes of the lower quality class MF1 (dataset B in table 5.7). The latter is the highest level of generalization test available with Rio Pipo fluxes. Except for petty AIC differences, the MLP performs similar to the EPReM in both tests. The MLP

outcompetes the other ANNs, whereas the GRNN fall behind due to their high #HLN resulting in AICs that are far off the range of the remaining models. The RBF and MDS statistics resemble MLP figures in general but contain larger error terms. The relatively equal distribution of short and the absence of long gaps in the target time series improves all model performances compared to the I-SIM results of Himmelmoor. The quality of the MDS models benefits notably from this circumstance as 99 % of the gaps could be filled with output from quality class A. The MLRs have the highest root mean squared and mean absolute errors, but surpass the RBF AIC in dataset B still not outperforming the MLP or the EPReM, though.

5.4 Parameters of mechanistic ensemble models

In an effort to separate the influences of the vegetated strips and the bare peat areas in Himmelmoor on net F_{CO_2} expressed in the SCTS, a combined ecosystem respiration photosynthesis model (see section 4.7) was fitted to monthly ensembles of the half-hourly Himmelmoor SCTS. The obtained parameter time series are shown in figure 5.15. In general, the vegetation period, with its productivity maximum between June and July and its cessation between mid-October and November is well depicted in the seasonal course of mechanistic parameters throughout both years. More importantly, also their absolute values appear to be coherent with literature data from similar plants or vegetation communities as found in Himmelmoor (see chapter 6). Using relative class contributions of contrasting surface types to scale single terms in a mechanistic model has thus proven to be feasible. Moreover, the division of the TVTS into SCTS appears to yield reasonable flux estimates that can be explained in a mechanistic way.

For comparability with Himmelmoor light saturation and respiration parameters, Pipo net ecosystem exchange (NEE) was compiled into monthly groups to which an EPReM with fixed Q_{10} was fitted. The individual monthly fits are shown in figure 5.14, whose resultant parameters are overlaid with daily results from EPReM in figure 5.16. The fact that the monthly parameter time series coincide well with the progression of the daily parameter sets throughout the year, gives further confidence in the ability of the ensemble method to yield meaningful plant physiological properties also on a monthly basis. Furthermore, this result underlines the homogeneity of the EC source area in Rio Pipo bog. More footprint variability in the monthly datasets would have introduced more noise into the relationships of PAR and NEE. If more pronounced, dissimilar EC fetch areas could have translated into two or more separate curve shapes within each monthly plot, denoting properties of diverse plant communities.

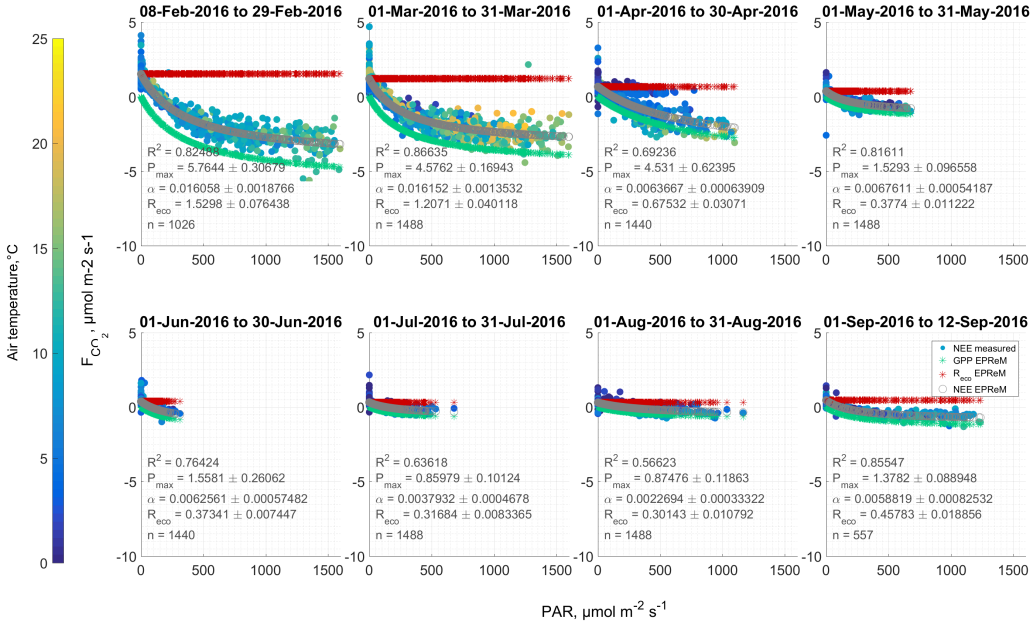

Figure 5.14: Light saturation fits to monthly ensembles of half-hourly Rio Pipo net ecosystem exchange.

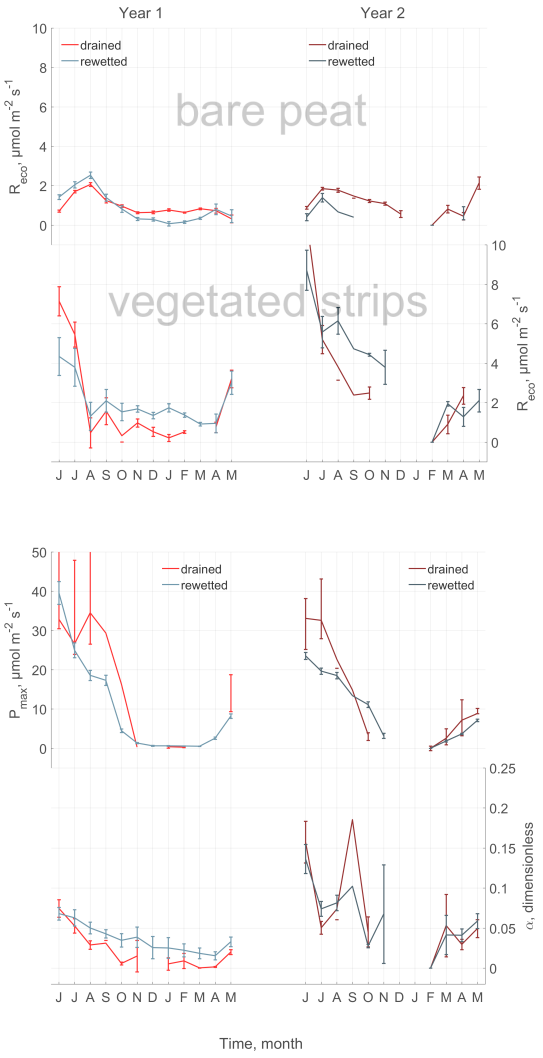

Figure 5.15: Parameter time series of combined photosynthesis and respiration models fitted to monthly thirty minute flux ensembles. This method allows for a mechanistic interpretation of the surface class level results gained with I-SIM. Top panel: Ecosystem respiration parameters divided by bare peat and vegetated areas within the surface classes *drained* and *rewetted*. Bottom panel: Photosynthesis parameters that were obtained by scaling the model term with the relative contribution of the vegetated surface class to the EC footprint.

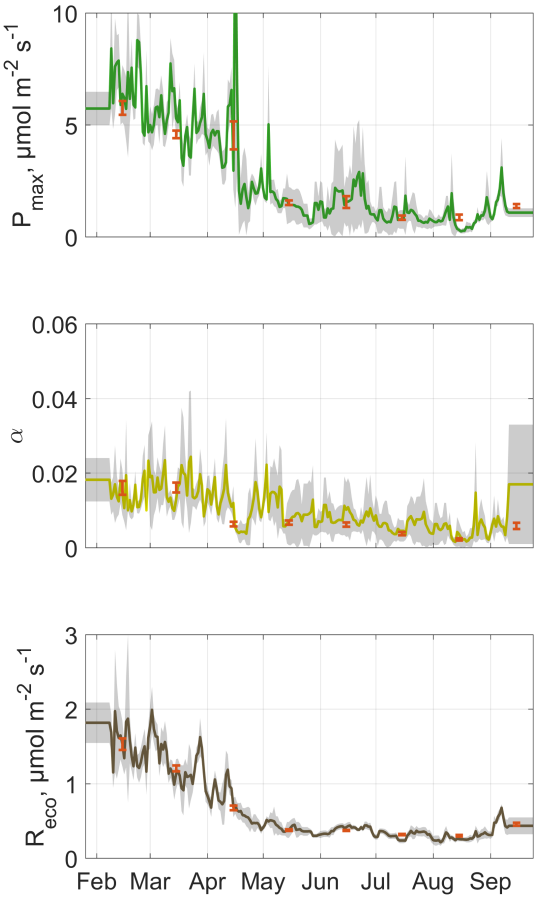

Figure 5.16: Rio Pipo EPReM parameter time series. Lines represent half-hourly model results, red bars denote the values obtained from monthly ensemble fits.

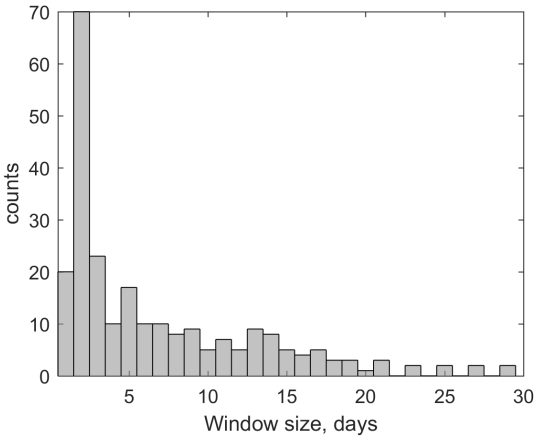

Figure 5.17: Histogram of EPReM window sizes used during Rio Pipo carbon dioxide flux gap-filling

5.5 Cumulative sums of carbon gas fluxes

Himmelmoor's cumulative annual sums of gas fluxes were calculated based on their gap-filled time series as described in section 4.8. The results are expressed as molar fluxes (figure 5.18) and as release of CO_2eq (figures 5.19 and 5.20). Factors to convert F_{CH4} into CO_2eq release were taken from the Fifth Assessment Report of the Intergovernmental Panel on Climate Change (IPPC AR5, Myhre et al., 2013). The impact of rewetting on the development of vertical carbon release is well documented with the shown results. Overall, the relations between GHG fluxes from the rewetted and the drained surface class as well as their trends from Year 1 to Year 2 display the anticipated behavior. Annual F_{CO2} from the restored site undercuts the summed up CO_2 emissions from the drained part of Himmelmoor in both years, whereas the difference increases with time. Annual CH_4 release from the wetter surfaces exceeds the cumulative F_{CH4} from the drained mining site in both years. Both fluxes rise from Year 1 to Year 2.

In Year 1, F_{CO2} from the rewetted area was already cumulatively lower than from the mining site (20.16 $\pm$ 0.36 vs. 22.48 $\pm$ 0.30 mol m^{-2}). It dropped by over 35 % in Year 2, increasing the difference to the cumulative mining site flux to over 40 % (12.91 $\pm$ 0.29 vs. 22.16 $\pm$ 0.28 mol m^{-2}). At the end and the beginning of Year 2 (i.e. in summer) the cumulative curve of SC_{rew} ceases to slope upwards. By reaching these vertexes, the points in time when the rewetted area turns from a CO_2 source into a sink are indicated. Nevertheless, on an annual basis the periods when the sink character of SC_{rew} prevails do not yet compensate for CO_2 release during timespans of reduced plant activity. CH_4 fluxes from both surface classes rise from Year 1 to Year 2, whereas their absolute difference stays constant. The cumulative CH_4 flux from SC_{rew} is 84 % higher than from SC_{dra} in Year 1(0.45 $\pm$ 0.01 vs. 0.83 $\pm$ 0.01 mol m^{-2}) and 51 % higher in Year 2 (0.76 $\pm$ 0.01 vs. 1.15 $\pm$ 0.01 mol m^{-2}). Compared to the molar F_{CO2} sum of both surface classes, cumulative CH_4 release is a factor of around 30 smaller in Year 1 and about 20 times smaller in Year 2. The development of both molar GHG emissions over time documents the rising importance of CH_4 in the course of rewetting.

The results are also expressed as GWP and global temperature change potential (GTP). These two metrics are commonly used to quantify the climate impact of various GHGs' emissions. In order to convert non-CO_2 gas emissions to release of CO_2eq, factors from AR5 were applied. The metrics are defined in distinct ways and yield different conversion factors. GWP is the integrated effect of radiative forcing over a certain time window. Different conversion factors are given for different window sizes. Hence, GWP puts weight on the period before the time window maximum and none on the period thereafter. In contrast, GTP is an end-point statistic giving the temperature response of the climate system at a certain point in time, not weighing

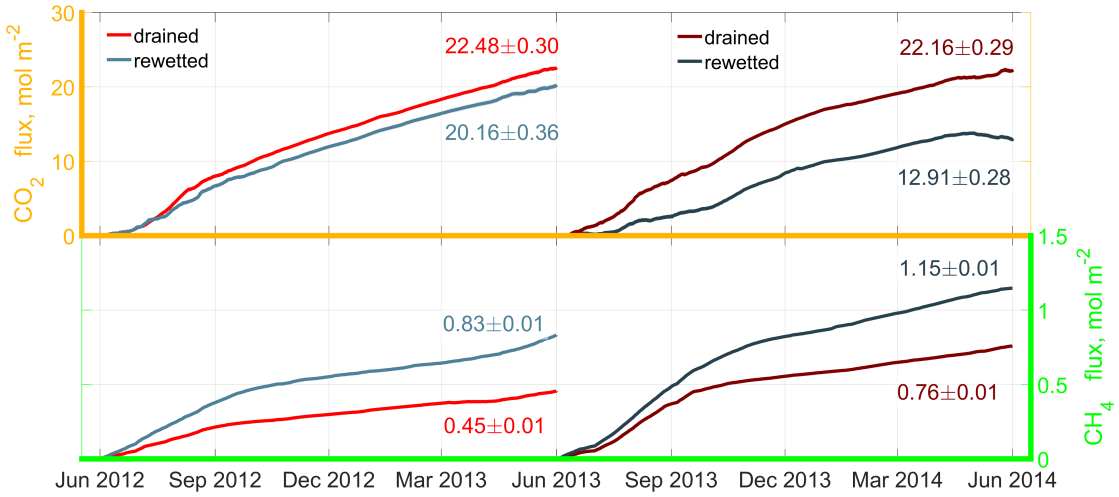

Figure 5.18: Cumulative molar carbon gas flux sums on surface class level. Himmelmoor dataset.

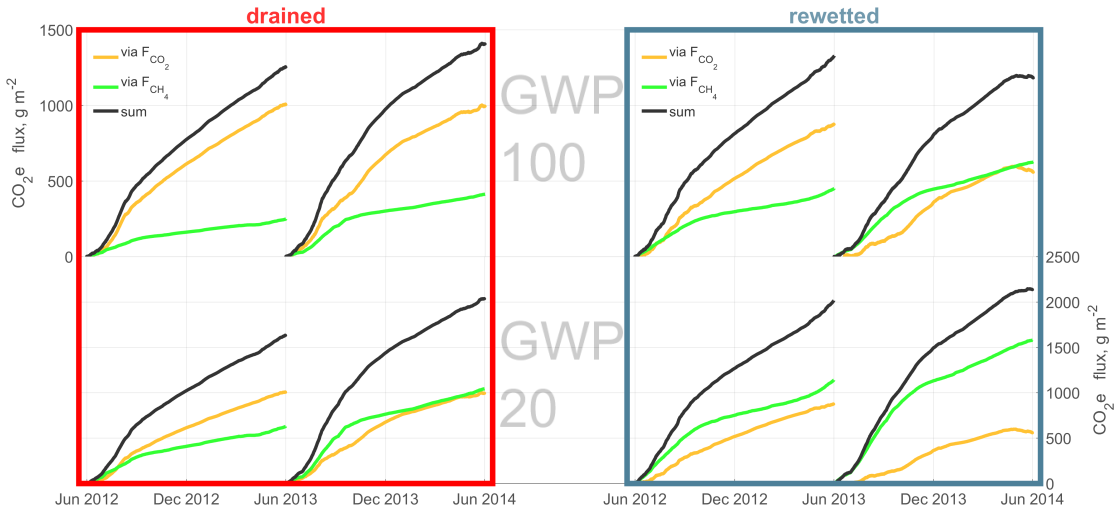

Figure 5.19: Annual sums of Himmelmoor greenhouse gas release expressed in carbon dioxide equivalents (CO_2eq). The conversion factors for global warming potential from IPCC AR5 including climate-carbon feedbacks are used. Results are given on 100 years and 20 years time horizons.

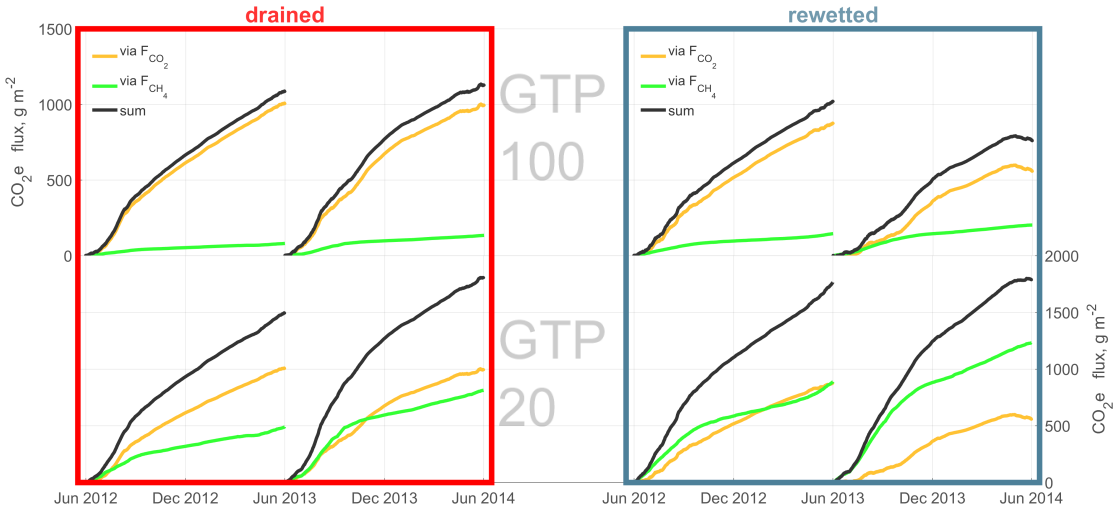

Figure 5.20: Annual sums of Himmelmoor greenhouse gas release expressed in CO_2eq. The conversion factors for global temperature change potential from IPCC AR5 including climate-carbon feedbacks are used. Results are given on 100 years and 20 years time horizons.

the timespan before or after. While in the preceding IPCC Assessment Report AR4 climate-carbon feedbacks were only included for CO_2, in AR5 also factors for CH_4 including climate-carbon feedback are reported (Myhre et al., 2013). These values, on time horizons of 20 and 100 years, were used for conversion in this study. Transforming the molar cumulative sums into sums of CO_2eq allows for comparability between the two GHG fluxes from the two surface classes regarding their climate impact. The sum of cumulative F_{CO2} and F_{CH4} coming from SC_{dra} are dominated by F_{CO2} in both years and across nearly all metrics, except for global warming potential on a 20 years time horizon (GWP20) where F_{CO2} and F_{CH4} amount to about 50 % of their sum each. Looking at the relations between CO_2 and CH_4 release from SC_{rew}, F_{CH4} sums exceed CO_2 emissions in two settings: on short time horizons and/or in Year 2. Although the cumulative F_{CH4} global warming potential on a 100 years time horizon (GWP100) also increases from Year 1 to Year 2, it mainly dominates the SC_{rew} sum due to a large drop in F_{CO2} from Year 1 to Year 2. On short time horizons this interannual variability is reflected as well but SC_{rew} CH_4 emissions exceed CO_2 release in both years.

Three summer and five winter months are available to establish a comparison between CO_2 fluxes from the undisturbed Rio Pipo bog and the different surface classes in Himmelmoor (see figure 5.21). This dataset obviously does not allow for a comparison of vertical carbon release on an annual basis but provides insight into the different ecological processes contributing to the observed net carbon fluxes. In general, Rio Pipo is a net-sink for CO_2 in summer and a source in winter, whereas cumulative winter CO_2 release is three times smaller compared to Himmelmoor CO_2 emissions in an equivalent time span. Himmelmoor carbon dioxide exchange during three summer months sums up to about the same amount as

during five winter months, with the exception of Year 2 when cumulated CO_2 fluxes from the rewetted areas are over one third smaller than from the drained sites. Year 2 could indicate the beginning establishment of the restored areas as a summer CO_2 sink.

Looking at the average diurnal courses of NEE at the three different surface types (figure 5.22), the rewetted areas of Himmelmoor reach midday CO_2 fixation rate maxima in Year 2 that are similar to those of the pristine bog. This net-effect is, however, not the result of similar conditions. Photosynthesis of the vascular plant species in Himmelmoor is more effective in fixing atmospheric CO_2. Maximum photosynthesis (P_{max}) of the Rio Pipo moss-dominated plant community is for example in February a factor of four smaller than P_{max} from SC_{veg} in Himmelmoor in the corresponding northern hemisphere month of August. At the same time, however, ecosystem respiration from the strips inhabited by vascular plants in Himmelmoor is also much higher (two-fold) compared to the *Sphagnum magellanicum* bog. Ecosystem respiration from Rio Pipo rather resembles the values inferred for the bare peat areas of Himmelmoor (see figures 5.16 and 5.15).

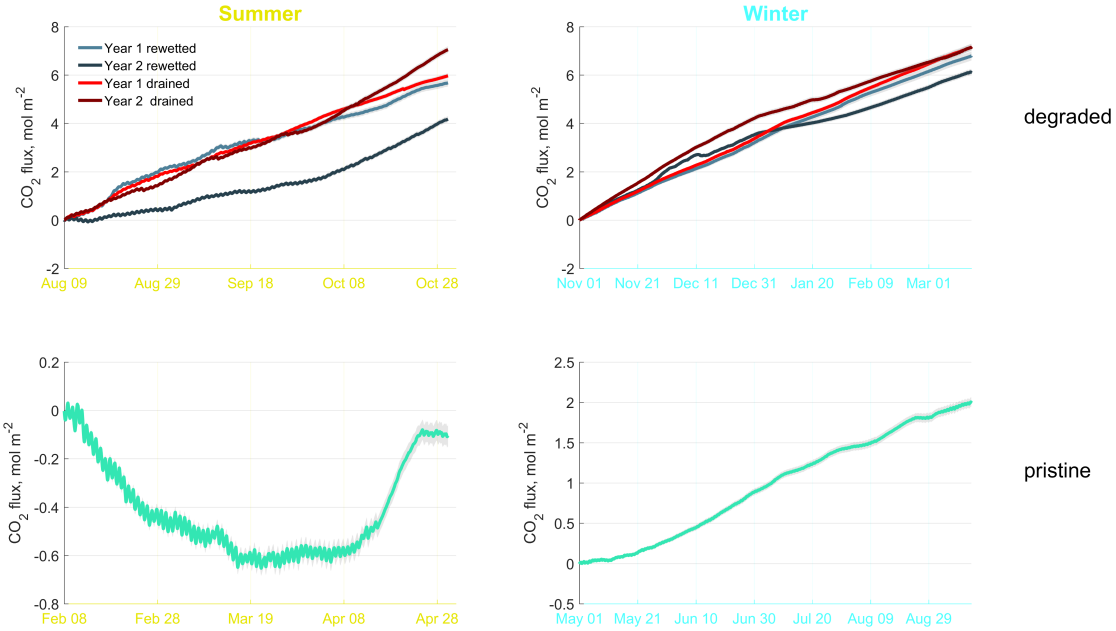

Figure 5.21: Comparison of cumulative summer and winter carbon dioxide fluxes from the three land use types investigated in this study. Top: Fluxes from rewetted and drained surfaces of the degraded site, Bottom: Fluxes from pristine mire; Note the dissimilar y-axis scaling. While both land use classes at the degraded site are carbon dioxide sources in summer and winter, the pristine site is a summer sink and a three times smaller source in winter.

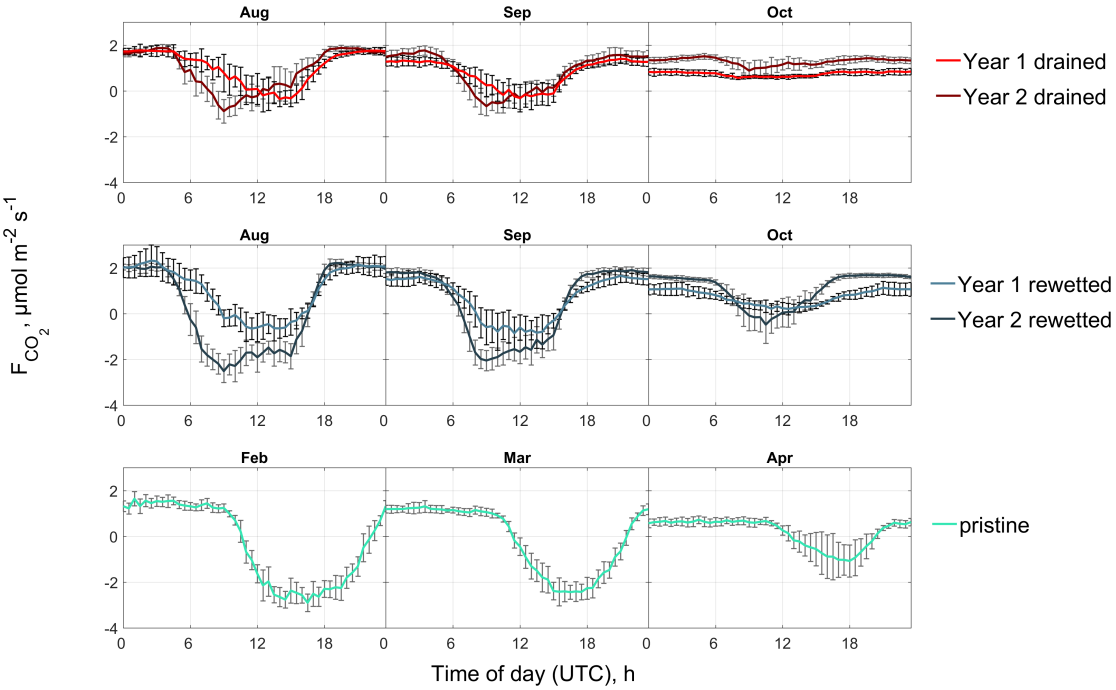

Figure 5.22: Monthly averaged diurnal cycles of summer net ecosystem exchange from all three studied surface types. Errorbars denote standard deviations of all half-hourly measurements used for calculating averages of a certain time of day.

Chapter 6

Discussion

6.1 Data processing and modeling

6.1.1 Quality filtering

My approach to quality filtering of half-hourly fluxes removed a large amount of data and is therefore rather harsh. Only the best available data were to be used for model fitting. In order to compile a gap-filled gas flux time series for the calculation of cumulative sums, more measurement data of lower quality was included back into it, and part of the filtering steps were reversed. This does, however, not apply to the $RSSI_{relStd}$ filter presented in the methods section. I think it is necessary to filter methane fluxes measured with a LI-7700 sensor in this manner. Our observations that methane concentration covary with RSSI values at 20 Hz and that large jumps in RSSI appear together with switching events in the LI-7700's mirror heaters make this filter essential to remove artificial high fluxes.

6.1.2 Model input selection

Data-driven selection. Connections of CH_4 fluxes to environmental drivers can be more complex and are to my knowledge not yet consolidated in a comprehensive, mechanistic approach to F_{CH4} gap-filling. This lack of a mechanistic explanations of CH_4 exchange might be owed to discontinuous features of methane producing and consuming processes. Above and below thresholds in environmental drivers like soil chemistry or vegetation properties, the various mechanisms leading to CH_4 release could be interconnected inherently different. Within a continuum of changes in driving variables, steps might exist in F_{CH4} responses when environmental properties transgress certain boundaries and cause ecological processes to systematically change. The complex interactions between drivers and flux response lead to empirical models commonly being employed (Dengel et al., 2013; Deshmukh et al., 2014; Forbrich et al., 2011; Hommeltenberg et al., 2014; Knox et al., 2015; Kroon et al., 2010; Sachs et al., 2008; Zhu et al., 2013, Goodrich et al. 2015a) for the purpose of F_{CH4} gap-filling. Empirical models involve parametric or non-parametric mapping of input variables to a target F_{CH4}. In contrast to mechanistic explanations, the resulting fitting parameters do not represent a

definable property of the measured system, though. Anyhow, with most authors, the choice of input variables reflects their conceptual perception of a cause-effect chain. This selection method takes into account the insight one has into reasons for variability in methane exchange prior to data analysis. To constrain model complexity by utilizing a priori knowledge about a system is perfectly fair and defendable. Nevertheless, the issue remains that there is only limited systematic information available about the coupling of processes that drive F_{CH4}. Connections might additionally be site-specific. For this reason, I opted for a data-driven input selection based on measurement data and not on arbitrary assumptions about flux driving processes. The goal of the I-SIM selection process was to filter out irrelevant and redundant variables from a potential input matrix containing measured biomet inputs, EC footprint information and fuzzy variables. The I-SIM scoring table, combines the response of multilinear and ANN models to differently manipulated versions of the inputs space. Lagged biomet variables were included as changes in environmental drivers commonly create shifted responses in gas fluxes.

Relevance of selected inputs. It cannot ultimately be appraised if the relevant input-target connections have been captured by the I-SIM routine. Nevertheless, physically sound explanatory frameworks for F_{CH4} variability can be outlined with the obtained results. In Year 2 of the Himmelmoor F_{CH4} dataset, the selection scheme preferred four peat temperatures and one soil redox potential, which are known (e. g. Couwenberg, 2009b) to drive methane production in soils. In both years footprint variables were included into the final input matrix. In Year 1, $CC_{veg,W}$ was chosen as MDS level 1 variable. It is evident that the presence of plants with aerenchyma in the footprint should influence the methane flux. In Year 2, four soil temperatures were included into the input matrix, whereas no soil variables were available in Year 1. Instead, the I-SIM algorithm selected fuzzy variables which contain similar spectral peaks like the real soil temperatures. $Fuzzy_{su}$ represents the low frequency portion of T_{Soil40} while $fuzzy_{mo}$ and $fuzzy_{af}$ emulate diurnal patterns included in T_{Soil5} and T_{Soil20}. Although this outcome does not mean that the physically meaningful processes have been captured comprehensively by the selection routine, it points to its ability to discriminate between weaker and stronger input-target connections which do not necessarily have to be linear. When cross-checked with six F_{CO2} target datasets, the I-SIM selection scheme did pick radiation inputs (five times PAR, one time R_g) that are known to be drivers of photosynthesis and that are thus also part of mechanistic NEE explanations.

Remaining linear dependencies. The removal of redundancy from the input spaces is measurable using the matrices' condition numbers that improved throughout the filtering process in every test case. Inspecting the correlation coefficients of individual input-input pairs nonetheless reveals that some linearly dependent in-

puts co-occur in the final input matrices. Linear dependency does, however, not necessarily imply spectral similarity of two inputs across the entire frequency band. Two variables can for example reach high correlation coefficients when both contain overriding seasonal cyclicity. If additional lower amplitude high frequency information is modulated on top of the long-wave content of one signal, correlation determination would still result in values close to 1. The accessory high frequency content would appear as noise in correlation analysis. This effect is for example visible in the relation of $fuzzy_{su}$ with all soil temperatures (figure A.6).

Fuzzy logic. I found that the inclusion of fuzzy variables makes particular sense, when an enhancement of the input space's frequency content contributes to a better approximation of the spectral properties of the target time series. Fuzzy logic puts a conceptual element in the framework. Benefits and drawbacks are, however, not easy to distinguish. Fuzzy variables, as employed here, can be seen as depictions of basic properties of the earth's orbit that drive many natural processes in the most general way. This leads to them being a very robust estimator but for a very unspecific process. Regarding frequency content, it is, however, highly likely that the record of an ecological mechanism contains cyclicality that is connected to orbital dynamics. If this information is missing due to gaps it should be replaced by gap-filling.

Footprint variables. I-SIM modeling with Himmelmoor data improves when the relative contributions of the vegetated areas to the EC footprint are part of the input space. Footprint information thus contributes to the explanation of CH_4 flux variability at this site. One reason for this is the scale on which surface characteristics change in relation to the EC tower position. The EC system is located centrally on the 1450 x 910 m large extraction site, adjacent to two around 30 m wide vegetated strips stretching ~600 m to the west and ~700 m to the east. The anemometer height of 6 m was initially chosen due to these dimensions. From the footprint information contained in the data gathered with this setup it can be inferred that for certain wind directions, fluxes mainly related to the vegetated area are indeed distinguishable from signals from other surfaces. Hence, the way the measurement system was set up, suits the site characteristic scale of surface variability in a way that the acquired data is interpretable on surface class level. Besides, vegetated and bare peat areas are sharply contrasting regarding their CH_4 source strength. This feature is adding to their discriminability in the EC signal. The coupling between F_{CH4} and SC_{veg} is that close that multilinear models can explain CH_4 flux variability in Himmelmoor adequately.

6.1.3 Artificial neural network architecture optimization

A common practice to take a decision for the #HLN of MLPs or RBF networks is to use sizes other authors have used before (i. e. Dengel et al., 2013; Järvi et al., 2012; Menzer et al., 2015). Also the

spread value of RBF networks is usually set to a fixed value without further reasoning (i. e. Menzer et al., 2015). To my knowledge, no structured approach for the selection of architectural ANN properties is available in literature. The results presented in this thesis show that data-based decision-making for ANN architecture, improves model quality and gives more defendable predictions. With an accountable method for the setup of ANNs, they can emerge from their fate of being somehow mysterious black boxes to being based on data analysis and being specifically constructed for responses to individual datasets.

6.1.4 Empirical flux models

Multilayer perceptron. The MLP models were used for Himmelmoor gas flux gap-filling because they perform the most consistently throughout the comparison with the five different datasets. This notion is primarily based on the AIC values the diverse performance and generalization tests with tower view and surface class time series resulted in. In case of CO_2 flux modeling, the MLPs outperform all other models in all tests with respect to this statistic. Driving models fitted to Year 1 data with Year 2 inputs and comparing the results to Year 2 targets gives the most robust estimation of generalization capability (datasets C in tables 5.6 and 5.3). With respect to AIC the F_{CO2} MLP models converge to the target flux best in this particular comparison.

Multilayer perceptron vs. multilinear regression. Regarding the F_{CH4} models' AICs, the MLR undercuts the MLP only once. Nonetheless, it does so with respect to dataset C, which yields the most meaningful result within the scope of a search for the most general explanation of fluxes. However, given that the AIC difference between MLR and MLP is small, further inquiries still lead to the conclusion that the MLP performs best in approximating CH_4 exchange. Reasons to doubt the MLR include the comparably high BE and MAE and foremost the overadaption to high and low extrema in the target data. This property of MLRs leads to them extrapolating from the target data range, meaning that the MLR predictions partly lie outside the solution space they were inferred from. This behavior is also portrayed in the SCTS (see figures B.13, B.14, B.15 and B.16). Hence, the MLR gap-filling would add information to amplitude regions of the time series where no samples are available in the measurement data and where it is therefore unknown if physically reasonable fluxes exist. Especially the relatively high number of negative flux outputs from the MLR leads to some reluctance towards the credibility of this model type, as a process that would explain those fluxes is not known to the writer. It is, however, notable that a relatively simple linear model is in terms of explanatory power almost equal to an ANN that contains much more complexity. I attribute the circumstance that the MLP still provides a more likely approximation of the target data to the fact that architectural choices made during MLP design do impact the quality of its prediction. Within the I-SIM approach,

emphasis is put on the determination of the least complex ANN structure possible that still produces an appropriate representation of the target time series. Compared to a MLP that is not set up at the lower bound of necessary complexity, a MLR would most likely be superior. It can probably be stated in general, that hidden layer size optimization is inevitable when implementing ANNs for gap-filling. However, that MLR models are in turn the next best choice for F_{CH4} modeling is probably not true for all CH_4 flux datasets. In the cases presented here, the linear correlation between F_{CH4} and the footprint contributions of SC_{rew} and SC_{veg} is high. Inundation and the thereby established anaerobic soil conditions makes these areas prone to enhanced CH_4 emissions. Moreover, by the presence of vascular vegetation in SC_{veg}, an effective pathway for CH_4 release is established. With regard to their potential CH_4 source strength, a sharp contrast between neighboring surface classes and SC_{rew} or SC_{veg} respectively exists. When scale and distribution of clearly distinct surface classes are realized as they are in Himmelmoor, footprint information alone appears to explain a significant part of the flux variability depicted in the landscape-scale EC TVTS. Nearly linear coupling of footprint variables and observed flux (see figure A.1) may also have led to the rather good performance of linear models with the presented dataset.

Limits of the generalization test. The latter interpretation of MLR quality is based on results from a test that is assumed to provide the most robust estimation of generalizability. Within this check, models fitted to Year 1 data are evaluated by driving them with Year 2 inputs and comparing the results with measured fluxes from Year 2. This proceeding, however, only yields a valid estimation of model quality if gas flux differences between Year 1 and Year 2 can be attributed to interannual variations in meteorological conditions and do not document a fundamental change in ecosystem processes. If the workings responsible for CH_4 exchange underwent systematic alteration from Year 1 to Year 2, Year 1 models can not be expected to explain Year 2 data very well. The question, if modifications of the carbon gas balance are the result of progressing rewetting or depict interannual deviations of generally unchanged ecosystem processes cannot be ultimately resolved with the now available dataset. EC measurements in Himmelmoor are now recommenced so that the evaluation of longer-term shifts in carbon flux dynamics will be more robust in the future.

Performance of remaining models. Regarding the remaining tested model types, GRNNs show the highest correlation coefficients but are by far the most complex models resulting in very high AICs. Moreover, the generalization check with this model as well as with the RBF results in a overestimation of the target data. The BEs of the MLPs vary the least across all three datasets. The MDS

method stands out by the addition of high frequency signal components. It is, however, the only approach that does not considerably shift the scaling exponent from the measured to the gap-filled data. The quality of the gap-filled MDS time series depends on the program flow step the solution was found in. More large gaps in Year 2 F_{CH4} records resulted in more gaps being filled with model output of quality C (see figures A.7 to A.11). The longer gaps also lead to an increased number of search window sizes larger then ten days. A similar decline in quality from Year 1 to Year 2 is apparent in MDS F_{CO2} gap-filling (see figures A.12 to A.15), while the overall quality is better compared to F_{CH4} modeling. Some of the long Year 2 gaps are due to outages in the logging system and affect not only EC fluxes but also certain biomet records. In this context, the MDS method has advantages over the other model types. The routine can resort to lower quality modeling by employing the diurnal cycle steps if input variables are missing. None of the other tested methods can output data when input data is missing. The MDS method is useful from a pragmatical standpoint, when for example annual flux sums are intended. The lower data quality can be addressed in the calculation of annual sums by using distinct error estimates for class C obtained from MDS_{QC}.

Empirical vs. mechanistic models. Apart from one case, ANN predictions perform superior in all generalization checks of F_{CH4} and F_{CO2} models. In particular, MLPs result in the most consistent statistics. While EPReM results are more accurate when compared to I-SIM models, AIC differences to the MLP predictions are marginal. This fact illustrates the ability of this ANN type to also explain less entangled cause-effect relationships while reaching an equal level of confidence like a mechanistic approach that contains a priori knowledge about ecosystem functioning in much greater detail. I consider this outcome not to be a feature of MLPs in general, but rather attribute the comparably good performance to the data-driven dimensionality reduction included in I-SIM.

6.1.5 Mechanistic flux models

Half-hourly models. In general, modeling of CO_2 fluxes is more straightforward than the prediction of F_{CH4} since CO_2 production and fixation are the result of ecological processes that are well understood and mechanistic explanations (Lloyd and Taylor, 1994; Michaelis and Menten, 1913; Thornley, 1998) have proven to be applicable to estimate F_{CO2}. In case of the Rio Pipo dataset, CO_2 fluxes from a homogeneous surface could be modeled on tower view scale. Over homogeneous terrain, the mechanistical EPReM outcompetes the empirical I-SIM NEE predictions as described above.

Ensemble model parameters. Mechanistic models that included footprint surface class contributions as scaling terms were fitted to monthly ensembles of Himmelmoor F_{CO2} data. The resultant parameter time series allow for comparisons

with literature values and between SC_{rew} and SC_{dra}. R_{eco} is between two- and fourfold larger in areas with than without vegetation. The bare peat R_{eco} fluxes are in concordance with findings from Vanselow-Algan et al. (2015) who conducted chamber measurements on the vegetationless peat extraction site in Himmelmoor. The authors report mean annual CO_2 emissions from the mining site of 0.53 $\pm$ 0.05 µmol m^{-2} s^{-1} with summertime maxima between around 2 and 4 µmol m^{-2} s^{-1}. These values are well in range with the seasonal course of R_{eco} as it displays for the bare peat areas of SC_{dra} and SC_{rew} alike (figure 5.15). Vanselow-Algan et al. (2015) additionaly partitioned the NEE from different vegetation communities at the outer edge of Himmelmoor. These areas were restored three decades ago after being degraded by small-scale manual peat-cutting. Although the plants dominating the vegetated strips of the mining site were not examined by Vanselow-Algan et al. (2015), some of the species investigated by them also frequently occur in SC_{veg} being the subject of the present study.

The "purple moor grass" microform in Vanselow-Algan et al. (2015) for example is dominated by *Molinia caerulea*; *Betula pubescens* and *Eriophorum angustifolium* also occur. In summer, R_{eco} fluxes form this site were estimated to range above 10 µmol m^{-2} s^{-1}. Beyer and Höper (2015) report further results from a former north German peat extraction site that was rewetted 30 years prior to their chamber measurement campaign. R_{eco} estimates from these authors are available for a site dominated by *Molinia caerulea* (up to 7 µmol m^{-2} s^{-1} in August) and by *Eriophorum angustifolium* (up to 5 µmol m^{-2} s^{-1} in late July). A substantial portion of the SC_{veg} is covered by *Betula pubescens*, *Salix spp.*, *Eriophorum vaginatum*, *Eriophorum angustifolium*, *Typha latifolia*, *Molinia caerulea*, *Carex spp.*, *Juncus effusus* and *Calamagrostis pseudophragmites*. Further combined plant and root respiration measurements of the species found in SC_{veg} are not present in literature. Nevertheless, properties of plants from the same genera are known. Most reported fluxes, however, only refer to autotrophic respiration as they were determined on leaf scale. Measurements of *Betula spp.* dark respiration are given by Patankar et al. (2013) and Gu et al. (2008) (between 1 and 5 µmol m^{-2} s^{-1}). Patankar et al. (2013) also assessed autotrophic respiration of *Salix pulchra* (up to 2 µmol m^{-2} s^{-1}), *Eriophorum vaginatum* (up to 3 µmol m^{-2} s^{-1}), and *Carex bigelowi* (up to 1 µmol m^{-2} s^{-1}). Other *Carex* species are in the same range as shown by Körner (1982) (*Carex curvula* 1 µmol m^{-2} s^{-1}) and Murchie and Horton (1997) (*Carex flacca* 1.5 µmol m^{-2} s^{-1}). *Salix* summer dark respiration has as well been investigated by Kaipiainen (2009) with *Salix dasyclados* (between 0.8 and 1.2 µmol m^{-2} s^{-1}).

Regarding the photosynthesis parameters P_{max} and α in the second model term (section 4.7), more literature values are available for comparison. Chamber gas exchange studies on a single birch (*Betula pubescens*) in Himmelmoor during three summer months in 2014 by Lienau (2014) resulted in P_{max} values between 32 and 41 µmol m^{-2} s^{-1}). More P_{max}

estimates from the same tree species have been reported by Nygren and Kellomäki (1983) (4 to 17 µmol m^{-2} s^{-1}) and Hoogesteger and Karlsson (1992). In the latter study, PAR was limited to 800 µmol m^{-2} s^{-1}, P_{max} was assesed to be 8 µmol m^{-2} s^{-1}. Other evaluations of *Betula spp.* maximum photosynthesis range between 10 and 15 µmol m^{-2} s^{-1} (Gu et al., 2008; Patankar et al., 2013). With P_{max} values commonly around 25 but also above 30 µmol m^{-2} s^{-1} (Chen et al., 2010) *Typha latifolia* is photosynthically more active which is also the case for *Salix spp.* ranging between 16 and 29 µmol m^{-2} s^{-1} (Ögren, 1993). Lab-experiments from Vernay et al. (2016) provide P_{max} estimates of *Molinia caerulea* (7 to 15 µmol m^{-2} s^{-1}). For *Juncus effusus* only net photosynthesis values of 6 to 11 µmol m^{-2} s^{-1} (Mann and Wetzel, 1999) have been reported so far.

From the north German site investigated by Beyer and Höper (2015), comparably high P_{max} estimates are reported for *Molinia caerulea* that commonly range between 15 and 30 µmol m^{-2} s^{-1} but also reach values up to 60 µmol m^{-2} s^{-1} in June. The P_{max} parameters given by these authors for *Eriopohorum angustifolium* are also rather large (up to 70, often around 20 µmol m^{-2} s^{-1}). Initial quantum yield estimates of plants also common in SC_{veg} span amounts between 0.02 and 0.08 (Chen et al., 2010; Kaipiainen, 2009; Murchie and Horton, 1997; Nygren and Kellomäki, 1983; Vernay et al., 2016).

Parameter differences between SC_{rew} and SC_{dra} mainly emerge with respect to SC_{veg} and can be explained with deviations in hydrological site charachteristics. Inundation on SC_{rew} led to a hydrological connection of SC_{veg} with the bare peat areas. Hampered plant productivity due to a higher water table are expressed in lower peak values of P_{max} in SC_{rew}. R_{eco} of the vegetated areas is on the other hand elevated in comparison to SC_{dra}. An increased input of dissolved organic carbon from the bare peat areas to the vegetated strips might have promoted respiration.

R_{eco} is composed of autotrophic and heterotrophic respiration. While mosses have no roots, vascular plants are able to directly influence decomposition conditions in the rhizosphere by providing oxygen and root exudates that form an easily decomposable substrate for microbial respiration (Bhullar et al., 2014; Kerdchoechuen, 2005; Neue et al., 1996). Hence, apart from possibly elevated plant respiration, the presence of vascular plants fosters soil respiration as well. Moreover, the labile carbon provided by these plants can potentially be used by CH_4 producing microorganisms in case chemical conditions favor reduction of organic matter. Overall, peat mineralization can be enhanced by the presence of vascular plants despite their ability to fix more carbon dioxide with their high photosynthetic rates. Additionally, they potentially promote CH_4 production and release by providing a potential substrate for methanogens and, with their aerenchymae, an effective transport mechanism that includes the possibility to bypass methane-oxidizing zones within the soil profile or water column.

6.2 Trace gas flux balances

A carbon balance in the early years after ditch blocking is given by two consecutive years of GHG fluxes from the restored surfaces as also described in section 5.5. According to these results, rewetting does have a positive effect on the climate impact of Himmelmoor on the long run. In summer of Year 2, CO_2 sequestration of the rewetted areas even exceeds CO_2 release, turning them briefly from a C-source into a C-sink. However, the GHG flux sum of the SC_{rew} is increasingly dominated by CH_4 release from Year 1 to Year 2. On short time horizons, this can lead to these areas surpassing the CO_2eq emissions of the drained surfaces. Nevertheless, increasing CH_4 fluxes are not necessarily related to a general transition of the ecosystem into a state where methane production is principally more favorable. The data presented here only spans two years. Changes might as well be caused by interannual variations in meteorological conditions. While both years were relatively wet compared to the long-term average, Year 1 is distinguished by storm rainfall in early summer. Plant growth might have been inhibited by that.

The annual CO_2 emissions from the drained parts of 989 $\pm$ 13 g m^{-2} a^{-1} and 975 $\pm$ 13 g m^{-2} a^{-1} are higher but in the same range than previously inferred from chamber data by Vanselow-Algan et al. (2015) with 730 $\pm$ 67 g m^{-2} a^{-1}. In reference to a study by Drösler et al. (2008) that covers 11 drained peat extraction sites in Europe, Himmelmoor ranks as a high emitter, whereas larger sums, up to 1300 g $m^{-2}a^{-1}$, are also reported. Including the amount of carbon removed from the harvesting site by peat extraction (11402 $\pm$ 670 g m^{-2} a^{-1}), CO_2 emissions account for less than one tenth of the total carbon loss per year. This value from Vanselow-Algan et al. (2015) is, however, expressed as CO_2 and assumes the instant decomposition of the material after removal. Restored cut-over bogs commonly are CO_2 sinks when active peat extraction has been ceased for several decades (Beyer and Höper, 2015; Tuittila et al., 1999; Wilson et al., 2016).

The CH_4 flux sums of 13.3 $\pm$ 0.2 g m^{-2} a^{-1} and 18.5 $\pm$ 0.2 g m^{-2} a^{-1} from the rewetted surface class are confirmed by findings from Beyer and Höper (2015) who report CH_4 balances between 16.2 $\pm$ 2.2 g m^{-2} a^{-1} and 24.2 $\pm$ 5.0 g m^{-2} a^{-1} from inundated cut-over bogs in northern Germany. Wilson et al. (2016) report annual CH_4 emission sums of 12.0 $\pm$ 2.6 g m^{-2} a^{-1} from an Irish Atlantic blanket blog that had been rewetted 14 years prior to the investigation. Results from a boreal peat extraction site, 20 years after mining had been ceased, are given by Tuittila et al. (2000). Although only the growing season has been covered by these authors, the cumulative seasonal F_{CH4} of 1.27 g m^{-2} a^{-1} suggests that CH_4 release from boreal peatlands is much lower compared to temperate sites. This circumstance has also been noted by Tiemeyer et al. (2016), who furthermore conclude that IPCC estimates for CH_4 release from rewetted bogs, as

they are primarily based on data from boreal peatlands, are not representative for temperate regions. Actual CH_4 emissions from temperate bogs are most likely higher than anticipated by the IPCC.

6.3 Himmelmoor restoration

What are the chances of Himmelmoor to regress to a near-pristine state now that peat mining ceased? Can a colonization with bog forming plants be expected? First of all, with the type of rewetting measures that have been taken and that involve inundation of large, unvegetated, continuous sections of the former extraction site, the establishment of peat forming mosses will take many decades up to a few centuries (H. Joosten, personal communication, 2014), if it takes place at all. One major limitation for this process could be minerotrophic water introduced into the system through deep, the underlying aquifier penetrating ditches. These are the areas today vegetated by fen-type plants. Peat forming *Sphagnum spp.* mosses are adapted to nutrient-poor environments. For the purpose of re-establishing a degraded peatland's natural ecosystem functions, however, the initialization of peat accumulation is inevitable (Gaudig, 2002; Joosten, 1992; Pfadenhauer and Klötzli, 1996). In case of inundation, the creation of floating vegetation mats is the only possibility for sphagnum colonization (Pfadenhauer and Klötzli, 1996). Nevertheless, fast growing vascular plants can support peat moss growth by diminishing wave movement and offering adherence area (Sliva, 1997). Besides the need for a preferably calm water surface, another limiting factor for floating mat growth is the water CO_2 concentration (Gaudig, 2002; Lamers, 2001; Lütt, 1992; Paffen and Roelofs, 1991; Smolders et al., 2001). This level can be elevated by vascular plants providing oxygen and thereby fostering heterotrophic soil respiration. It thus seems conceivable that the *Sphagnum spp.* growth favoring effects outweigh the negative ramifications for bog development that the current plant cover implies. In sections of Himmelmoor with a non-industrial land use history, overgrowth of the grass tussocks, formerly dominating the area, by the bog-type *Sphagnum* species *magellanicum* and *papillosum* is in progress today (personal observation, 2016). The now prevailing plant species on the extraction site could therefore constitute an intermediate state that can potentially be overcome. Established peat accumulation by mosses could on the long run elevate the water level and eventually even decouple the bog's water regime from the groundwater.

Chapter 7

Synthesis

7.1 Conclusions

To summarize, the questions formulated in the beginning of this thesis are answered.

What is the best procedure for a reproducible selection of driving variables for accurate and robust empirical models (such as artificial neural networks, multilinear regressions or marginal distribution sampling methods) of gas flux time series?

I propose the I-SIM algorithm to tackle the tasks anticipated in the question posed above. Data-driven input selection resulted in physically reasonable choices for inputs that were used to drive CH_4 and CO_2 flux models. In settings when a comparison of I-SIM models with mechanistic flux predictions was feasible, I-SIM ANN models resulted in equally good approximations of the target data. I attribute this fact (1) to the input space dimensionality reduction and (2) to the ANN parameter optimization included in I-SIM. I therefore conclude that when applying empirical models to gap fill trace gas flux time series, a thorough and accountable method for the selection of input variables improves model predictions considerably. When ANNs are used in particular, efforts should be made to set them up in the least convoluted way a sufficient approximation of the target data allows for.

Is it possible to extract trace gas flux balances of individual surface classes from a complex EC flux times series measured over a heterogeneous peatland?

I found that if different microforms show contrasting gas flux features, the inclusion of their footprint contributions into flux models can improve their estimates and allow for more robust gap-filling of gas flux time series. Moreover, due to the specific setup (position and measurement height) of the EC system in Himmelmoor, fluxes could be attributed to distinct surface classes and individual annual time series were estimated. This subdivision of EC time series was possible owing to the scale (hundreds of meters) on which surface patterning exists in Himmelmoor. Additionally, a sharp contrast in gas flux dynamics between the different surface classes allowed for better discriminability between EC fluxes associated to individual surface types. However, to be able to estimate gas flux

time series of subsections within the EC footprint, rigorous filtering of the original time series is inevitable. Consequently, a considerable amount of measurement data is omitted and not assessed further.

Are the contrasting peatland management types also reflected in disparate carbon gas flux balances?

The three investigated land use types show distinct carbon gas flux features. Regarding Himmelmoor, CO_2 emissions decrease progressively after rewetting. The release of CH_4 increases after rewetting and within the present two year dataset also over time. On short timescales, the climate impact of elevated CH_4 emissions dominates over the effect of decreasing CO_2 release. Summer NEE of Rio Pipo resembles the values from the rewetted sites in Himmelmoor. Flux-partitioning reveals that while this net-flux is similar at both sites, photosynthesis is more effective in Himmelmoor. At the same time, ecosystem respiration is much higher in Himmelmoor, what leads to a summer NEE similar to Rio Pipo.

How does the climate change mitigation potential of a former peat-mining site develop during the early phase of rewetting.

It is conceivable that Himmelmoor can be transformed into a carbon accumulating peatland. However, this process will probably take centuries and will take place only when sustained management of the area is employed. The current rewetting measures that involve shallow inundation of large continuous areas are not sufficient to re-initialize the growth of bog-forming peat mosses. Although the current state of restoration does result in analogous summer NEE compared to Rio Pipo, ecosystem respiration at night and in winter is much higher than in the pristine system. Organic matter decomposition is promoted by the prevalent vascular plants. Pristine ecosystem respiration rather resembles values from the bare peat areas in Himmelmoor. A pristine bog carbon balance will not set in as long as vascular plants dominate.

7.2 Outlook

The GHGs that were considered within the scope of this thesis are the most important ones when it comes to the evaluation of the climate impact of peatland land use change. Other gases, like for example nitrous oxide, could be included in future studies in order to report an even more comprehensive GHG balance.

Additional small-scale gas fluxes measurements could be used to further substantiate the inferred flux time series on surface class level. Chamber measurements or ancillary EC towers with a lower measurement height would be an option to gain additional direct small-scale information.

In order to distinguish more clearly between interannual differences in gas flux balances and shifts in GHG emission dynamics related to land use change, more long-term data from Himmelmoor has to be analyzed. The EC system at this site is still running what actually provides the opportunity to follow up on the development of gas fluxes in the course of rewetting.

Acknowledgments

I want to express my heartfelt gratitude to Prof. Dr. Lars Kutzbach and Prof. Dr. Eva-Maria Pfeiffer for teaching, supervising and inspiring me during my studies and for their continued and kind support over the last years. I am especially grateful to Dipl.-Ing. Christian Wille, who was always willing to share his great technical wisdom and his comprehensive scientific insights with me in the most patient and friendly way.

None of the research projects carried out in Himmelmoor would have been possible without the fantastic, ongoing support of the peat plant operators. I want to espacially thank the manager of the peat plant, Klaus-Dieter Czerwonka, his wife Monika, their son Hans and Hans Müller for their always reliable, hands-on approach to the diverse challenges that come with the installation and operation of measurement equipment in hard to access areas. For supporting the fieldwork in Himmelmoor, I want to thank Peter Schreiber, Norman Rüggen, Ben Runkle, Olga Vybornova, Adrian Heger, Tim Pfau, Tom Huber, Ben Kreitner, Laure Hoeppli, Anastasia Tatarinova, Zoé Rehder and Oliver Kaufmann.

I am very grateful to Dra. Verónica Pancotto who had a key role in the logistical organization of our project in Argentina, shared her profound knowledge about the peatland ecosystems on Tierra del Fuego with me and was of vital importance during fieldwork. I am certain that without her insistent dedication to the project, no EC system would be collecting data on Tierra del Fuego today. She was moreover kindly hosting me in Centro Austral de Investigaciones Científicas (CADIC) in Ushuaia whose director Prof. Dr. Jorge Rabassa I also want to thank. I very much appreciate being able to work in Parque Nacional Tierra del Fuego and want to thank APN (Administracin de Parques Nacionales, Argentina) and Dr. Alejandro Valenzuela in particular. For supporting my fieldwork in Argentina, I want to express my gratitude to Ing. Rodolfo Iturraspe of UNTDF (Universidad Tierra del Fuego Antártida e Islas del Atlántico Sur), Sergio Jose Camargo of DGRH (Dirección General de Recursos Hídricos), Adrian Heger, Tom Huber, Prof. Dr. Christian Blodau, Wiebke Münchberger and Carla Bockermann. My work was partly supported through the DFG project KU 1418/6-1 ”Carbon, water and nutrient dynamics in vascuals vs. Sphagnum-dominated bog ecosystems in southern Patagonia – CANDYbog”.

References

Alberto, M. C. R., Wassmann, R., Buresh, R. J., Quilty, J. R., Correa, T. Q., Sandro, J. M. and Centeno, C. A. R.: 2014, Measuring methane flux from irrigated rice fields by eddy covariance method using open-path gas analyzer, *Field Crops Research* **160**, 12 – 21.

Alm, J., Shurpali, N. J., Minkkinen, K., Aro, L., Hytoenen, J., Laurila, T., Lohila, A., Maljanen, M., Martikainen, P. J. and Maekiranta, P.: 2007, Emission factors and their uncertainty for the exchange of CO_2, CH_4 and N_2O in Finnish managed peatlands, *Boreal Environment Research* **12**(2), 191 – 209.

Arroyo, M., Pliscoff, P., Mihoc, M. and Arroyo-Kalin, M.: 2005, The magellanic moorland, *in* L. Fraser and P. Keddy (eds), *The World's Largest Wetlands: Ecology and Conservation*, Cambridge University Press, Cambridge.

Auer, V.: 1965, *The Pleistocene of Fuego-Patagonia. Part IV: Bog Profiles*, number 1-3 in *Annales Academiae Scientiarum Fennicae: Geologica-geographica*, Suomalainen Tiedeakatemia, Helsinki.

Beale, M. H., Hagan, M. T. and Demuth, H. B.: 2015, *Neural Network Toolbox User's Guide*, The MathWorks, Inc., Natick.

Beer, J. and Blodau, C.: 2007, Transport and thermodynamics constrain belowground carbon turnover in a northern peatland, *Geochimica et Cosmochimica Acta* **71**(12), 2989 – 3002.

Beyer, C. and Höper, H.: 2015, Greenhouse gas exchange of rewetted bog peat extraction sites and a sphagnum cultivation site in northwest germany, *Biogeosciences* **12**(7), 2101–2117.

Bhattacharyya, P., Neogi, S., Roy, K., Dash, P., a.K. Nayak and Mohapatra, T.: 2014, Tropical low land rice ecosystem is a net carbon sink, *Agriculture, Ecosystems & Environment* **189**, 127 – 135.

Bhullar, G. S., Edwards, P. J. and Olde Venterink, H.: 2014, Influence of different plant species on methane emissions from soil in a restored swiss wetland, *PLOS ONE* **9**(2), 1–5.

Biester, H., Kilian, R., Franzen, C., Woda, C., Mangini, A. and Schöler, H.: 2002, Elevated mercury accumulation in a peat bog of the magellanic moorlands, chile (53°s)–an anthropogenic signal from the southern hemisphere, *Earth and Planetary Science Letters* **201**(3), 609–620.

Bishop, C. M.: 1995, Neural Networks for Pattern Recognition, *Journal of the American Statistical Association* **92**, 482.

Björck, S., Rundgren, M., Ljung, K., Unkel, I. and sa Wallin: 2012, Multi-proxy analyses of a peat bog on isla de los estados, easternmost tierra del fuego: a unique record of the variable southern hemisphere westerlies since the last deglaciation, *Quaternary Science Reviews* **42**, 1 – 14.

Blanco, D. E. and de la Balze, V. M.: 2004, *Los Turbales de la Patagonia. Bases para su inventario y la conservacin de su biodiversidad*, Wetlands International, Buenos Aires.

Brown, M. G., Humphreys, E. R., Moore, T. R., Roulet, N. T. and Lafleur, P. M.: 2014, Evidence for a nonmonotonic relationship between ecosystem-scale peatland methane emissions and water table depth, *Journal of Geophysical Research - Biogeosciences* **119**(5), 826 – 835.

Bubier, J. L.: 1995, The relationship of vegetation to methane emission and hydrochemical gradients in northern peatlands, *Journal of Ecology* **83**(3), 403–420.

Burba, G., Schmidt, A., Scott, R. L., Nakai, T., Kathilankal, J., Fratini, G., Hanson, C., Law, B., Mcdermitt, D. K., Eckles, R., Furtaw, M. and Velgersdyk, M.: 2012, Calculating CO_2 and H_2O eddy covariance fluxes from an enclosed gas analyzer using an instantaneous mixing ratio, *Global Change Biology* **18**(1), 385 – 399.

Campbell, D. I., Smith, J., Goodrich, J. P., Wall, A. M. and Schipper, L. A.: 2014, Year-round growing conditions explains large co2 sink strength in a new zealand raised peat bog, *Agricultural and Forest Meteorology* **192**, 59–68.

Chen, H., Zamorano, M. F. and Ivanoff, D.: 2010, Effect of flooding depth on growth, biomass, photosynthesis, and chlorophyll fluorescence of typha domingensis, *Wetlands* **30**(5), 957–965.

Chen, S., Cowan, C. F. and Grant, P. M.: 1991, Orthogonal least squares learning algorithm for radial basis function networks, *IEEE Transactions on neural networks* **2**(2), 302–309.

Conti, M. E., Finoia, M. G., Bocca, B., Mele, G., Alimonti, A. and Pino, A.: 2012, Atmospheric background trace elements deposition in tierra del fuego region (patagonia, argentina), using transplanted usnea barbata lichens, *Environmental Monitoring and Assessment* **184**(1), 527–538.

Couwenberg, J.: 2009a, *Emission factors for managed peat soils (organic soils, histosols) An analysis of IPCC default values*, Wetlands International, Ede.

Couwenberg, J.: 2009b, *Methane emissions from peat soils*, Wetlands International, Ede.

Couwenberg, J., Dommain, R. and Joosten, H.: 2010, Greenhouse gas fluxes from tropical peatlands in south-east Asia, *Global Change Biology* **16**(6), 1715 – 1732.

Czerwonka, K.-D. and Czerwonka, M.: 1985, *Das Himmelmoor - Dokumentationen, Berichte, Kommentare,*

Geschichten, self-published, Quickborn.

Dengel, S., Levy, P. E., Grace, J., Jones, S. K. and Skiba, U. M.: 2011, Methane emissions from sheep pasture, measured with an open-path eddy covariance system, *Global Change Biology* **17**, 3524 – 3533.

Dengel, S., Zona, D., Sachs, T., Aurela, M., Jammet, M., Parmentier, F. J. W., Oechel, W. and Vesala, T.: 2013, Testing the applicability of neural networks as a gap-filling method using CH_4 flux data from high latitude wetlands, *Biogeosciences* **10**(12), 8185 – 8200.

Deshmukh, C., Serça, D., Delon, C., Tardif, R., Demarty, M., Jarnot, C., Meyerfeld, Y., Chanudet, V., Guédant, P., Rode, W., Descloux, S. and Guérin, F.: 2014, Physical controls on CH_4 emissions from a newly flooded subtropical freshwater hydroelectric reservoir: Nam Theun 2, *Biogeosciences* **11**(15), 4251–4269.

Detto, M., Verfaillie, J., Anderson, F., Xu, L. and Baldocchi, D.: 2011, Comparing laser-based open- and closed-path gas analyzers to measure methane fluxes using the eddy covariance method, *Agricultural and Forest Meteorology* **151**(10), 1312 – 1324.

Draper, N. R. and Smith, H.: 1998, *Applied Regression Analysis*, 3rd edn, John Wiley and Sons, New York.

Drösler, M., Freibauer, A., Christensen, T. R. and Friborg, T.: 2008, Observations and status of peatland greenhouse gas emissions in europe, *The continental-scale greenhouse gas balance of Europe*, Springer, New York, pp. 243–261.

Falge, E., Baldocchi, D., Olson, R., Anthoni, P., Aubinet, M., Bernhofer, C., Burba, G., Ceulemans, R., Clement, R., Dolman, H., Granier, A., Gross, P., Grünwald, T., Hollinger, D., Jensen, N.-O., Katul, G., Keronen, P., Kowalski, A., Lai, C. T., Law, B. E., Meyers, T., Moncrieff, J., Moors, E., Munger, J., Pilegaard, K., Rannik, Ü., Rebmann, C., Suyker, A., Tenhunen, J., Tu, K., Verma, S., Vesala, T., Wilson, K. and Wofsy, S.: 2001, Gap filling strategies for defensible annual sums of net ecosystem exchange, *Agricultural and Forest Meteorology* **107**(1), 43 – 69.

Fan, S. M., Wofsy, S. C., Bakwin, P. S., Jacob, D. J., Anderson, S. M., Kebabian, P. L., McManus, J. B., Kolb, C. E. and Fitzjarrald, D. R.: 1992, Micrometeorological measurements of ch4 and co2 exchange between the atmosphere and subarctic tundra, *Journal of Geophysical Research: Atmospheres* **97**(D15), 16627 – 16643.

Finkelstein, P. L. and Sims, P. F.: 2001, Sampling error in eddy correlation flux measurements, *Journal of Geophysical Research* **106**(D4), 3503.

Forbrich, I., Kutzbach, L., Wille, C., Becker, T., Wu, J. and Wilmking, M.: 2011, Cross-evaluation of measurements of peatland methane emissions on microform and ecosystem scales using high-resolution landcover classification and source weight modelling,

Agricultural and Forest Meteorology **151**(7), 864 – 874.

Fratini, G., Ibrom, A., Arriga, N., Burba, G. and Papale, D.: 2012, Relative humidity effects on water vapour fluxes measured with closed-path eddy-covariance systems with short sampling lines, *Agricultural and Forest Meteorology* **165**, 53 – 63.

Friborg, T. and Christensen, T.: 2000, Trace gas exchange in a high-arctic valley 2 . Landscape CH 4 fluxes measured and modeled using eddy correlation have measurements, *Global Biogeochemical Cycles* **14**(3), 715 – 723.

Fritz, C., Pancotto, V. A., Elzenga, J. T. M., Visser, E. J. W., Grootjans, A. P., Pol, A., Iturraspe, R., Roelofs, J. G. M. and Smolders, A. J. P.: 2011, Zero methane emission bogs: extreme rhizosphere oxygenation by cushion plants in patagonia, *New Phytologist* **190**(2), 398–408.

Garratt, J.: 1994, *The Atmospheric Boundary Layer*, Cambridge Atmospheric and Space Science Series, Cambridge University Press, Cambridge.

Garson, G. D.: 1991, Interpreting neural-network connection weights, *AI Expert* **6**(4), 46 – 51.

Gash, J. H. C. and Culf, a. D.: 1996, Applying a linear detrend to eddy correlation data in realtime, *Boundary-Layer Meteorology* **79**(3), 301 – 306.

Gaudig, G.: 2002, The research project: "peat mosses (sphagnum) as a renewable resource: establishment of peat mosses - optimising growth conditions, *Telma* **32**, 227 – 242.

Glaser, P. H.: 2004, Surface deformations as indicators of deep ebullition fluxes in a large northern peatland, *Global Biogeochemical Cycles* **18**(1), n/a – n/a.

Godoy, R., Paulino, L., Oyarzún, C. and Boeckx, P.: 2003, Atmospheric n deposition in central and southern chile. an overview, *Gayana Bot ánica* **60**(1), 47–53.

Goodrich, J., Campbell, D., Clearwater, M., Rutledge, S. and Schipper, L.: 2015, High vapor pressure deficit constrains gpp and the light response of nee at a southern hemisphere bog, *Agricultural and Forest Meteorology* **203**, 54–63.

Goodrich, J., Campbell, D., Roulet, N., Clearwater, M. and Schipper, L.: 2015, Overriding control of methane flux temporal variability by water table dynamics in a southern hemisphere, raised bog, *Journal of Geophysical Research: Biogeosciences* **120**(5), 819 – 831.

Goodrich, J. P., Varner, R. K., Frolking, S., Duncan, B. N. and Crill, P. M.: 2011, High-frequency measurements of methane ebullition over a growing season at a temperate peatland site, *Geophysical Research Letters* **38**(7).

Grootjans, A., Iturraspe, R., Fritz, C., Moen, A., Joosten, H. et al.: 2014, Mires and mire types of peninsula mitre, tierra del fuego, argentina, *Mires and peat* **14**, 1–20.

Grootjans, A., Iturraspe, R., Lanting, A., Fritz, C., Joosten, H. et al.: 2010, Eco-

hydrological features of some contrasting mires in tierra del fuego, argentina, *Mires and peat* **6**(01), 1–15.

Grube, A., Fuest, T. and Menzel, P.: 2010, Geology of the Himmelmoor(bog) near Quickborn, *Telma* **40**, 19 – 32.

Gu, M., Robbins, J. A., Rom, C. R. and Choi, H. S.: 2008, Photosynthesis of birch genotypes (Betula L.) under varied irradiance and CO_2 concentration, *HortScience* **43**(2), 314–319.

Hahn-Schöfl, M., Zak, D., Minke, M., Gelbrecht, J., Augustin, J. and Freibauer, a.: 2010, Organic sediment formed during inundation of a degraded fen grassland emits large fluxes of CH_4 and CO_2, *Biogeosciences Discussions* **7**(6), 9273 – 9303.

Hammond, R.: 1981, *The peatlands of Ireland*, An Foras Taluntais, Dublin.

Hanis, K. L., Tenuta, M., Amiro, B. D. and Papakyriakou, T. N.: 2013, Seasonal dynamics of methane emissions from a subarctic fen in the Hudson Bay Lowlands, *Biogeosciences* **10**(7), 4465 – 4479.

Hashem, S.: 1997, Optimal Linear Combinations of Neural Networks., *Neural networks : the official journal of the International Neural Network Society* **10**(4), 599 – 614.

Hatala, J. a., Detto, M. and Baldocchi, D. D.: 2012, Gross ecosystem photosynthesis causes a diurnal pattern in methane emission from rice, *Geophysical Research Letters* **39**(6), 1 – 5.

Haykin, S.: 1999, *Neural Networks: a comprehensive foundation*, Prentice Hall, Upper Saddle River.

Heusser, C.: 1993, Late-glacial of southern south america, *Quaternary Science Reviews* **12**(5), 345 – 350.

Heusser, C.: 1995, Palaeoecology of a donatia-astelia cushion bog, magellanic moorland-subantarctic evergreen forest transition, southern tierra del fuego, argentina, *Review of Palaeobotany and Palynology* **89**(3), 429 – 440.

Hollinger, D. Y., Goltz, S. M., Davidson, E. a., Lee, J. T., Tu, K. and Valentine, H. T.: 1999, Seasonal patterns and environmental control of carbon dioxide and water vapour exchange in an ecotonal boreal forest, *Global Change Biology* **5**(8), 891 – 902.

Hommeltenberg, J., Mauder, M., Drösler, M., Heidbach, K., Werle, P. and Schmid, H. P.: 2014, Ecosystem scale methane fluxes in a natural temperate bog-pine forest in southern germany, *Agricultural and Forest Meteorology* **198**, 273 – 284.

Hoogesteger, J. and Karlsson, P.: 1992, Effects of defoliation on radial stem growth and photosynthesis in the mountain birch (betula pubescens ssp. tortuosa), *Functional Ecology* pp. 317–323.

Horst, T. W. and Lenschow, D. H.: 2009, Attenuation of scalar fluxes measured with spatially-displaced sensors, *Boundary-Layer Meteorology* **130**, 275 – 300.

Hsieh, C.-I., Katul, G. and wen Chi, T.: 2000, An approximate analytical model for footprint estimation of scalar fluxes in thermally stratified atmospheric flows, *Advances in Water Resources* **23**(7), 765 – 772.

Hunter, A., Kennedy, L., Henry, J. and Ferguson, I.: 2000, Application of neural networks and sensitivity analysis to improved prediction of trauma survival, *Computer Methods and Programs in Biomedicine* **62**(1), 11 – 19.

Ibrom, A., Dellwik, E., Flyvbjerg, H., Jensen, N. O. and Pilegaard, K.: 2007, Strong low-pass filtering effects on water vapour flux measurements with closed-path eddy correlation systems, *Agricultural and Forest Meteorology* **147**(3-4), 140 – 156.

Iturraspe, R.: 2010, *Las turberas de Tierra del Fuego y el Cambio Climático global*, Fundación Humedales/Wetlands International, Buenos Aires.

Iturraspe, R.: 2012, Spatial analysis and description of eastern peatlands of tierra del fuego, argentina, *in* T. Lindholm, R. Heikkilä and S. Ympäristökeskus (eds), *Mires from Pole to Pole*, Finnish Environment Inst., Helsinki, pp. 385–389.

Jackowicz-Korczyski, M., Christensen, T. R., Bäckstrand, K., Crill, P., Friborg, T., Mastepanov, M. and Ström, L.: 2010, Annual cycle of methane emission from a subarctic peatland, *Journal of Geophysical Research* **115**(G2), 1 – 10.

Järvi, L., Nordbo, A., Junninen, H., Riikonen, A., Moilanen, J., Nikinmaa, E. and Vesala, T.: 2012, Seasonal and annual variation of carbon dioxide surface fluxes in Helsinki, Finland, in 20062010, *Atmospheric Chemistry and Physics* **12**(18), 8475 – 8489.

Jha, C. S., Rodda, S. R., Thumaty, K. C., Raha, a. K. and Dadhwal, V. K.: 2014, Eddy covariance based methane flux in Sundarbans mangroves, India, *Journal of Earth System Science* **123**(5), 1089 – 1096.

Joosten, H.: 1992, Bog regeneration in the netherlands: A review, *in* O. M. Bragg (ed.), *Peatland Ecosystems and Man: An Impact Assessment*, Department of Biological Sciences, University of Dundee, Dundee.

Kaimal, J. C., Wyngaard, J. C., Izumi, Y. and Coté, O. R.: 1972, Spectral characteristics of surface-layer turbulence, *Quarterly Journal of the Royal Meteorological Society* **98**(417), 563 – 589.

Kaimal, J. and Finnigan, J.: 1994, *Atmospheric Boundary Layer Flows: Their structure and measurements*, Oxford University Press, Oxford.

Kaipiainen, E. L.: 2009, Parameters of photosynthesis light curve in salix dasyclados and their changes during the growth season, *Russian Journal of Plant Physiology* **56**(4), 445–453.

Kerdchoechuen, O.: 2005, Methane emission in four rice varieties as related to sugars and organic acids of roots and root exudates and biomass

yield, *Agriculture, Ecosystems & Environment* **108**(2), 155 – 163.

Kettunen, A., Kaitala, V., Alm, J., Silvola, J., Nykänen, H. and Martikainen, P. J.: 1996, Cross-correlation analysis of the dynamics of methane emissions from a boreal peatland, *Global Biogeochemical Cycles* **10**(3), 457–471.

Kleinebecker, T., Hölzel, N. and Vogel, A.: 2007, Gradients of continentality and moisture in south patagonian ombrotrophic peatland vegetation, *Folia Geobotanica* **42**(4), 363–382.

Kleinebecker, T., Hölzel, N. and Vogel, A.: 2008, South patagonian ombrotrophic bog vegetation reflects biogeochemical gradients at the landscape level, *Journal of Vegetation Science* **19**(2), 151–160.

Kljun, N., Calanca, P., Rotach, M. W. and Schmid, H. P.: 2004, A simple parameterisation for flux footprint predictions, *Boundary-Layer Meteorology* **112**(3), 503 – 523.

Knox, S. H., Sturtevant, C., Matthes, J. H., Koteen, L., Verfaillie, J. and Baldocchi, D.: 2015, Agricultural peatland restoration: effects of land-use change on greenhouse gas (CO_2 and CH_4) fluxes in the Sacramento-San Joaquin Delta, *Global Change Biology* **21**(2), 750 – 765.

Kordowski, K. and Kuttler, W.: 2010, Carbon dioxide fluxes over an urban park area, *Atmospheric Environment* **44**(23), 2722 – 2730.

Kormann, R. and Meixner, F. X.: 2001, An analytical footprint model for non-neutral stratification, *Boundary-Layer Meteorology* **99**(2), 207 – 224.

Körner, C.: 1982, CO_2 exchange in the alpine sedge Carex curvula as influenced by canopy structure, light and temperature, *Oecologia* **53**(1), 98–104.

Kroon, P. S., Schrier-Uijl, a. P., Hensen, a., Veenendaal, E. M. and Jonker, H. J. J.: 2010, Annual balances of CH4 and N2O from a managed fen meadow using eddy covariance flux measurements, *European Journal of Soil Science* **61**(5), 773 – 784.

Lai, D. Y. F.: 2009, Methane Dynamics in Northern Peatlands: A Review, *Pedosphere* **19**(4), 409 – 421.

Lamers, L.: 2001, *Tackling Biochemical Questions in Peatlands*, PhD thesis, Katholieke Universiteit Nijmegen.

Lee, X., Massman, W. and Law, B.: 2004, *Handbook of Micrometeorology: A Guide for Surface Flux Measurement and Analysis*, Kluwer Academic Publishers, Dordrecht.

Lehmann, J. R. K., Münchberger, W., Knoth, C., Blodau, C., Nieberding, F., Prinz, T., Pancotto, V. A. and Kleinebecker, T.: 2016, High-resolution classification of south patagonian peat bog microforms reveals potential gaps in up-scaled ch4 fluxes by use of unmanned aerial system (uas) and cir imagery, *Remote Sensing* **8**(3), 173.

Lienau, D.: 2014, *Untersuchung der diurnalen variabilität der photosyntheseraten der moorbirke im himmelmoor*, Master's thesis, Universität Hamburg, Hamburg.

Likas, A., Vlassis, N. and J. Verbeek, J.: 2003, The global k-means clustering algorithm, *Pattern Recognition* **36**(2), 451 – 461.

Lloyd, J. and Taylor, J.: 1994, On the temperature dependence of soil respiration, *Functional ecology* pp. 315–323.

Lomb, N.: 1976, Least-squares frequency analysis of unequally spaced data, *Astrophysics and Space Science* **39**(2), 447–462.

Long, K., Flanagan, L. B. and Cai, T.: 2010, Diurnal and seasonal variation in methane emissions in a northern Canadian peatland measured by eddy covariance, *Global Change Biology* **16**, 2420 – 2435.

Lütt, S.: 1992, *Produktionsbiologische Untersuchungen zur Sukzession der Torfstichvegetation in Schleswig-Holstein*, Arbeitsgemeinschaft Geobotanik in Schleswig-Holstein und Hamburg, Kiel.

Mahecha, M. D., Reichstein, M., Carvalhais, N., Lasslop, G., Lange, H., Seneviratne, S. I., Vargas, R., Ammann, C., Arain, M. A., Cescatti, A., Janssens, I. A., Migliavacca, M., Montagnani, L. and Richardson, A. D.: 2010, Global convergence in the temperature sensitivity of respiration at ecosystem level, *Science* **329**(5993), 838–840.

Mann, C. J. and Wetzel, R. G.: 1999, Photosynthesis and stomatal conductance of Juncus effusus in a temperate wetland ecosystem, *Aquatic Botany* **63**(2), 127–144.

Mark, A. F., Johnson, P. N., Dickinson, K. J. M. and McGlone, M. S.: 1995, Southern hemisphere patterned mires, with emphasis on southern new zealand, *Journal of the Royal Society of New Zealand* **25**(1), 23–54.

Mauder, M. and Foken, T.: 2004, Documentation and instruction manual of the eddy covariance software package TK2, Univ, *Arbeitsergebnisse, Universität Bayreuth, Abt. Mikrometeorologie* **26**, 45.

Mauquoy, D. and Bennett, K. D.: 2006, Peatlands in tierra del fuego, *in* H. Rydin and J. K. Jeglum (eds), *The biology of peatlands*, Oxford University Press, Oxford.

McDermitt, D., Burba, G., Xu, L., Anderson, T., Komissarov, a., Riensche, B., Schedlbauer, J., Starr, G., Zona, D., Oechel, W., Oberbauer, S. and Hastings, S.: 2011, A new low-power, open-path instrument for measuring methane flux by eddy covariance, *Applied Physics B: Lasers and Optics* **102**(2), 391 – 405.

Menzer, O., Meiring, W., Kyriakidis, P. C. and McFadden, J. P.: 2015, Annual sums of carbon dioxide exchange over a heterogeneous urban landscape through machine learning based gap-filling, *Atmospheric Environment* **101**, 312 – 327.

Michaelis, L. and Menten, M. L.: 1913, Die kinetik der invertinwirkung, *Biochemische Zeitschrift* **49**(333-369), 352.

Mikhaylov, O. A., Miglovets, M. N. and Zagirova, S. V.: 2015, Vertical methane fluxes in mesooligotrophic boreal peatland in European Northeast Russia, *Contemporary Problems of Ecology* **8**(3), 368 – 375.

Moen, A., Couwenberg, J. and Joosten, H.: 2005, Comments on the regional variation and mires in Tierra del Fuego-a comparison with Fennoscandia, *International Mire Conservation Group Newsletter* **4**, 11–13.

Moffat, A. M.: 2012, *A new methodology to interpret high resolution measurements of net carbon fluxes between terrestrial ecosystems and the atmosphere*, PhD thesis, Friedrich-Schiller-Universität Jena.

Moffat, A. M., Papale, D., Reichstein, M., Hollinger, D. Y., Richardson, A. D., Barr, A. G., Beckstein, C., Braswell, B. H., Churkina, G., Desai, A. R., Falge, E., Gove, J. H., Heimann, M., Hui, D., Jarvis, A. J., Kattge, J., Noormets, A. and Stauch, V. J.: 2007, Comprehensive comparison of gap-filling techniques for eddy covariance net carbon fluxes, *Agricultural and Forest Meteorology* **147**(3-4), 209 – 232.

Moncrieff, J., Clement, R., Finnigan, J. and Meyers, T.: 2004, Averaging, detrending, and filtering of eddy covariance time series, *Handbook of Micrometeorology* pp. 7 – 31.

Moncrieff, J., Valentini, R., Greco, S., Guenther, S. and Ciccioli, P.: 1997, Trace gas exchange over terrestrial ecosystems: methods and perspectives in micrometeorology, *Journal of Experimental Botany* **48**(5), 1133 – 1142.

Moore, D. and de Goodall, R.: 1983, *Flora of Tierra Del Fuego*, A. Nelson, Oswestry.

Murchie, E. H. and Horton, P.: 1997, Acclimation of photosynthesis to irradiance and spectral quality in british plant species: chlorophyll content, photosynthetic capacity and habitat preference, *Plant, Cell and Environment* **20**(4), 438–448.

Myhre, G., Shindell, D., Bron, F.-M., Collins, W., Fuglestvedt, J., Huang, J., Koch, D., Lamarque, J.-F., Lee, D., Mendoza, B., Nakajima, T., Robock, A., Stephens, G., Takemura, T. and Zhang, H.: 2013, Anthropogenic and natural radiative forcing, *in* T. Stocker, D. Qin, G.-K. Plattner, M. Tignor, S. Allen, J. Boschung, A. Nauels, Y. Xia, V. Bex and P. Midgley (eds), *Climate Change 2013: The Physical Science Basis. Contribution of Working Group I to the Fifth Assessment Report of the Intergovernmental Panel on Climate Change*, Cambridge University Press, Cambridge.

Naftaly, U., Intrator, N. and Horn, D.: 1997, Optimal ensemble averaging of neural networks, *Network: Computation in Neural Systems* **8**(3), 283 – 296.

Nakai, T., Van der Molen, M., Gash, J. and Kodama, Y.: 2006, Correction of sonic anemometer angle of attack errors, *Agricultural and Forest Meteorology* **136**(1), 19–30.

Neue, H., Wassmann, R., Lantin, R., Alberto, M. C., Aduna, J. and Javellana, A.: 1996, Factors affecting methane emission from rice fields, *Atmospheric Environment* **30**(10), 1751–1754.

Nygren, M. and Kellomäki, S.: 1983, Effect of shading on leaf structure and photosynthesis in young birches, Betula pendula Roth. and B. pubescens Ehrh., *Forest Ecology and Management* **7**(2), 119–132.

Ögren, E.: 1993, Convexity of the Photosynthetic Light-Response Curve in Relation to Intensity and Direction of Light during Growth., *Plant physiology* **101**(3), 1013–1019.

Olden, D. A. and Jackson, J. D. Y.: 2002, Illuminating the ”black box”: a randomization approach for understanding variable contributions in artificial neuronal networks., *Ecological Modelling* **154**, 135 – 150.

Paffen, B. and Roelofs, J.: 1991, Impact of carbon dioxide and ammonium on the growth of submerged sphagnum cuspidatum, *Aquatic Botany* **40**(1), 61 – 71.

Papale, D. and Valentini, R.: 2003, A new assessment of European forests carbon exchanges by eddy fluxes and artificial neural network spatialization, *Global Change Biology* **9**(4), 525 – 535.

Parish, F., Sirin, A., Charman, D., Joosten, H., Minaeva, T. and Silvius, M.: 2008, *Assessment on peatlands, biodiversity and climate change*, Global Environment Centre, Kuala Lumpur.

Parmentier, F. J. W., Van Huissteden, J., Van Der Molen, M. K., Schaepman-Strub, G., Karsanaev, S. a., Maximov, T. C. and Dolman, a. J.: 2011, Spatial and temporal dynamics in eddy covariance observations of methane fluxes at a tundra site in northeastern Siberia, *Journal of Geophysical Research: Biogeosciences* **116**(3), 1 – 14.

Patankar, R., Mortazavi, B., Oberbauer, S. F. and Starr, G.: 2013, Diurnal patterns of gas-exchange and metabolic pools in tundra plants during three phases of the arctic growing season, *Ecology and Evolution* **3**(2), 375–388.

Peltola, O., Hensen, A., Helfter, C., Belelli Marchesini, L., Bosveld, F. C., van den Bulk, W. C. M., Elbers, J. A., Haapanala, S., Holst, J., Laurila, T., Lindroth, A., Nemitz, E., Röckmann, T., Vermeulen, A. T. and Mammarella, I.: 2014, Evaluating the performance of commonly used gas analysers for methane eddy covariance flux measurements: the InGOS intercomparison field experiment, *Biogeosciences* **11**(12), 3163 – 3186.

Peltola, O., Mammarella, I., Haapanala, S., Burba, G. and Vesala, T.: 2013, Field intercomparison of four methane gas analyzers suitable for eddy covariance flux measurements, *Biogeosciences* **10**(6), 3749 – 3765.

Perrone, M. P. and Cooper, L. N.: 1993, When networks disagree: ensemble methods for hybrid neural network, *in* R. J. Mammone (ed.), *Neural Networks for Speech and Image Process-*

ing, Chapman Hall, London, pp. 126 – 142.

Pfadenhauer, J. and Klötzli, F.: 1996, Restoration experiments in middle european wet terrestrial ecosystems: An overview, *Vegetatio* **126**(1), 101–115.

Pfeiffer, E.-M.: 1997, Methanfreisetzung aus hydromorphen Böden verschiedener naturnaher und genutzter Feuchtgebiete (Marsch, Moor, Tundra, Reisanbau)., *Hamburger Bodenkundliche Arbeiten* **37**.

Pisano, E.: 1977, Fitogeografía de Fuego-Patagonia chilena. I.- Comunidades vegetales entre las latitudes 52 y 56° S, *Anales del Instituto de la Patagonia*.

Pisano, E.: 1983, Magellanic tundra complex, *Ecosystems of the World, 4B (Regional Studies): Mires, swamp, bog, fen and moor.*, Elsevier, Amsterdam, pp. 295 – 329.

Ponce, J. F., Borromei, A. M., Menounos, B. and Rabassa, J.: 2016, Late-holocene and little ice age palaeoenvironmental change inferred from pollen analysis, isla de los estados, argentina, *Quaternary International* .

Ponce, J. F. and Fernández, M.: 2014, *Climatic and environmental history of Isla de los Estados, Argentina*, Springer, New York.

Pypker, T. G., Moore, P. a., Waddington, J. M., Hribljan, J. a. and Chimner, R. C.: 2013, Shifting environmental controls on CH4 fluxes in a sub-boreal peatland, *Biogeosciences* **10**(12), 7971 – 7981.

Rabassa, J., Coronato, A., Bujalesky, G., Salemme, M., Roig, C., Meglioli, A., Heusser, C., Gordillo, S., Roig, F., Borromei, A. and Quattrocchio, M.: 2000, Quaternary of tierra del fuego, southernmost south america: an updated review, *Quaternary International* **6871**, 217 – 240.

Rabassa, J., Coronato, A. and Heusser, C.: 1989, Peat-bog accumulation rate in the andes of tierra del fuego and patagonia (argentina and chile) during the last 43.000 years, *Pirineos* **133**, 113–122.

Rabassa, J., Coronato, A., Heusser, C., Juent, F. R., Borromei, A., Roig, C. and Quattrocchio, M.: 2006, Chapter 6 the peatlands of argentine tierra del fuego as a source for paleoclimatic and paleoenvironmental information, *in* A. M. C. I.P. Martini and W. Chesworth (eds), *PeatlandsEvolution and Records of Environmental and Climate Changes*, Vol. 9 of *Developments in Earth Surface Processes*, Elsevier, pp. 129 – 144.

Rabassa, J., Coronato, A. and Roig, C.: 1996, The peat bogs of tierra del fuego, argentina, *in* E. Lappalainen (ed.), *Global peat resources*, International Peat Society, Jyväskylä, pp. 261–266.

Reichstein, M., Falge, E., Baldocchi, D., Papale, D., Aubinet, M., Berbigier, P., Bernhofer, C., Buchmann, N., Gilmanov, T., Granier, A., Grunwald, T., Havrankova, K., Ilvesniemi, H., Janous, D., Knohl, A., Laurila, T., Lohila, A., Loustau, D., Matteucci, G., Meyers, T.,

Miglietta, F., Ourcival, J.-M., Pumpanen, J., Rambal, S., Rotenberg, E., Sanz, M., Tenhunen, J., Seufert, G., Vaccari, F., Vesala, T., Yakir, D. and Valentini, R.: 2005, On the separation of net ecosystem exchange into assimilation and ecosystem respiration: review and improved algorithm, *Global Change Biology* **11**(9), 1424 – 1439.

Richardson, A. D., Mahecha, M. D., Falge, E., Kattge, J., Moffat, A. M., Papale, D., Reichstein, M., Stauch, V. J., Braswell, B. H., Churkina, G., Kruijt, B. and Hollinger, D. Y.: 2008, Statistical properties of random {CO2} flux measurement uncertainty inferred from model residuals, *Agricultural and Forest Meteorology* **148**(1), 38 – 50.

Rinne, J., Riutta, T., Pihlatie, M., Aurela, M., Haapanala, S., Tuovinen, J. P., Tuittila, E. S. and Vesala, T.: 2007, Annual cycle of methane emission from a boreal fen measured by the eddy covariance technique, *Tellus, Series B: Chemical and Physical Meteorology* **59**(3), 449 – 457.

Roig, C., Roig, F., Collado, L., Coronato, A., Martnez Carretero, E. and Barrios, V.: 2001, *Inventario de los turbales de la zona centro de la provincia de Tierra del Fuego. Informe final*, CFI-Subsecretara de Recursos Naturales, provincia de Tierra del Fuego, Antrtida e Islas del Atlntico Sur, Ushuaia.

Roig, F. A.: 1998, La vegetación de la patagonia, *in* M. Correa (ed.), *Flora Patagnica. Parte I*, Instituto Nacional de Tecnología Agropecuaria, Buenos Aires, pp. 48–166.

Roivainen, H.: 1954, Studien über die moore feuerlands, *Annales Botanici Societatis Zooligicae Botanicae Fennicae'Vanamo'(* **28**(2).

Runkle, B. R. K., Sachs, T., Wille, C., Pfeiffer, E.-M. and Kutzbach, L.: 2013, Bulk partitioning the growing season net ecosystem exchange of co_2 in siberian tundra reveals the seasonality of its carbon sequestration strength, *Biogeosciences* **10**(3), 1337–1349.

Saarnio, S., Winiwarter, W. and Leitão, J.: 2009, Methane release from wetlands and watercourses in Europe, *Atmospheric Environment* **43**(7), 1421 – 1429.

Sachs, T., Giebels, M., Boike, J. and Kutzbach, L.: 2008, Environmental controls on CH4 emission from polygonal tundra on the microsite scale in the Lena river delta, Siberia, *Global Change Biology* **16**(11), 3096 – 3110.

Sarle, W. S.: 1994, Neural Networks and Statistical Models, *Proceedings of the Nineteenth Annual SAS Users Group International Conference, April, 1994*, pp. 1 – 13.

Sarle, W. S.: 1997, Neural Network FAQ, periodic posting to the Usenet newsgroup comp.ai.neural-nets.
URL: *ftp://ftp.sas.com/pub/neural/FAQ.html*

Scargle, J. D.: 1982, Studies in astronomical time series analysis. II - Statistical aspects of spectral analysis of unevenly spaced data, *Astrophysical Journal* **263**, 835–853.

Schmidt, A., Wrzesinsky, T. and Klemm, O.: 2008, Gap Filling and Qual-

ity Assessment of CO2 and Water Vapour Fluxes above an Urban Area with Radial Basis Function Neural Networks, *Boundary-Layer Meteorology* **126**(3), 389 – 413.

Schrier-Uijl, A. P., Kroon, P. S., Leffelaar, P. a., van Huissteden, J. C., Berendse, F. and Veenendaal, E. M.: 2010, Methane emissions in two drained peat agro-ecosystems with high and low agricultural intensity, *Plant and Soil* **329**(1), 509 – 520.

Shoemaker, W. B., Anderson, F., Barr, J. G., Graham, S. L. and Botkin, D. B.: 2015, Carbon exchange between the atmosphere and subtropical forested cypress and pine wetlands, *Biogeosciences* **12**(8), 2285 – 2300.

Sliva, J.: 1997, *Renaturierung von industriell abgetorften Hochmooren am Beispiel der Kendlmühlilzen*, PhD thesis, Institut für Landespflege und Botanik München.

Smolders, A. J. P., Tomassen, H. B. M., Pijnappel, H. W., Lamers, L. P. M. and Roelofs, J. G. M.: 2001, Substrate-derived co2 is important in the development of sphagnum spp., *New Phytologist* **152**(2), 325 – 332.

Specht, D. F.: 1991, A general regression neural network, *Neural Networks, IEEE Transactions on* **2**(6), 568 – 576.

Strack, M., Kellner, E. and Waddington, J.: 2005, Dynamics of biogenic gas bubbles in peat and their effects on peatland biogeochemistry, *Global Biogeochemical Cycles* **19**(1).

Stull, R.: 1988, *An Introduction to Boundary Layer Meteorology*, Kluwer Academic Publishers, Dordrecht.

Suyker, A. E., Verma, S. B., Clement, R. J. and Billesbach, D. P.: 1996, Methane flux in a boreal fen: Season-long measurement by eddy correlation, *Journal of Geophysical Research: Atmospheres* **101**(D22), 28637 – 28647.

Thornley, J. H. M.: 1998, Dynamic model of leaf photosynthesis with acclimation to light and nitrogen, *Annals of Botany* **81**(3), 421–430.

Tiemeyer, B., Albiac Borraz, E., Augustin, J., Bechtold, M., Beetz, S., Beyer, C., Drsler, M., Ebli, M., Eickenscheidt, T., Fiedler, S., Frster, C., Freibauer, A., Giebels, M., Glatzel, S., Heinichen, J., Hoffmann, M., Hper, H., Jurasinski, G., Leiber-Sauheitl, K., Peichl-Brak, M., Rokopf, N., Sommer, M. and Zeitz, J.: 2016, High emissions of greenhouse gases from grasslands on peat and other organic soils, *Global Change Biology* **22**(12), 4134–4149.

Tuhkanen, S.: 1990, *Tierra Del Fuego as a Target for Biogeographical Research in the Past and Present*, Anales del Instituto de la Patagonia: Serie ciencias naturales, Instituto de la Patagonia, Punta Arenas.

Tuhkanen, S.: 1992, *The climate of Tierra del Fuego from a vegetation geographical point of view and its ecoclimatic counterparts elsewhere*, Finnish Botanical Publishing Board, Helsinki.

Tuittila, E.-S., Komulainen, V.-M., Vasander, H. and Laine, J.: 1999,

Restored cut-away peatland as a sink for atmospheric co2, *Oecologia* **120**(4), 563–574.

Tuittila, E. S., Komulainen, V. M., Vasander, H., Nykanen, H., Martikainen, P. J. and Laine, J.: 2000, Methane dynamics of a restored cut-away peatland, *Global Change Biology* **6**(5), 569 – 581.

Tuzson, B., Hiller, R. V., Zeyer, K., Eugster, W., Neftel, a., Ammann, C. and Emmenegger, L.: 2010, Field intercomparison of two optical analyzers for CH_4 eddy covariance flux measurements, *Atmospheric Measurement Techniques* **3**(6), 1519 – 1531.

Vanselow-Algan, M., Schmidt, S. R., Greven, M., Fiencke, C., Kutzbach, L. and Pfeiffer, E.-M.: 2015, High methane emissions dominated annual greenhouse gas balances 30 years after bog rewetting, *Biogeosciences* **12**(14), 4361 – 4371.

Verma, S. B., Ullamn, F. G., Billesbach, D., Clement, R. J. and Kim, J.: 1992, Eddy correlation measurements of methane flux in a northern peatland ecosystem, *Boundary-Layer Meteorology* **58**, 289 – 304.

Vernay, A., Balandier, P., Guinard, L., Amglio, T. and Malagoli, P.: 2016, Photosynthesis capacity of quercus petraea (matt.) saplings is affected by molinia caerulea (l.) under high irradiance, *Forest Ecology and Management* **376**, 107 – 117.

Vickers, D. and Mahrt, L.: 1997, Quality control and flux sampling problems for tower and aircraft data, *Journal of Atmospheric and Oceanic Technology* **14**(3), 512 – 526.

Weischet, W.: 1985, Climatic constraints for the development of the far south of Latin America, *GeoJournal* **11**(1), 79–87.

Whalen, S. C.: 2005, Biogeochemistry of methane exchange between natural wetlands and the atmosphere, *Environmental Engineering Science* **22**(1).

Wille, C., Kutzbach, L., Sachs, T., Wagner, D. and Pfeiffer, E.-M.: 2008, Methane emission from Siberian arctic polygonal tundra: eddy covariance measurements and modeling, *Global Change Biology* **14**(6), 1395 – 1408.

Wilson, D., Alm, J., Laine, J., Byrne, K. a., Farrell, E. P. and Tuittila, E. S.: 2009, Rewetting of cutaway peatlands: Are we re-creating hot spots of methane emissions?, *Restoration Ecology* **17**(6), 796 – 806.

Wilson, D., Farrell, C. A., Fallon, D., Moser, G., Mller, C. and Renou-Wilson, F.: 2016, Multiyear greenhouse gas balances at a rewetted temperate peatland, *Global Change Biology* **22**(12), 4080–4095.

Wolpert, D. H.: 1992, Stacked generalization, *Neural Networks* **5**(2), 241 – 259.

Yu, Z., Loisel, J., Brosseau, D. P., Beilman, D. W. and Hunt, S. J.: 2010, Global peatland dynamics since the last glacial maximum, *Geophysical Research Letters* **37**(13), n/a–n/a. L13402.

Zahniser, M. S., Nelson, D. D., Mcmanus, J. B. and Kebabian, P. L.: 1995, Measurement of trace gas fluxes using tunable diode laser spectroscopy, *Philosophical Transactions: Physical Sciences and Engineering* **351**(1696), 371 – 382.

Zeltner, U.: 2003, *Schutzgebiets- und Biotopverbundsystem Schleswig-Holstein- regionale Ebene - (Gebiete von überörtlicher Bedeutung für den Arten- und Biotopschutz); Fachbeitrag zur Landschaftsrahmenplanung; Spezieller Teil; Planungsraum I - Teilbereich Kreis Pinneberg*, Landesamt für Natur und Umwelt des Landes Schleswig-Holstein, Flintbek.

Zheng, Y., Zhao, Z., Zhou, J.-J. and Zhou, H.: 2012, Evaluations of different leaf and canopy photosynthesis models: a case study with black locust (robinia pseudoacacia) plantations on a loess plateau, *Pakistan Journal of Botany* **44**, 531–539.

Zhu, X., Zhuang, Q., Qin, Z., Glagolev, M. and Song, L.: 2013, Estimating wetland methane emissions from the northern high latitudes from 1990 to 2009 using artificial neural networks, *Global Biogeochemical Cycles* **27**(2), 592 – 604.

Appendices

Appendix A

Tower view gap-filling suplementary

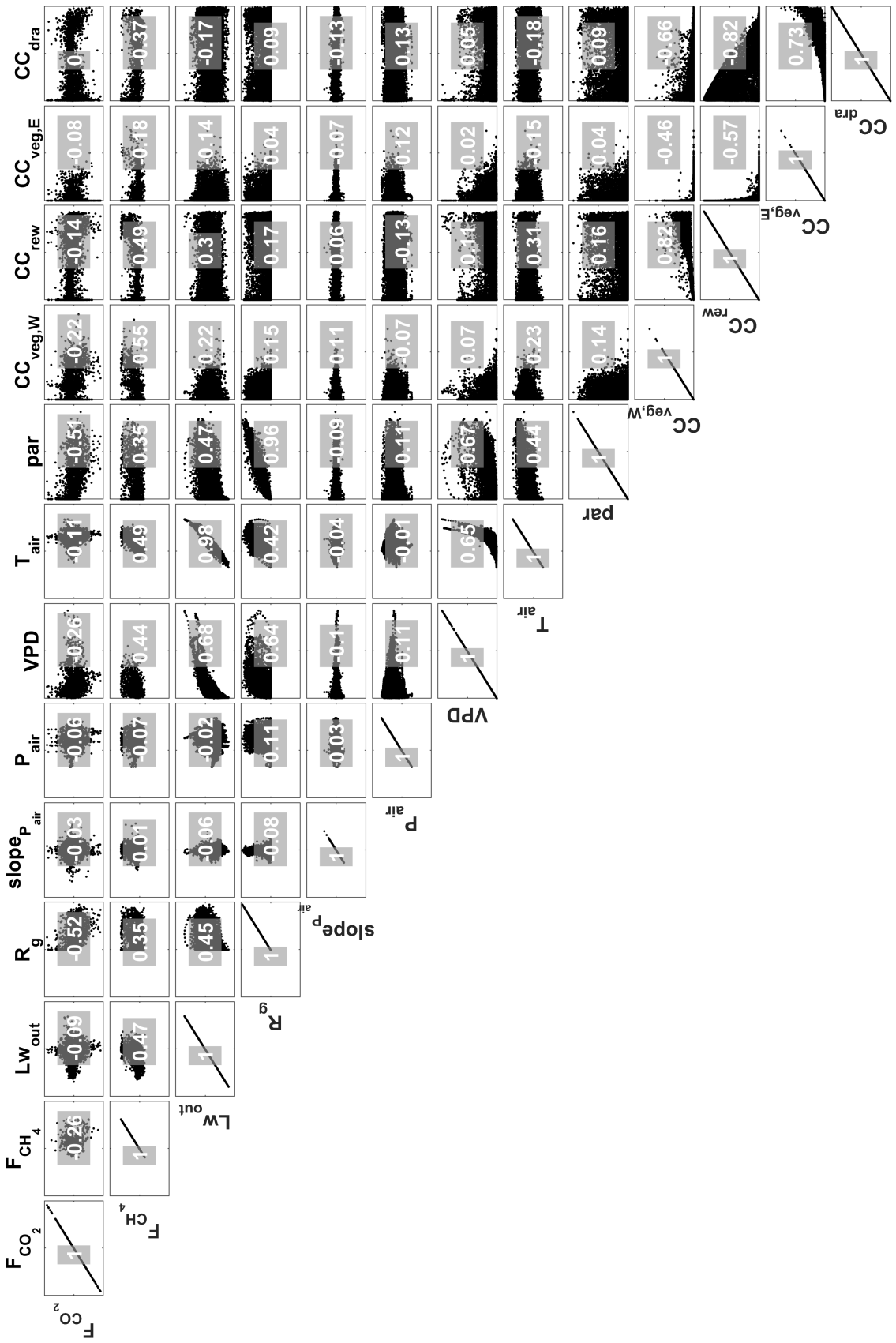

Figure A.1: Pearson's correlation coefficients of Year 1 input-target matrix. #1

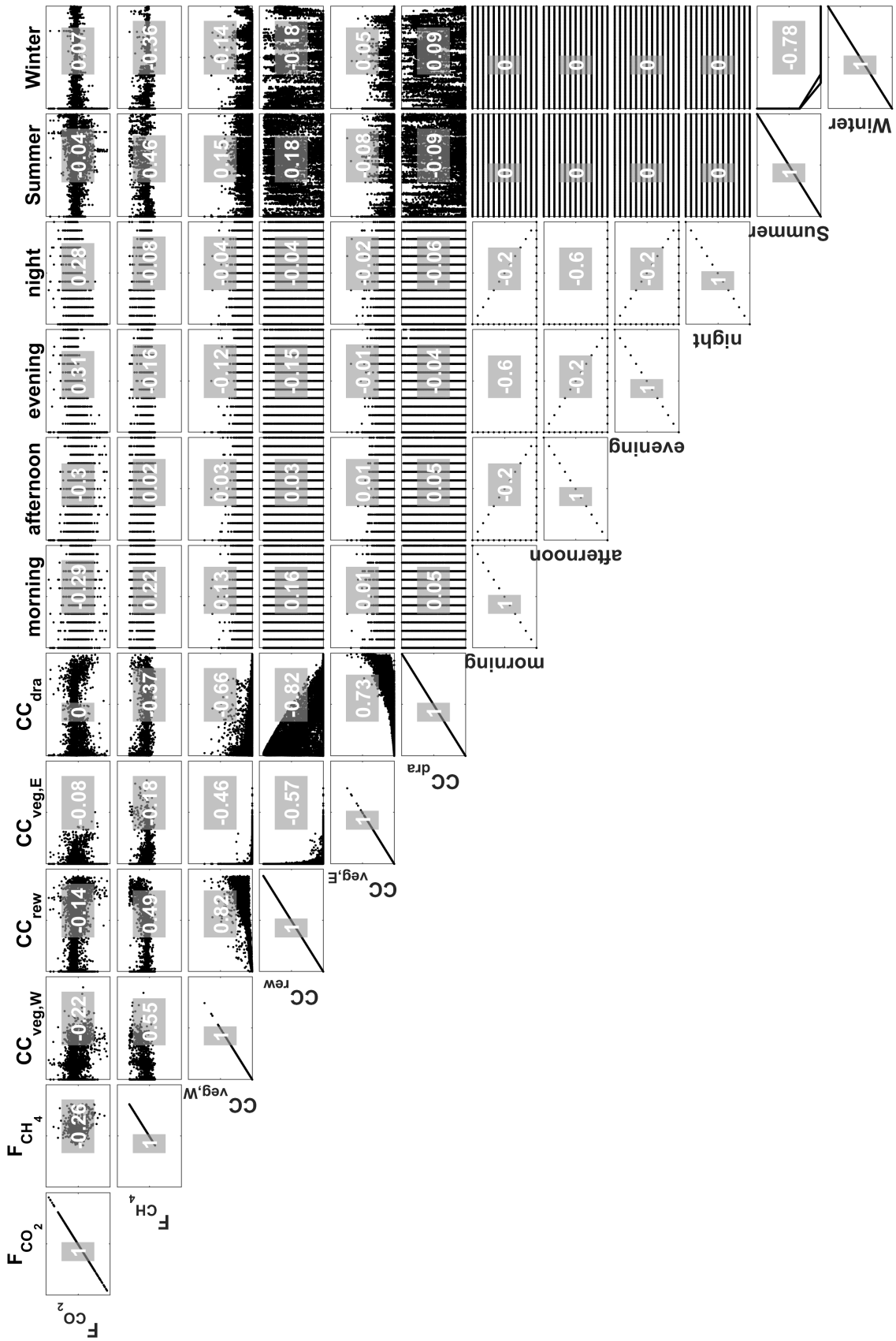

Figure A.2: Pearson's correlation coefficients of Year 1 input-target matrix. #2

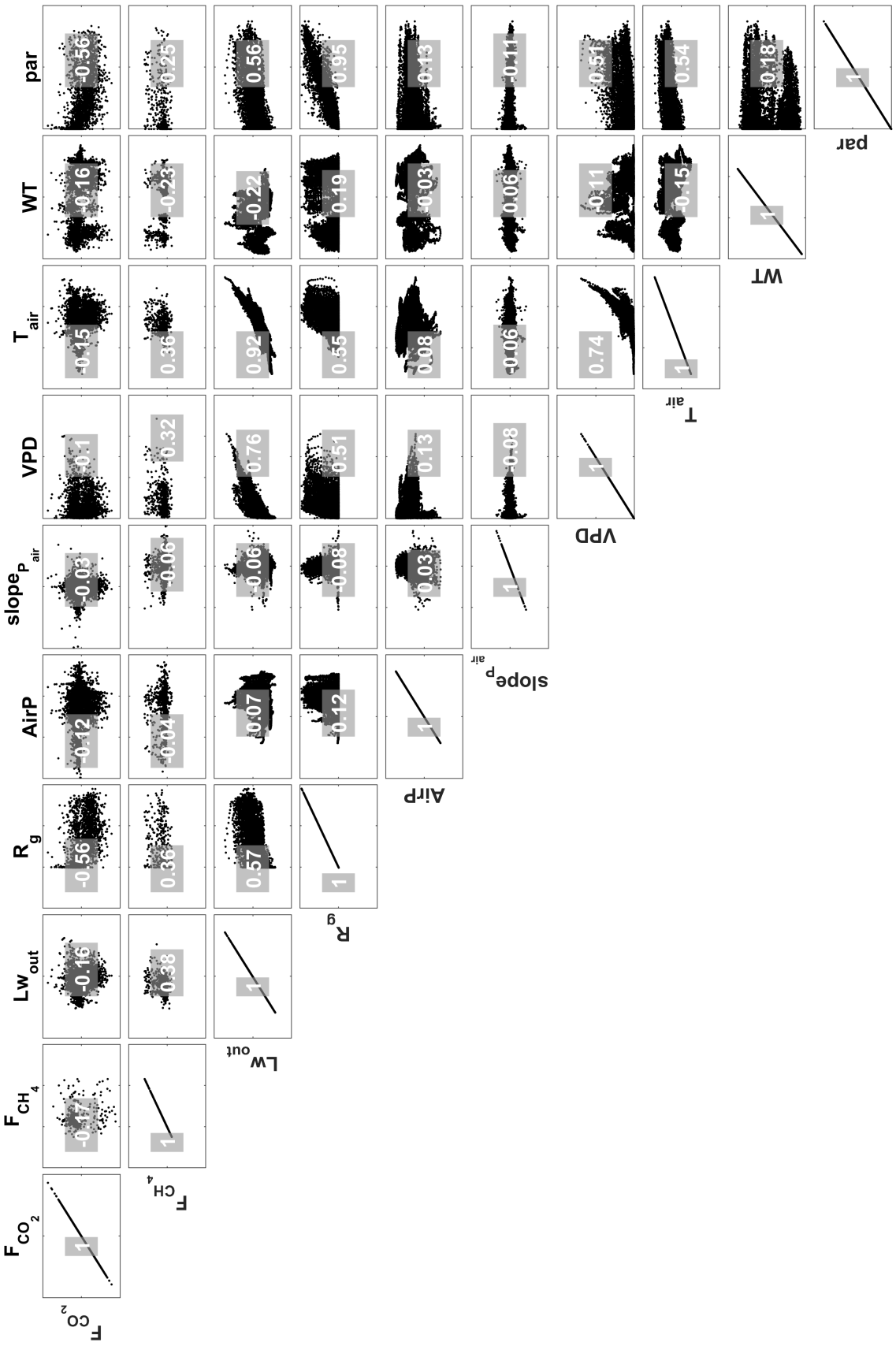

Figure A.3: Pearson's correlation coefficients of Year 2 input-target matrix. #1

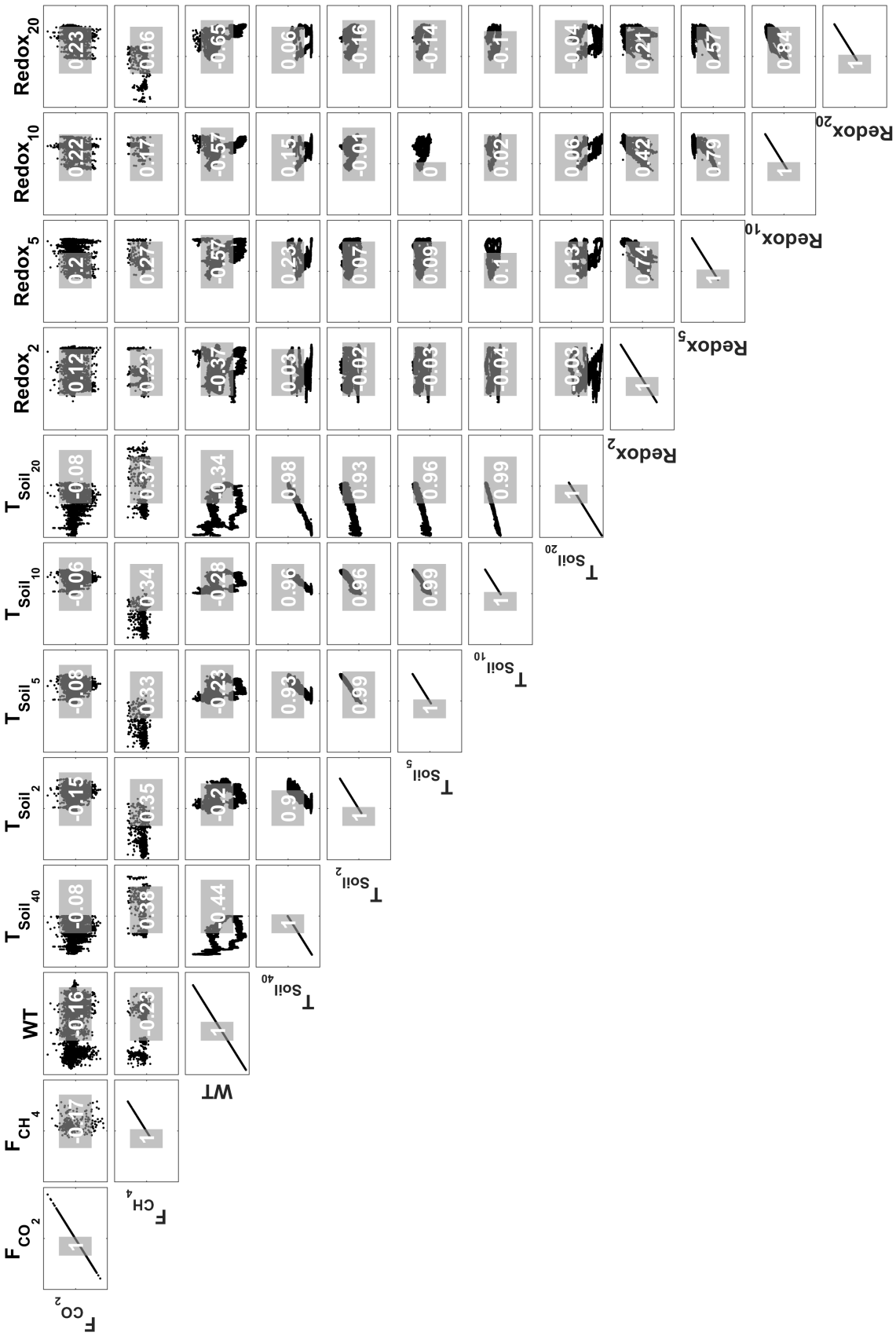

Figure A.4: Pearson's correlation coefficients of Year 2 input-target matrix. #2

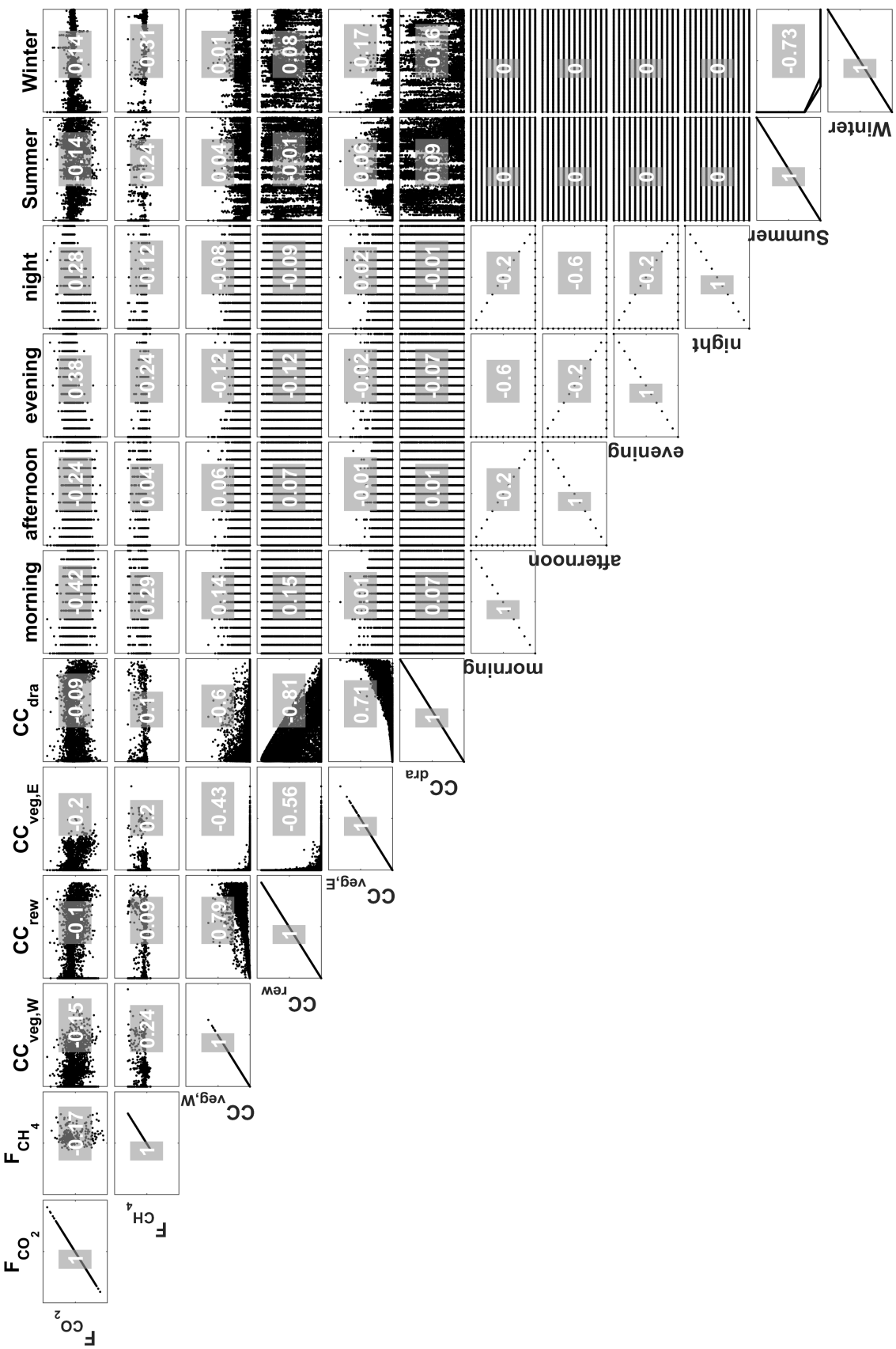

Figure A.5: Pearson's correlation coefficients of Year 2 input-target matrix. #3

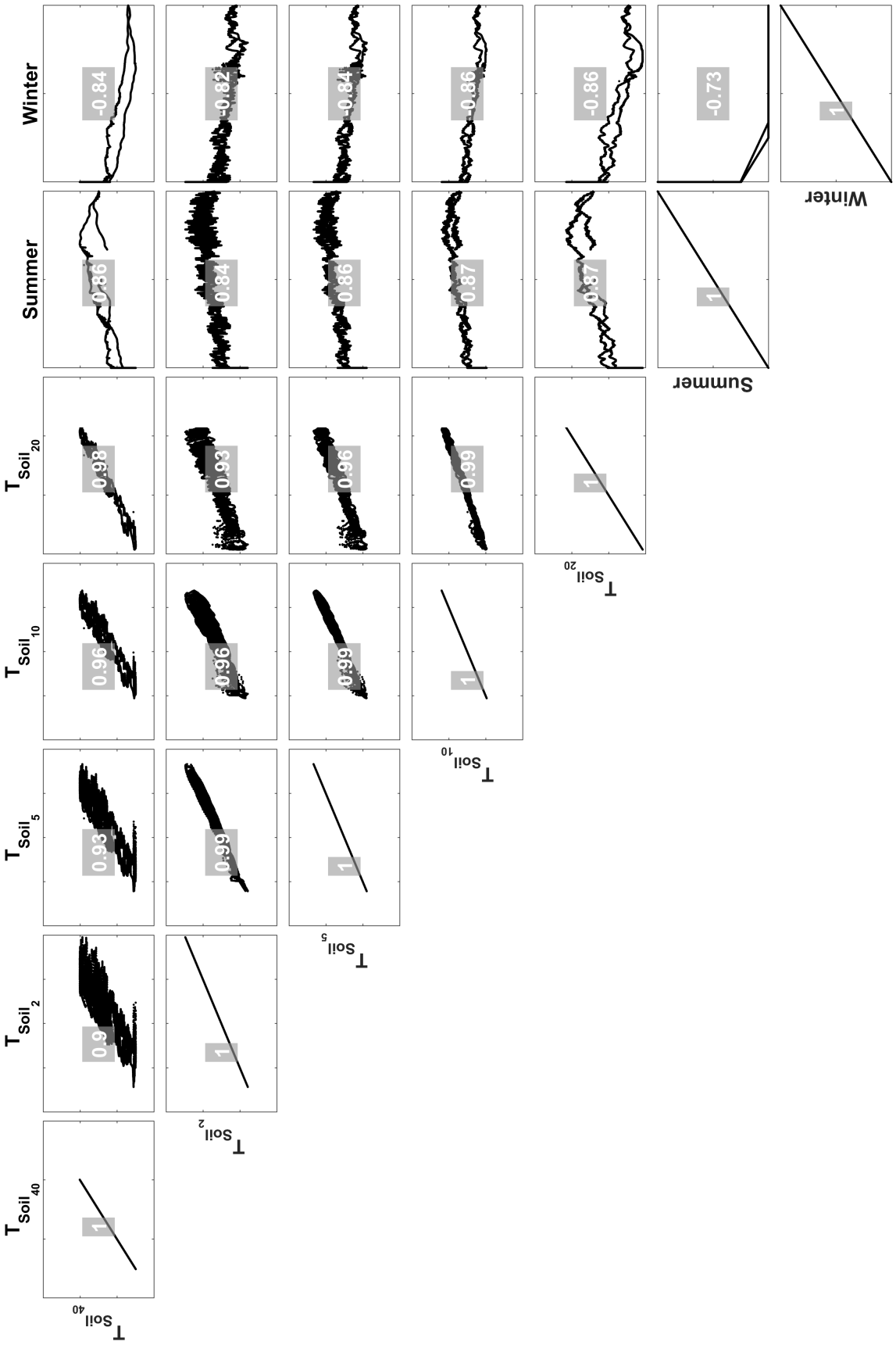

Figure A.6: Pearson's correlation coefficient of input-target matrix Year 2. #4

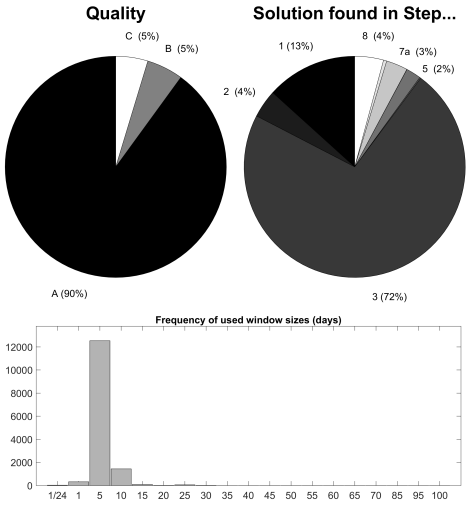

Figure A.7: Quality of Year 1 F_{CH4} values within MDS gap-filling.

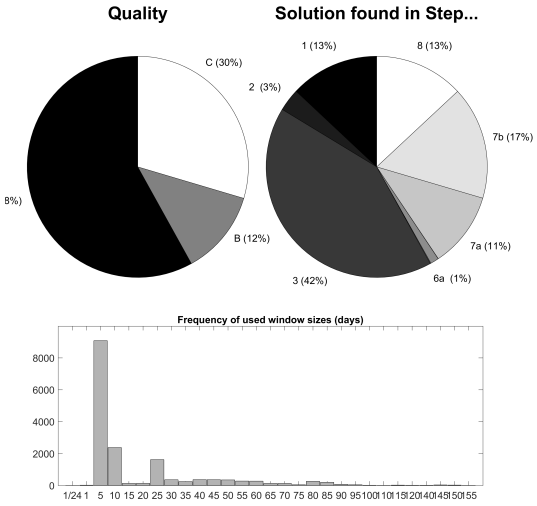

Figure A.8: Quality of Year 2 F_{CH4} values within MDS gap-filling.

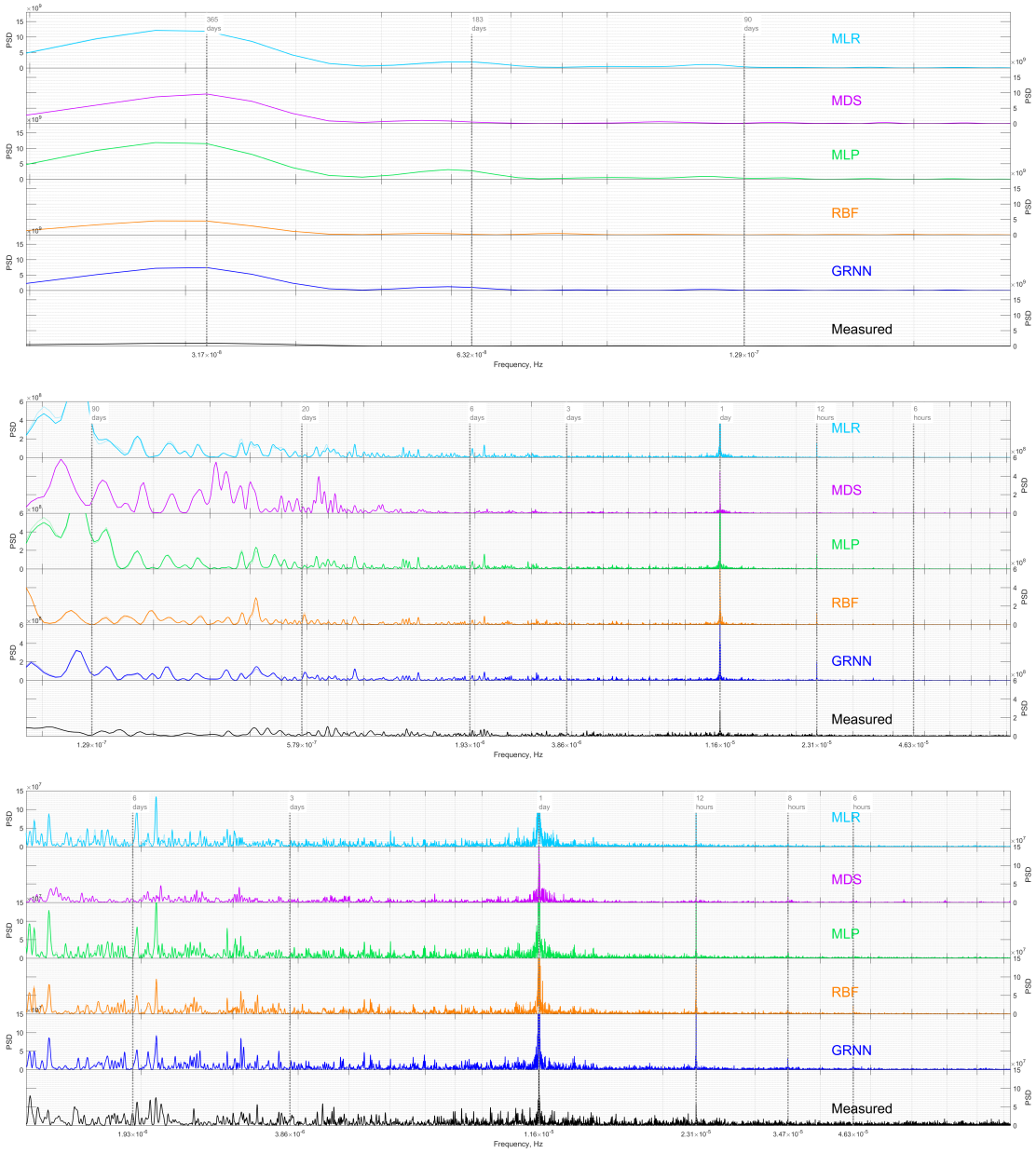

Figure A.9: Lomb-Scargle periodograms of the measured and gap-filled transformed two year time F_{CH4} series. PSD: power spectral density, MLR: multilinear regression; MDS: marginal distribution sampling; MLP: multilayer perceptron; RBF: radial basis function network; GRNN: generalized regression neural network

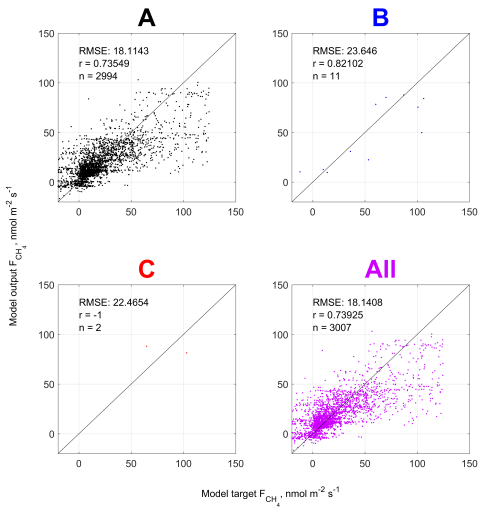

Figure A.10: Results of MDS_{QC} with Year 1 F_{CH4}.

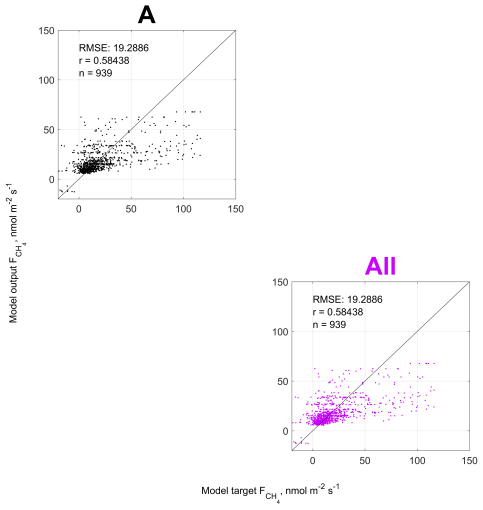

Figure A.11: Results of MDS_{QC} with Year 2 F_{CH4}.

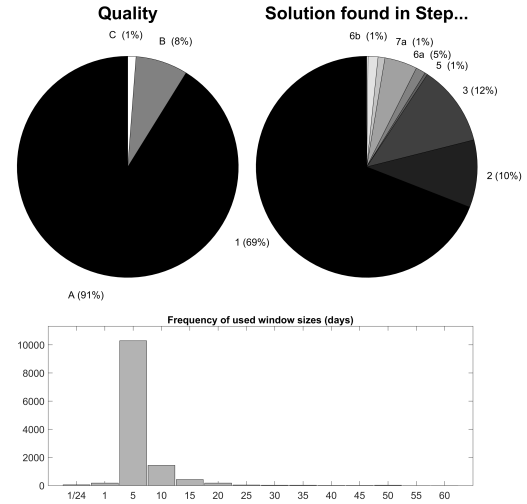

Figure A.12: Quality of Year 1 F_{CO2} values within MDS gap-filling.

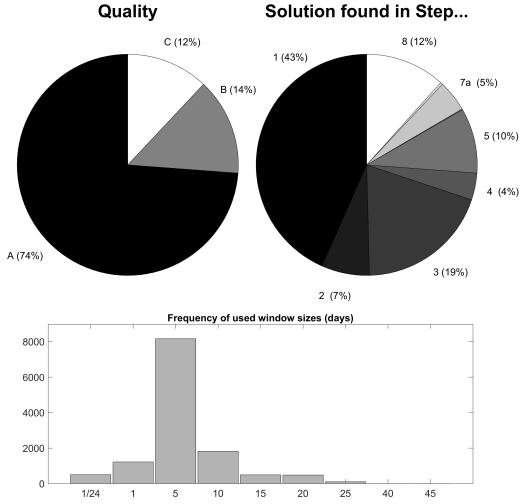

Figure A.13: Quality of Year 2 F_{CO2} values within MDS gap-filling.

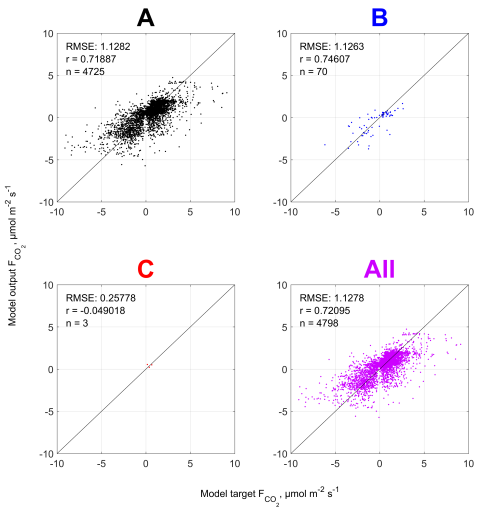

Figure A.14: Results of MDS_{QC} with Year 1 F_{CO_2}.

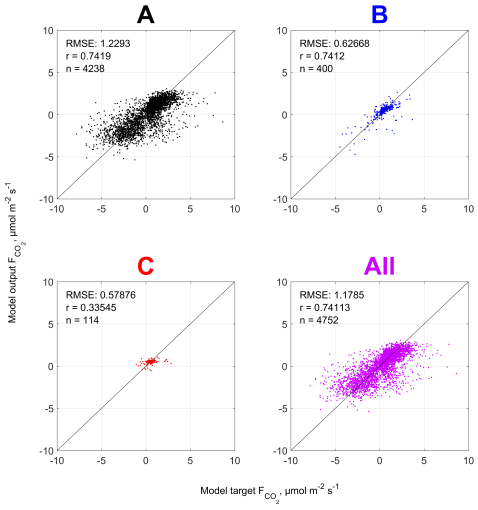

Figure A.15: Results of MDS_{QC} with Year 2 F_{CO_2}.

Appendix B

Surface class view methane flux gap-filling suplementary

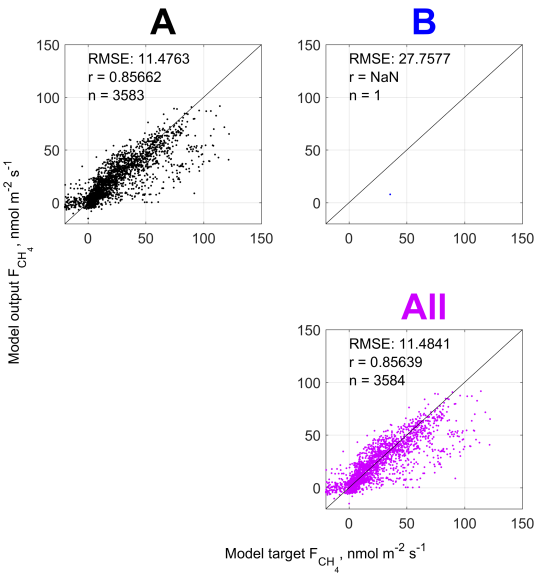

Figure B.1: Results of MDS_{QC} with Year 1 F_{CH4} from SC_{dra}.

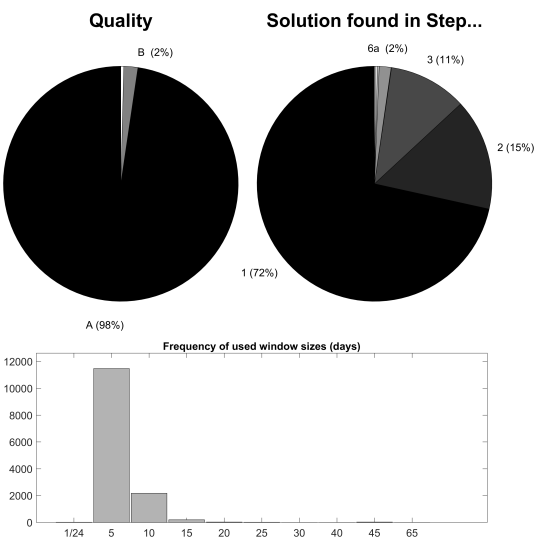

Figure B.2: Quality of Year 1 F_{CH4} from SC_{dra} values within MDS gap-filling.

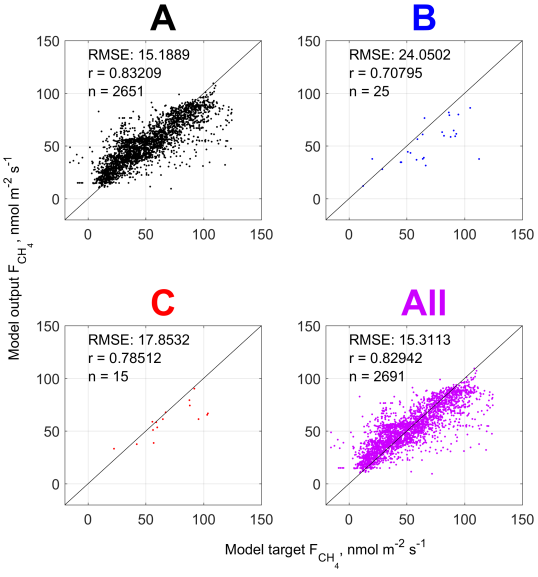

Figure B.3: Results of MDS_{QC} with Year 1 F_{CH4} from SC_{rew}.

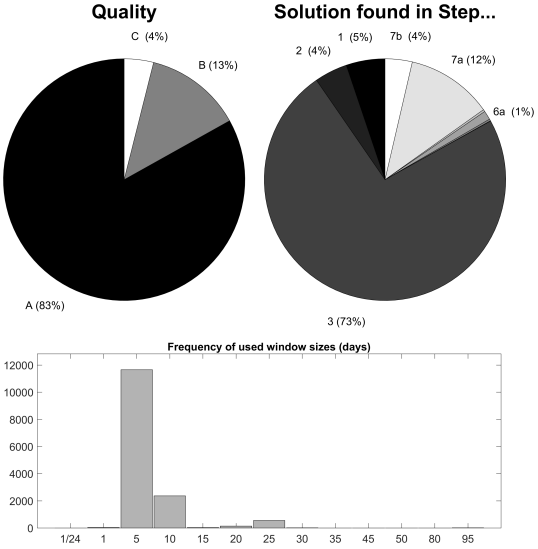

Figure B.4: Quality of Year 1 F_{CH4} from SC_{rew} values within MDS gap-filling.

Table B.1: F_{CH4} model statistics, Year 1 SC_{dra}

	MLR	MDS	MLP	RBF	GRNN
r	0.83	0.86	0.93	0.91	0.95
RMSE	12.35	11.48	7.96	9.09	7.08
AIC	18045.83	-	15229.58	16410.25	52772.28
BE	0.00	0.83	-0.05	0.07	0.22
MAE	8.32	6.71	3.96	4.69	3.74
scaling exponent	-0.88	-0.79	-0.93	-0.89	-0.92

Table B.2: F_{CH4} model statistics, Year 1 SC_{rew}

	MLR	MDS	MLP	RBF	GRNN
r	0.90	0.83	0.95	0.93	0.96
RMSE	12.11	15.29	8.73	10.02	7.51
AIC	13455.71	-	12006.71	13637.19	43363.52
BE	0.00	-0.69	0.05	0.19	-0.04
MAE	7.81	10.96	3.86	5.53	4.07
scaling exponent	-0.91	-0.81	-0.94	-0.93	-0.94

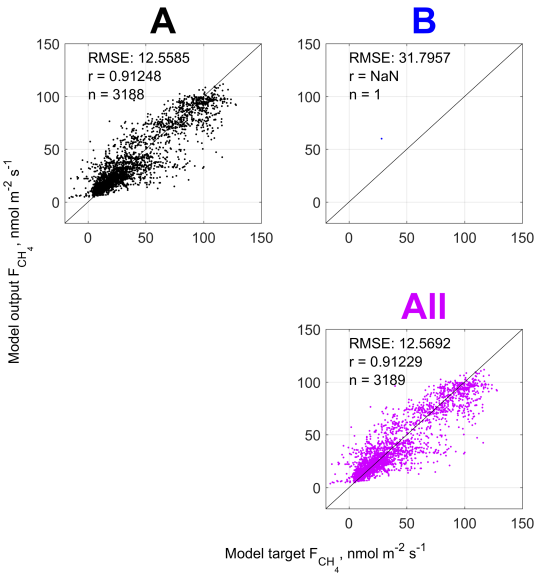

Figure B.5: Results of MDS_{QC} with Year 2 F_{CH4} from SC_{dra}.

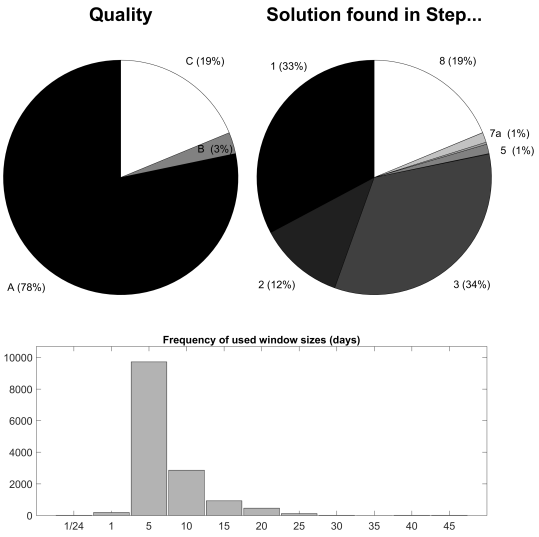

Figure B.6: Quality of Year 2 F_{CH4} from SC_{dra} values within MDS gap-filling.

Table B.3: Input selection result (**bold**: in final Matrix) for Year 1 F_{CH4} from SC_{dra}

	Timelag	Score
Lw_{out}	1.5	7.0
R_g	-0.5	4.0
$slope_{Pair}$	0.0	2.0
P_{air}	7.5	4.0
VPD	1.0	8.0
T_{air}	2.0	7.0
Lw_{out} #lag	-	6.0
R_g #lag	-	5.0
P_{air} #lag	-	4.0
VPD #lag	-	7.0
T_{air} #lag	-	8.0
$CC_{veg,E}$	-	12.0
CC_{dra}	-	1.0
$fuzzy_{mo}$	-	8.0
$fuzzy_{af}$	-	10.0
$fuzzy_{ev}$	-	5.0
$fuzzy_{ni}$	-	5.0
$fuzzy_{su}$	-	12.0
$fuzzy_{wi}$	-	8.0

Table B.4: Input selection result (**bold**: in final Matrix) for Year 1 F_{CH4} from SC_{rew}

	Timelag	Score
Lw_{out}	1.0	7.0
R_g	-1.0	3.0
$slope_{Pair}$	1.5	1.0
P_{air}	-7.0	7.0
VPD	0.0	8.0
T_{air}	0.5	7.0
Lw_{out} #lag	-	8.0
R_g #lag	-	5.0
$slope_{Pair}$ #lag	-	3.0
P_{air} #lag	-	3.0
T_{air} #lag	-	8.0
$CC_{veg,W}$	-	12.0
CC_{rew}	-	2.0
$fuzzy_{mo}$	-	8.0
$fuzzy_{af}$	-	11.0
$fuzzy_{ev}$	-	6.0
$fuzzy_{ni}$	-	6.0
$fuzzy_{su}$	-	12.0
$fuzzy_{wi}$	-	6.0

Table B.5: F_{CH4} model statistics, Year 2 SC_{dra}. RMSE, BE and MAE in nmol m^{-2} s^{-1}.

	MLR	MDS	MLP	RBF	GRNN
r	0.95	0.91	0.99	0.97	0.99
RMSE	9.47	12.57	5.05	7.23	4.63
AIC	14403.28	-	10806.58	15619.14	75774.42
BE	0.00	0.28	-0.04	0.21	0.13
MAE	6.45	8.34	1.91	4.56	2.52
scaling exponent	-1.01	-0.89	-1.03	-1.04	-1.03

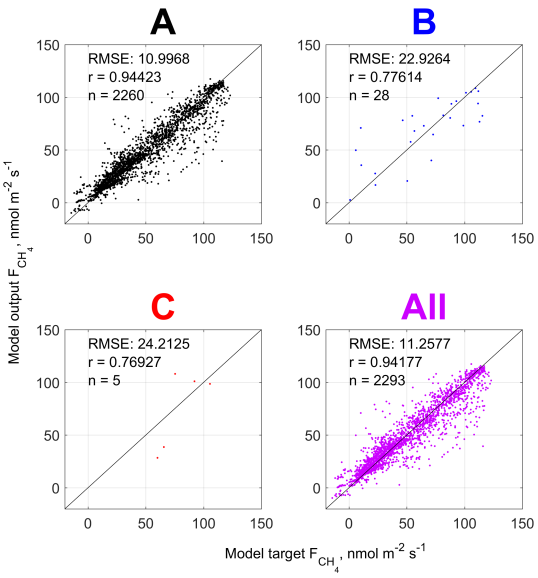

Figure B.7: Results of MDS_{QC} with Year 2 F_{CH4} from SC_{rew}.

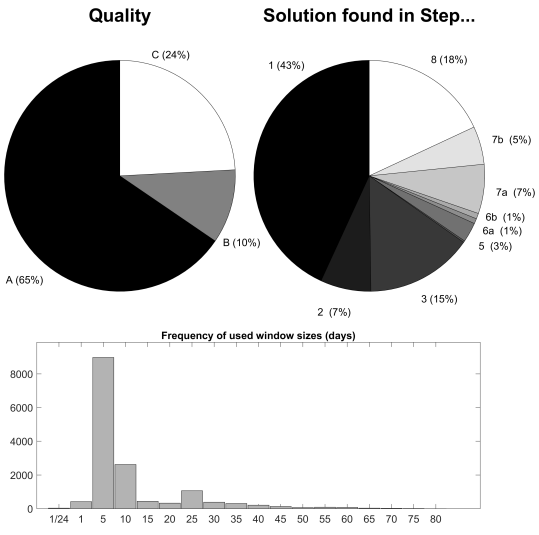

Figure B.8: Quality of Year 2 F_{CH4} from SC_{rew} values within MDS gap-filling.

Table B.6: F_{CH4} model statistics, Year 2 SC_{rew}. RMSE, BE and MAE in nmol m^{-2} s^{-1}.

	MLR	MDS	MLP	RBF	GRNN
r	0.96	0.94	0.99	0.98	0.99
RMSE	9.69	11.26	4.40	6.91	4.91
AIC	10463.63	-	7297.34	12295.15	47269.75
BE	0.00	0.73	0.00	0.27	0.24
MAE	6.92	7.31	1.61	4.32	3.05
scaling exponent	-1.03	-1.05	-1.08	-1.10	-1.02

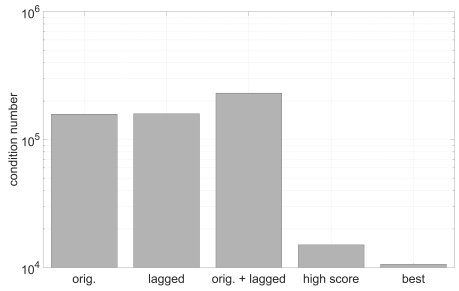

Figure B.9: Development of the input matrix condition number throughout variable selection for Year 1 SC_{dra} F_{CH4} gap-filling.

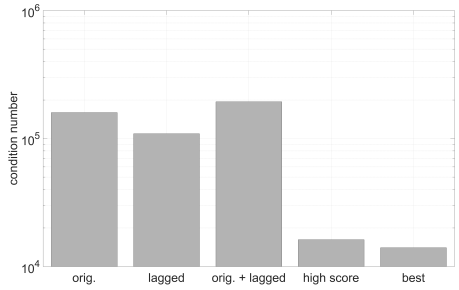

Figure B.10: Development of the input matrix condition number throughout variable selection for Year 1 SC_{rew} F_{CH4} gap-filling.

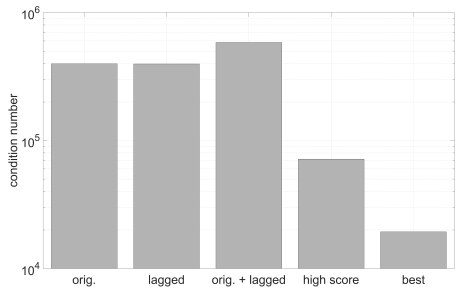

Figure B.11: Development of the input matrix condition number throughout variable selection for Year 2 SC_{dra} F_{CH4} gap-filling.

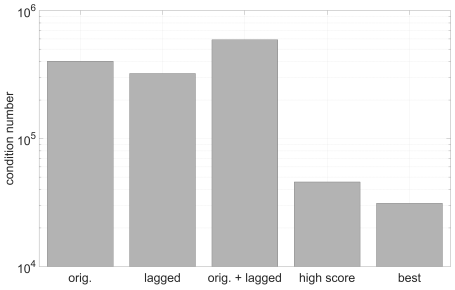

Figure B.12: Development of the input matrix condition number throughout variable selection for Year 2 SC_{rew} F_{CH4} gap-filling.

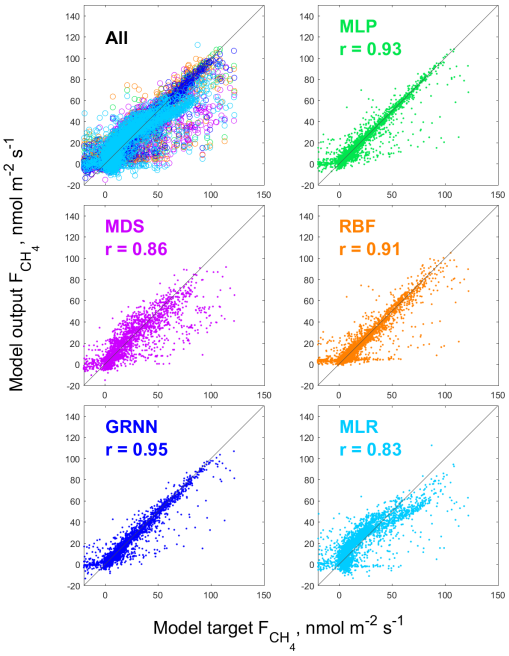

Figure B.13: Scatter plots of all Year 1 F_{CH4} SC_{dra} models vs. target fluxes.

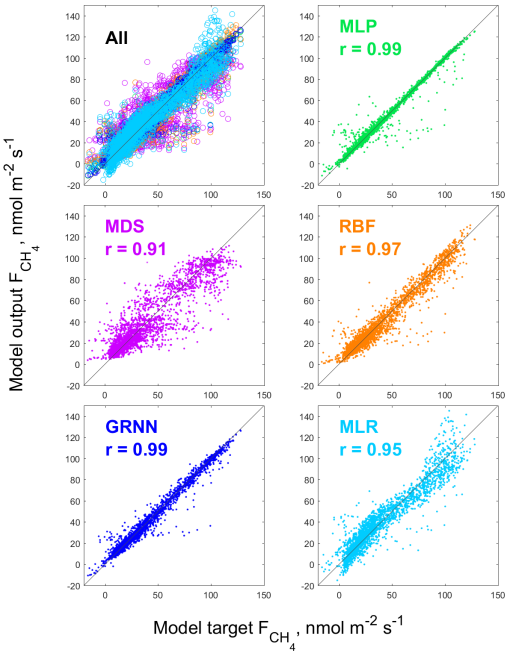

Figure B.15: Scatter plots of all Year 2 F_{CH4} SC_{dra} models vs. target fluxes.

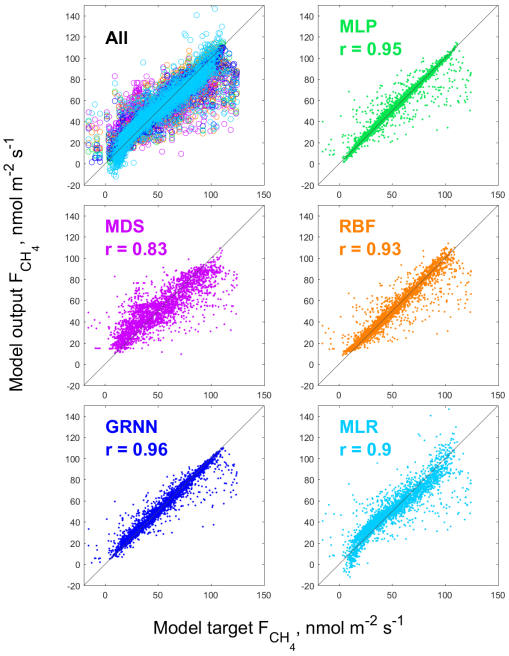

Figure B.14: Scatter plots of all Year 1 F_{CH4} SC_{rew} models vs. target fluxes.

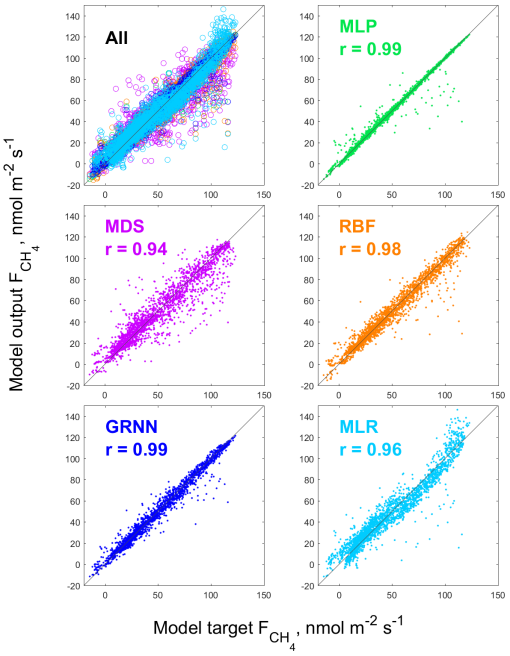

Figure B.16: Scatter plots of all Year 2 F_{CH4} SC_{dra} models vs. target fluxes.

Table B.7: Input selection result (**bold**: in final Matrix) for Year 2 F_{CH4} from SC_{dra}

	Timelag	Score
Lw_{out}	2.5	7.0
R_g	1.0	2.0
P_{air}	7.5	1.0
$slope_{Pair}$	4.0	2.0
VPD	3.0	8.0
T_{air}	3.5	6.0
WT	-2.5	4.0
T_{Soil40}	-5.0	8.0
T_{Soil2}	5.0	7.0
T_{Soil5}	-5.5	8.0
T_{Soil10}	-2.5	7.0
T_{Soil20}	1.5	6.0
$Redox_2$	2.0	7.0
$Redox_5$	1.5	5.0
$Redox_{10}$	1.0	8.0
$Redox_{20}$	2.0	6.0
Lw_{out} #lag	-	5.0
R_g #lag	-	1.0
P_{air} #lag	-	1.0
$slope_{Pair}$ #lag	-	0.0
VPD #lag	-	6.0
T_{air} #lag	-	5.0
WT #lag	-	6.0
T_{Soil40} #lag	-	8.0
T_{Soil2} #lag	-	7.0
T_{Soil5} #lag	-	7.0
T_{Soil10} #lag	-	8.0
T_{Soil20} #lag	-	7.0
$Redox_2$ #lag	-	7.0
$Redox_5$ #lag	-	8.0
$Redox_{10}$ #lag	-	7.0
$Redox_{20}$ #lag	-	6.0
$CC_{veg,E}$	-	12.0
CC_{dra}	-	3.0
$fuzzy_{mo}$	-	9.0
$fuzzy_{af}$	-	8.0
$fuzzy_{ev}$	-	7.0
$fuzzy_{ni}$	-	6.0
$fuzzy_{su}$	-	10.0
$fuzzy_{wi}$	-	7.0

Table B.8: Input selection result (**bold**: in final Matrix) for Year 2 F_{CH4} from SC_{rew}

	Timelag	Score
Lw_{out}	0.5	6.0
R_g	0.0	6.0
P_{air}	11.0	1.0
$slope_{Pair}$	-4.5	1.0
VPD	2.5	8.0
T_{air}	2.0	6.0
WT	7.0	8.0
T_{Soil40}	-5.5	7.0
T_{Soil2}	4.0	7.0
T_{Soil5}	-5.5	8.0
T_{Soil10}	-2.5	6.0
T_{Soil20}	2.0	8.0
$Redox_2$	2.0	6.0
$Redox_5$	0.0	6.0
$Redox_{10}$	0.0	8.0
$Redox_{20}$	1.0	8.0
Lw_{out} #lag	-	5.0
P_{air} #lag	-	1.0
$slope_{Pair}$ #lag	-	3.0
VPD #lag	-	5.0
T_{air} #lag	-	6.0
WT #lag	-	8.0
T_{Soil40} #lag	-	7.0
T_{Soil2} #lag	-	7.0
T_{Soil5} #lag	-	7.0
T_{Soil10} #lag	-	6.0
T_{Soil20} #lag	-	7.0
$Redox_2$ #lag	-	8.0
$Redox_{20}$ #lag	-	7.0
$CC_{veg,W}$	-	12.0
CC_{rew}	-	3.0
$fuzzy_{mo}$	-	9.0
$fuzzy_{af}$	-	7.0
$fuzzy_{ev}$	-	7.0
$fuzzy_{ni}$	-	7.0
$fuzzy_{su}$	-	9.0
$fuzzy_{wi}$	-	12.0

Appendix C

Surface class view carbon dioxide flux gap-filling suplementary

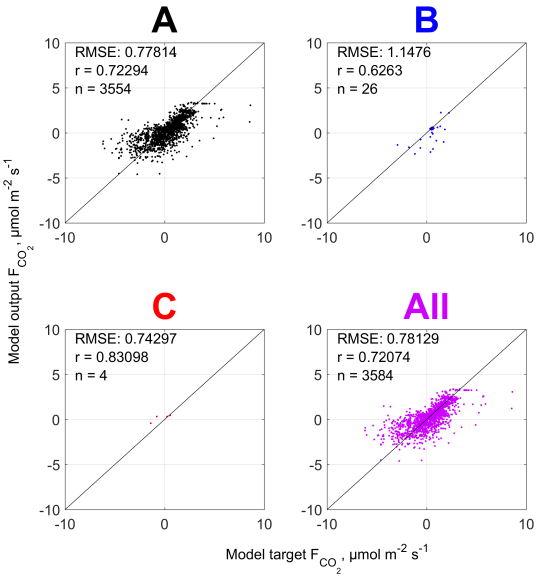

Figure C.1: Results of MDS_{QC} with Year 1 F_{CO2} from SC_{dra}

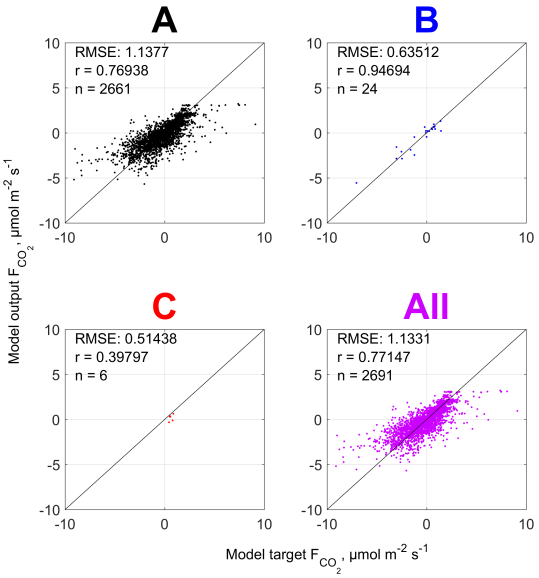

Figure C.3: Results of MDS_{QC} with Year 1 F_{CO2} from SC_{rew}

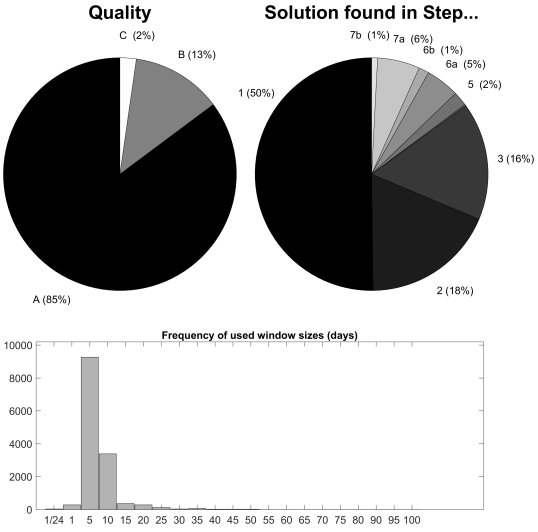

Figure C.2: Quality of Year 1 F_{CO2} SC_{dra} values within MDS gap-filling.

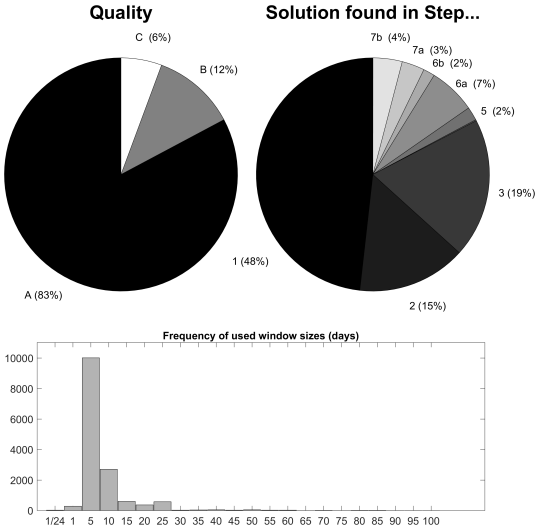

Figure C.4: Quality of Year 1 F_{CO2} SC_{rew} values within MDS gap-filling.

Table C.1: F_{CO2} model statistics, Year 1 SC_{dra}. RMSE, BE and MAE in µmol m^{-2} s^{-1}.

	MLR	MDS	MLP	RBF	GRNN
r	0.56	0.72	0.89	0.86	0.92
RMSE	0.93	0.78	0.52	0.57	0.46
AIC	-479.00	-	-4464.25	-2980.99	41849.63
BE	0.00	0.01	-0.00	-0.00	-0.01
MAE	0.60	0.41	0.23	0.28	0.22
scaling exponent	-0.99	-0.74	-1.11	-1.09	-0.99

Table C.2: F_{CO2} model statistics, Year 1 SC_{rew}. RMSE, BE and MAE in µmol m^{-2} s^{-1}.

	MLR	MDS	MLP	RBF	GRNN
r	0.73	0.77	0.86	0.83	0.87
RMSE	1.20	1.13	0.90	0.98	0.88
AIC	1039.93	-	-437.25	380.46	34843.43
BE	-0.00	0.01	-0.00	0.00	0.02
MAE	0.84	0.75	0.52	0.62	0.54
scaling exponent	-1.17	-0.87	-1.21	-1.15	-1.10

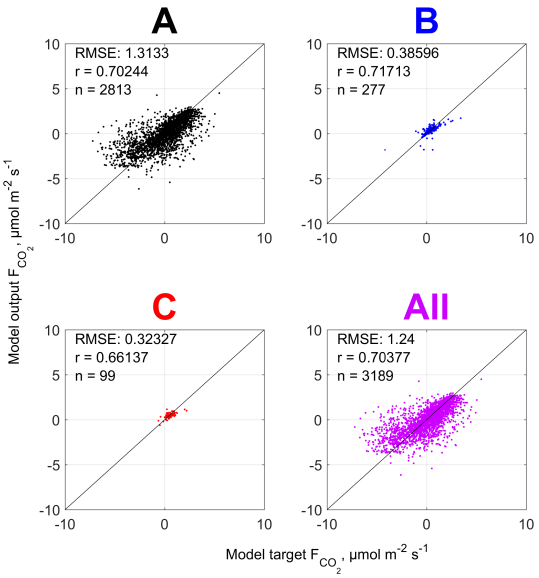

Figure C.5: Results of MDS_{QC} with Year 2 F_{CO2} from SC_{dra}

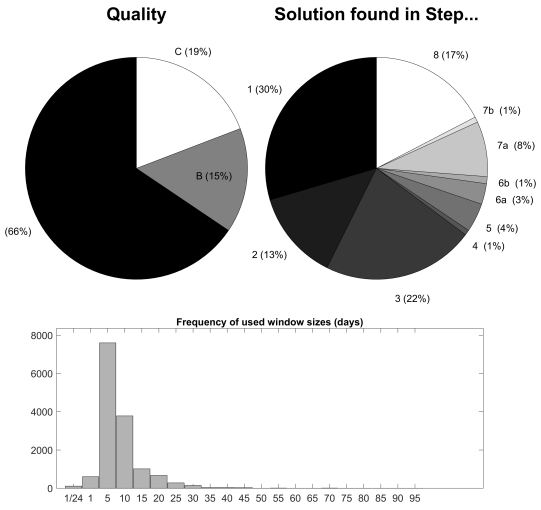

Figure C.6: Quality of Year 2 F_{CH4} SC_{dra} values within MDS gap-filling.

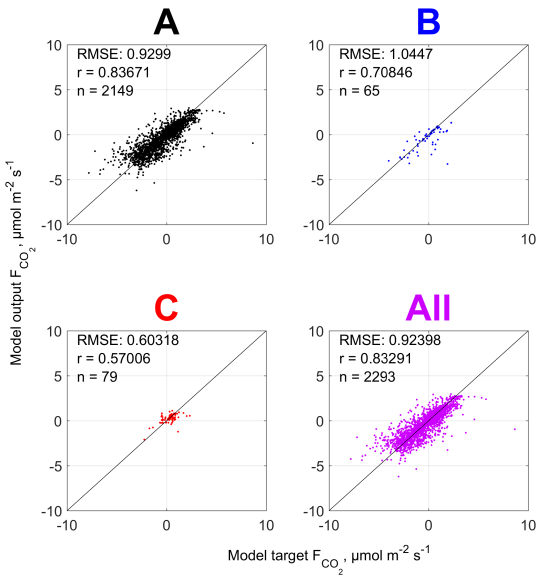

Figure C.7: Results of MDS_{QC} with Year 2 F_{CO2} from SC_{rew}

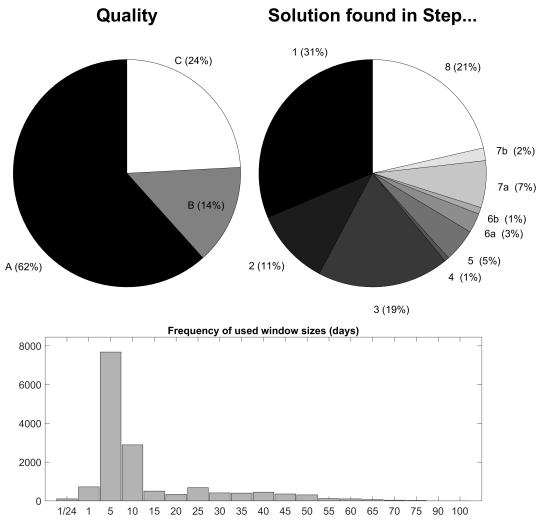

Figure C.8: Quality of Year 2 F_{CO2} SC_{rew} values within MDS gap-filling.

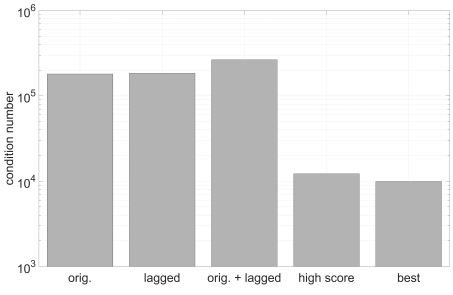

Figure C.9: Development of the input matrix condition number throughout variable selection for Year 1 SC_{dra} F_{CO2} gap-filling.

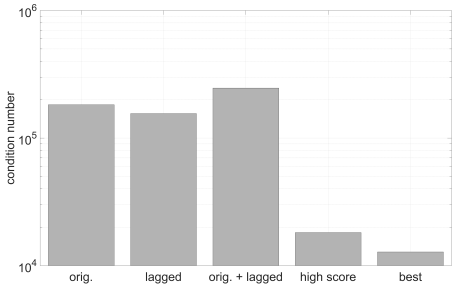

Figure C.10: Development of the input matrix condition number throughout variable selection for Year 1 SC_{rew} F_{CO2} gap-filling.

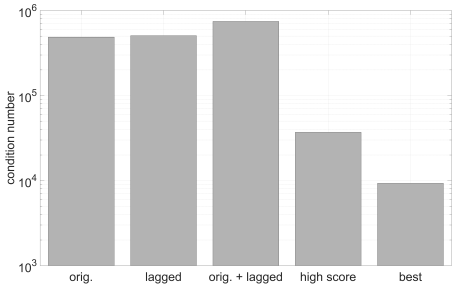

Figure C.11: Development of the input matrix condition number throughout variable selection for Year 2 SC_{dra} F_{CO2} gap-filling.

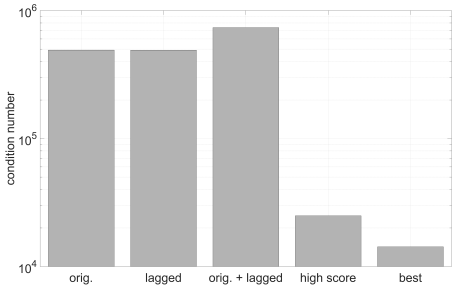

Figure C.12: Development of the input matrix condition number throughout variable selection for Year 2 SC_{rew} F_{CO2} gap-filling.

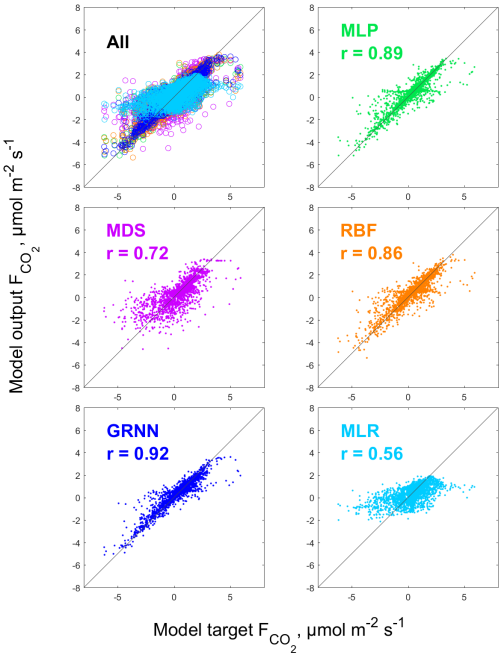

Figure C.13: Scatter plots of all Year 1 F_{CO2} SC_{dra} models vs. target fluxes.

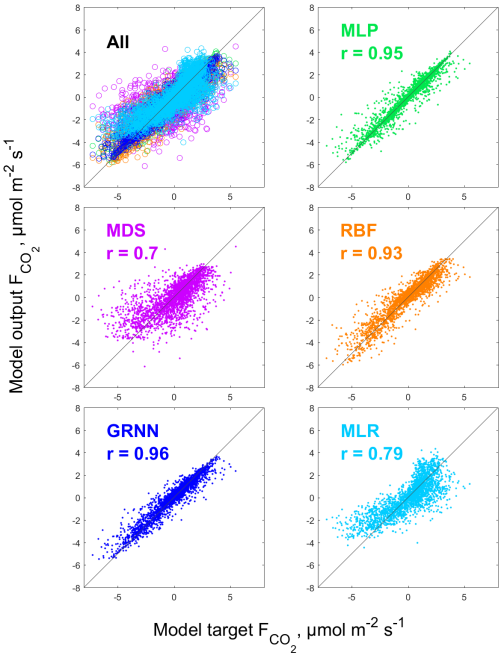

Figure C.15: Scatter plots of all Year 2 F_{CO2} SC_{dra} models vs. target fluxes.

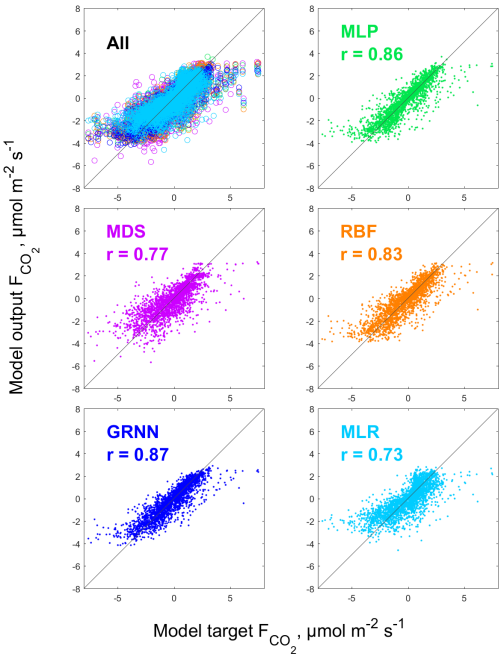

Figure C.14: Scatter plots of all Year 1 F_{CO2} SC_{rew} models vs. target fluxes.

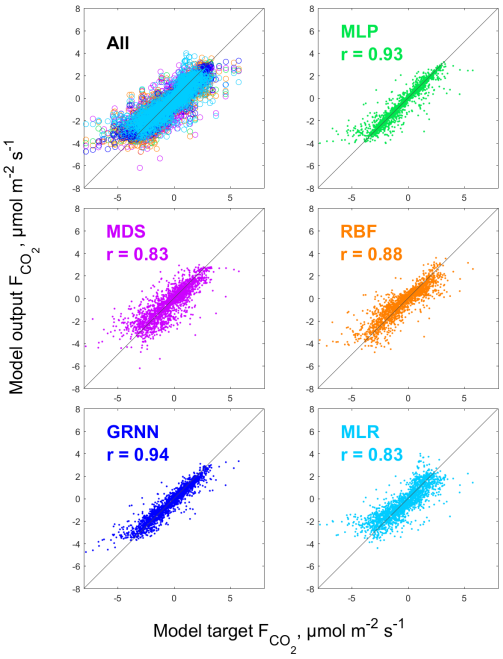

Figure C.16: Scatter plots of all Year 2 F_{CO2} SC_{rew} models vs. target fluxes.

Table C.3: Input selection result (**bold**: in final Matrix) for Year 1 F_{CO_2} from SC_{rew}

	Timelag	Score
Lw_{out}	1.5	8.0
R_g	0.0	8.0
$slope_{Pair}$	-3.0	2.0
P_{air}	8.0	0.0
VPD	1.0	3.0
T_{air}	0.5	8.0
par	0.0	7.0
Lw_{out} #lag	-	8.0
$slope_{Pair}$ #lag	-	2.0
P_{air} #lag	-	1.0
VPD #lag	-	6.0
T_{air} #lag	-	6.0
$CC_{veg,W}$	-	12.0
CC_{rew}	-	3.0
$fuzzy_{mo}$	-	10.0
$fuzzy_{af}$	-	11.0
$fuzzy_{ev}$	-	8.0
$fuzzy_{ni}$	-	11.0
$fuzzy_{su}$	-	9.0
$fuzzy_{wi}$	-	12.0

Table C.4: Input selection result (**bold**: in final Matrix) for Year 1 F_{CO_2} from SC_{dra}

	Timelag	Score
Lw_{out}	1.0	8.0
R_g	-0.5	7.0
$slope_{Pair}$	7.0	0.0
P_{air}	3.0	3.0
VPD	0.5	5.0
T_{air}	1.0	8.0
par	-0.5	7.0
Lw_{out} #lag	-	7.0
R_g #lag	-	7.0
$slope_{Pair}$ #lag	-	0.0
P_{air} #lag	-	2.0
VPD #lag	-	5.0
T_{air} #lag	-	7.0
par #lag	-	3.0
$CC_{veg,E}$	-	12.0
CC_{dra}	-	4.0
$fuzzy_{mo}$	-	8.0
$fuzzy_{af}$	-	9.0
$fuzzy_{ev}$	-	9.0
$fuzzy_{ni}$	-	6.0
$fuzzy_{su}$	-	12.0
$fuzzy_{wi}$	-	12.0

Table C.5: F_{CO_2} model statistics, Year 2 SC_{dra}. RMSE, BE and MAE in µmol m^{-2} s^{-1}.

	MLR	**MDS**	**MLP**	**RBF**	**GRNN**
r	0.79	0.70	0.95	0.93	0.96
RMSE	1.23	1.24	0.59	0.75	0.59
AIC	1387.20	-	-2874.21	-119.67	62060.46
BE	0.00	0.02	-0.00	-0.00	-0.01
MAE	0.92	0.79	0.34	0.51	0.39
scaling exponent	-0.96	-0.80	-1.16	-1.11	-1.16

Table C.6: F_{CO_2} model statistics, Year 2 SC_{rew}. RMSE, BE and MAE in µmol m^{-2} s^{-1}.

	MLR	**MDS**	**MLP**	**RBF**	**GRNN**
r	0.83	0.83	0.93	0.88	0.94
RMSE	1.00	0.92	0.64	0.85	0.61
AIC	46.52	-	-1811.23	77.57	44621.70
BE	-0.00	0.03	-0.00	-0.00	0.02
MAE	0.70	0.61	0.34	0.58	0.41
scaling exponent	-1.22	-0.83	-1.27	-1.03	-1.07

Table C.7: Input selection result (**bold**: in final Matrix) for Year 2 F_{CO_2} from SC_{rew}

	Timelag	Score
Lw_{out}	2.0	5.0
R_g	0.5	5.0
P_{air}	12.0	0.0
$slope_{Pair}$	3.5	2.0
VPD	2.5	3.0
T_{air}	2.5	8.0
WT	6.5	5.0
T_{Soil40}	5.5	5.0
T_{Soil2}	4.0	7.0
T_{Soil5}	-5.0	6.0
T_{Soil10}	-2.0	6.0
T_{Soil20}	2.5	5.0
$Redox_2$	1.0	5.0
$Redox_5$	1.5	7.0
$Redox_{10}$	1.0	6.0
$Redox_{20}$	1.5	6.0
par	0.5	5.0
Lw_{out} #lag	-	3.0
R_g #lag	-	3.0
P_{air} #lag	-	0.0
$slope_{Pair}$ #lag	-	1.0
VPD #lag	-	2.0
T_{air} #lag	-	7.0
WT #lag	-	6.0
T_{Soil40} #lag	-	5.0
T_{Soil2} #lag	-	6.0
T_{Soil5} #lag	-	5.0
T_{Soil10} #lag	-	6.0
T_{Soil20} #lag	-	7.0
$Redox_2$ #lag	-	7.0
$Redox_5$ #lag	-	6.0
$Redox_{10}$ #lag	-	6.0
$Redox_{20}$ #lag	-	6.0
par #lag	-	8.0
$CC_{veg,E}$	-	12.0
CC_{dra}	-	3.0
$fuzzy_{mo}$	-	6.0
$fuzzy_{af}$	-	9.0
$fuzzy_{ev}$	-	9.0
$fuzzy_{ni}$	-	9.0
$fuzzy_{su}$	-	9.0
$fuzzy_{wi}$	-	12.0

Table C.8: Input selection result (**bold**: in final Matrix) for Year 2 F_{CO_2} from SC_{rew}

	Timelag	Score
Lw_{out}	2.0	5.0
R_g	0.0	5.0
P_{air}	8.5	2.0
$slope_{Pair}$	-2.5	0.0
VPD	2.5	3.0
T_{air}	2.0	8.0
WT	6.0	4.0
T_{Soil40}	-6.5	7.0
T_{Soil2}	3.5	8.0
T_{Soil5}	6.0	8.0
T_{Soil10}	-3.0	8.0
T_{Soil20}	2.0	6.0
$Redox_2$	-1.5	6.0
$Redox_5$	0.0	3.0
$Redox_{10}$	0.5	6.0
$Redox_{20}$	1.5	5.0
par	0.5	2.0
Lw_{out} #lag	-	4.0
P_{air} #lag	-	0.0
$slope_{Pair}$ #lag	-	1.0
VPD #lag	-	4.0
T_{air} #lag	-	6.0
WT #lag	-	5.0
T_{Soil40} #lag	-	7.0
T_{Soil2} #lag	-	7.0
T_{Soil5} #lag	-	7.0
T_{Soil10} #lag	-	7.0
T_{Soil20} #lag	-	7.0
$Redox_2$ #lag	-	5.0
$Redox_{10}$ #lag	-	5.0
$Redox_{20}$ #lag	-	6.0
par #lag	-	8.0
$CC_{veg,W}$	-	9.0
CC_{rew}	-	3.0
$fuzzy_{mo}$	-	8.0
$fuzzy_{af}$	-	9.0
$fuzzy_{ev}$	-	9.0
$fuzzy_{ni}$	-	9.0
$fuzzy_{su}$	-	11.0
$fuzzy_{wi}$	-	11.0